Experimental and theoretical developments for the acoustoelastic characterization and stress-monitoring of concrete materials and structures

Agustin Spalvier Blanco

Programa de Posgrado en Ingeniería Estructural

Facultad de Ingeniería

Universidad de la República

Montevideo – Uruguay

Diciembre de 2020

Experimental and theoretical developments for the acoustoelastic characterization and stress-monitoring of concrete materials and structures

Agustin Spalvier Blanco

Tesis de Doctorado presentada al Programa de Posgrado en Ingeniería Estructural, Facultad de Ingeniería de la Universidad de la República, como parte de los requisitos necesarios para la obtención del título de Doctor en Ingeniería Estructural.

Director:
  Dr. Prof. Ing. Gonzalo Cetrangolo

Codirector:
  Ph.D. Prof. John S. Popovics

Director académico:
  Dr. Prof. Alina Aulet

Montevideo – Uruguay
Diciembre de 2020
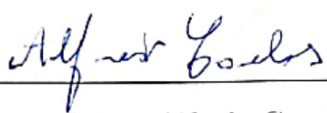
INTEGRANTES DEL TRIBUNAL DE DEFENSA DE TESIS

Dr. Prof. Nicolás Benech

Dr. Prof. Ing. Alfredo Canelas

Dr. Prof. Ing. Raul Bertero

Dr. Prof. Ing. Atilio Morquio

Dr. Prof. Ing. Nicolás Pérez

Montevideo – Uruguay

Diciembre de 2020

IV

Acknowledgments

First I would like to thank my family for their unconditional support. I would like to thank the committee members, for their time and comments that improved this thesis' qual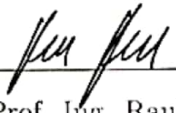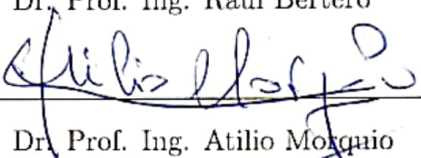ity; specially Atilio Morquio for the innumerable and fruitful discussions at the beginning of this doctoral research, Nicolás Pérez for his help with several experiments and Alfredo Canelas for his help with the theoretical developments. I would also like to acknowledge the help of my lab-mates and friends, Gonzalo Moltini, Alina Aulet, Vanesa Baño, Carlos Mazzey, Gonzalo Cabrera, and Santiago Laco, who helped me many times with the experiments, field tests and by giving interesting suggestions. I am particularly grateful to my lab-mate and friend Leandro Domenech, who helped me very much in several stages of this investigation, both during the experiments and analysis, which was clearly fruitful for this thesis. I would also like to thank several professors, researchers and staff who helped me carry out this investigation, in particular Luis Segura and Berardi Sensale, for their comments and advice, Marcelo Gancio, Alberto Gómez, Jimena Machado and Cinthia Planchón for helping me solve many practical experimental, computing and bibliographical situations, María Noel Pereyra and the other members of the Concrete Lab of the *Departamento de Construcción*, who allowed me building concrete samples and gave me advice on several occasions, and my friend Jesús Eiras, Cédric Payan and Vincent Garnier for giving me the chance of meeting, collaborating and working within their lab in Aix-Marseille. Finally, I am especially grateful to my adviser Gonzalo Cetrangolo, and co-adviser John S. Popovics, for their advice and guidance during these years, giving me the necessary support, with interesting suggestions and ideas, always with patience and creating an excellent working environment that I am glad to be part of.

To finish, I would like to mention and thank the *Comisión Académica de Posgrado* and the *Comisión Central de Dedicación Total* for supporting me as a teacher and researcher in the *Universidad de la República*, the *Centro de In-*

RESUMEN

Para evaluar el estado de las estructuras civiles es frecuentemente necesario conocer el nivel de tensión que soportan los distintos elementos estructurales. Sin embargo, el desarrollo de técnicas eficientes de ensayos no destructivos para la estimación de tensiones de estructuras de hormigón sigue siendo un tema abierto. Con este fin, investigaciones anteriores han estudiado la dependencia de la velocidad de propagación de ondas mecánicas con la tensión aplicada, esto es el "efecto acustoelástico". Estudios recientes en elementos de hormigón sometidos a compresión axial han mostrado que el efecto acustoelástico también puede ser detectado con técnicas basadas en fenómenos de vibración, lo que ofrece varias ventajas. Esta tesis se centra en el estudio, documentación y mejora del uso de técnicas de vibración (resonancia) para la caracterización acustoelástica y la determinación de tensiones en elementos estructurales alargados de hormigón, sometidos a compresión axial. Se incluye un desarrollo teórico exhaustivo con métodos analíticos y numéricos, donde el modo de vibración torsional se elige frente a los otros posibles modos de vibración. El parámetro nolineal material β_G se define en base a la vibración torsional, que corresponde a la tasa de cambio del módulo elástico de corte G respecto a la deformación axial. La expresión de β_G se calcula analíticamente respecto a las constantes elásticas de segundo y tercer orden (l, m, y n) y se verifica numéricamente usando modelos de elementos finitos. Los efectos de la torsión no uniforme (alabeo), la no-linealidad geométrica (efecto P-δ) y el del cambio de las condiciones de borde, son estudiados analítica, numérica y experimentalmente, para evaluar su efecto en β_G. Se realizan experimentos para tres mezlcas de hormigón usando tres especímenes prismáticos de dimensiones $15 \times 15 \times 60$ cm^3; los valores de β_G se calculan para estos tres especímenes sometiéndolos a varios ciclos de carga y descarga, lo que prueba la existencia, dominio y repetitividad del efecto acustoelástico: la frecuencia de vibración torsional aumenta al aumentar las deformaciones (y tensiones) de compresión en elementos alargados. Una segunda campaña experimental es realizada usando las técnicas de propagación de ondas ultrasónicas y vibración torsional simultáneamente en el mismo especimen de mortero. Contrariamente a las predicciones teóricas ba-

sadas en la acustoelasticidad, el ultrasonido arroja resultados de β_G un orden de magnitud menor que los resultados de β_G que arroja la vibración torsional. Para afrontar esta aparente contradicción, la teoría se completa heurísticamente teniendo en cuenta fenómenos menores de viscosidad. Finalmente, se presenta un caso de estudio de un estructura a escala real, un tanque de hormigón postensado para la contención de material nuclear, el cual se somete a incrementos graduales de presión interior. Se identifican las frecuencias de vibración usando un sistema de medición basado en técnicas de análisis modal operacional y se observa que las frecuencias de vibración se correlacionan con la presión interna. Tanto el experimento como el modelo de elementos finitos muestran que las frequencias de vibración aumentan al aumentar la presión interna, sugiriendo que, en este caso, la no-linealidad geométrica domina frente a los efectos acustoelásticos.

Palabras claves:
ensayos no destructivos, análisis de vibración, ultrasonido, no-linealidad material, torsión.

ABSTRACT

Condition assessment of civil infrastructure often requires knowing the current stress acting on a given structural member. However, the development of an efficient nondestructive testing (NDT) technique for estimating current stresses in structural concrete elements remains open. To this end, previous research have studied the dependence of mechanical wave speed with applied stress, "the acoustoelastic effect". Recent research on concrete elements under uniaxial compression has shown that the acoustoelastic effect can also be detected with techniques based on vibration phenomena, which offers several benefits. This thesis focuses on studying, documenting and improving the use of resonance vibration for acoustoelastic characterization and current stress determination of slender concrete structural elements under compression. An exhaustive theoretical development using analytical and numerical methods is provided, where the torsional vibration mode is selected over other vibration modes. The nonlinear material parameter β_G is defined based on torsional vibration, which corresponds to the rate of change of the elastic shear modulus G with respect to the uniaxial strain. The expression of β_G is analytically calculated with respect to the second and third-order elastic constants (l, m, and n) and numerically verified with finite element method (FEM) models. The effect of non-uniform torsion (warping), geometric nonlinearity (P-δ effect) and changing boundary conditions is studied analytically, numerically and experimentally, to assess their effect on β_G. Experiments are carried out for three concrete mixture designs using prismatic specimens of dimensions 15 $\times$ 15 $\times$ 60 cm^3; values of β_G are calculated for these specimens submitted to several loading and unloading cycles, which proves the existence, dominance and repeatability of the acoustoelastic effect: torsional frequency of vibration increases with increasing compressive strains (and stresses) in elongated elements. A second experimental campaign is conducted using ultrasonic wave propagation and torsional vibration techniques simultaneously on the same mortar specimen. Conversely to the theoretical predictions based on acoustoelasticity, ultrasonic results yield a β_G value an order of magnitude lower than the torsional vibration-based β_G. To address this apparent contradic-

tion the theory is completed heuristically by accounting for the slight material viscosity. Finally, a case of study of a real size post-tensioned-concrete nuclear-containment structure is presented, where the containment is submitted to gradual internal pressure. Frequencies of vibration are identified using an output-only sensing system and the tracked frequencies are correlated with internal pressure. Both the experiment and an FEM model show that frequencies of vibration increase with increasing internal pressure suggesting that geometric nonlinearity dominates over acoustoelastic effects in this case.

Keywords:
nondestructive testing, vibration analysis, ultrasound, material nonlinearity, torsion.

List of Figures

List of Tables

List of Symbols

List of the most relevant symbols in this Thesis.

$\mathbb{C}$ Right Cauchy-Green strain tensor used in the Theory of Finite Elasticity 42

$\mathbb{D}$ Strain tensor within the theory of infinitesimal linear-elasticity 10

E Young's modulus of a material 10

E_0 "Young's modulus" of a material where the subindex 0 emphasizes it corresponds to the undeformed state 33

E_ε "Young's modulus" of a material where the subindex ε denotes it corresponds to an elongated solid with a uniaxial strain of value ε 33

$\mathbb{E}$ Green-Lagrange strain tensor used in the Theory of Finite Elasticity 43

$\mathbb{F}$ Deformation gradient used in the Theory of Finite Elasticity 42

G Shear or transverse elastic modulus, equivalent to Lamé elastic constant μ 11

G_0 "Shear modulus" of a material where the subindex 0 emphasizes it corresponds to the undeformed state 35

G_ε "Shear modulus" of a material where the subindex ε denotes it corresponds to an elongated solid with a uniaxial strain of value ε 34

$G_{\varepsilon,T}$ Temperature and strain-dependent shear elastic modulus of an elongated solid, that controls torsional vibration, used in Chapter 5 88

$G_{0,T0}$ Temperature and strain-dependent shear elastic modulus of an elongated solid, that controls torsional vibration, at the undeformed state $\varepsilon = 0$ and constant temperature $T = T_0$, used in Chapter 5 88

$G_{\varepsilon,T0}$ Temperature and strain-dependent shear elastic modulus of an elongated solid that controls torsional vibration, at a deformed state given by ε and constant temperature $T = T_0$, used in Chapter 5 88

G' Storage modulus of a viscoelastic solid, defined as the real part of the complex modulus, used in Chapter 5 105

used when using Theory of Finite Elasticity 41

X_2 Lagrange material coordinate in direction 2 of a Cartesian axes system, used when using Theory of Finite Elasticity 41

X_3 Lagrange material coordinate in direction 3 of a Cartesian axes system, used when using Theory of Finite Elasticity 41

a Longitudinal stretch of an elongated solid used in the Theory of Finite Elasticity 41

b Transverse stretch of an elongated solid used in the Theory of Finite Elasticity 41

b_G Factor that establishes a linear relationship between temperature T and the temperature-dependent shear modulus $G_{\varepsilon,T}$, used in Chapter 5 88

β Generic material nonlinear parameter associated to the elastic constant that relates the applied stress σ to the squared strains ε^2 for a given constitutive relationship 26

β_{bulk} Material nonlinear parameter associated to the elastic constant that relates the applied stress σ to the squared strains ε^2 for a given constitutive relationship associated to a wave traveling in an infinite medium. 26

β_E Material nonlinear parameter associated to the elastic constant that relates the applied uniaxial stress σ to the squared uniaxial strains ε^2 for a given nonlinear constitutive relationship associated to an elongated solid axially loaded, which can be interpreted as the rate of variation of the Young's modulus E during a uniaxially loading test 33

β_G Material nonlinear parameter associated to the elastic constant that relates the applied shear stress τ to the squared shear strains γ_τ for a given nonlinear constitutive relationship associated to an elongated solid axially loaded, which can be interpreted as the rate of variation of the shear modulus γ during a uniaxially loading test 35

β'_G Frequency dependent nonlinear shear elastic modulus calculated from assuming a solid viscoleastic model with nonlinear (strain dependent) spring constants and linear viscosity, used in Chapter 5 108

c Viscous damping constant of a vibrating mass-spring-damper single degree of freedom system, associated to the Structural Dynamics topic 15

χ Deformation field of a solid used when using the Theory of Finite Elasticity 42

δ Generic material nonlinear parameter associated to the elastic constant that

relates the applied stress σ to the cubic strains ε^3 for a given constitutive relationship 26

ε Engineering strain normal to a given cross-section of an elongated solid (bar), defined as the bar's deformed length minus the original length, divided by the original length, parallel to the solid's longitudinal (axial) direction, mainly used associated to the Hooke's Law: $\sigma = E\varepsilon$ 10

ε_{11} Element 11 of the strain tensor $\mathbb{D}$, equivalent to the engineering strain ε for the case of an elongated solid axially loaded 46

ε_1 Axial principal strain of an elongated solid in a deformed state, state 1 58

η_G Viscosity constant of the damper in a viscoelastic model with nonlinear (strain-dependent) spring constants and linear viscosity, used in Chapter 5 103

f Frequency of vibration of a system in Hz, frequency variable in a frequency-domain description, or frequency of a solid's particle while a wave is traveling through 13

f_1 Frequency of vibration, in Hz, of the first mode (fundamental) of an elongated solid in torsional vibration 37

f_1 Fundamental torsional frequency of vibration of an elongated solid in a deformed state, state 1 58

f_0 Fundamental torsional frequency of vibration of an elongated solid in the undeformed state, state 0 58

f_c Concrete compressive strength 7

γ Wavenumber defined in a distributed-parameter vibrating element, which defines the modal shapes 21

γ_τ Shear strain or distortion, acting parallel to a specified section 11

$i_G(\Delta T)$ Factor that establishes a linear relationship between temperature the temperature-and-strain-dependent shear modulus $G_{\varepsilon,T}$ at temperature T and the strain-dependent shear modulus $G_{\varepsilon,T0}$ at constant temperature T_0, used in Chapter 5 88

$i_{G,(C)}(\Delta T)$ Factor that establishes a linear relationship between temperature the temperature-and-strain-dependent shear modulus $G_{\varepsilon,T}$ at temperature T and the strain-dependent shear modulus $G_{\varepsilon,T0}$ at constant temperature T_0, of the control specimen, used in Chapter 5 89

k Stiffness constant of a vibrating mass-spring-damper single degree of freedom system, associated to the Structural Dynamics topic 15

k Stiffness linear constant to represent the boundary conditions in the ends of an elongated solid in torsional vibration 38

l First Murnaghan third order elastic constant 25

λ First Lamé elastic constant of a material 10

λ_ω Wavelength of a propagating wave 13

m Mass of a vibrating mass-spring-damper single degree of freedom system, associated to the Structural Dynamics topic 15

m Second Murnaghan third order elastic constant 25

m_T Linear parameter, slope, that relates the specimen's $i_G(\Delta T)$ with the control specimen's $i_{G,(C)}(\Delta T)$, used in Chapter 5 89

μ Second Lamé elastic constant of a material 10

n Modal number of a system, where $n = 1$ represents the first (fundamental) mode and frequency of vibration 22

n Third Murnaghan third order elastic constant 25

n_T Linear parameter, y-intercept, that relates the specimen's $i_G(\Delta T)$ with the control specimen's $i_{G,(C)}(\Delta T)$, used in Chapter 5 89

ν Poisson's ratio elastic constant of a material 11

ν_0 "Poisson's ratio" of a material where the subindex 0 emphasizes it corresponds to the undeformed state 36

ω Angular frequency of vibration of a system or angular frequency variable in a frequency-domain description 16

$\overline{\omega}_1$ Angular frequency of vibration of an undamped single degree of freedom system freely vibrating, associated to the Structural Dynamics topic 16

ω_1' Natural frequency of vibration of a damped single degree of freedom system vibrating freely, associated to the Structural Dynamics topic 17

ω_1 Angular frequency of vibration of the first mode (fundamental) of an elongated solid in torsional vibration 36

$\hat{\omega}_0$ Angular frequency of vibration of the "nearly rigid" mode (mode 0), present due to the elastic boundary conditions at the ends of an elongated solid in torsional vibration 39

$\hat{\omega}_1$ Angular frequency of vibration of the first (fundamental) mode, which has been affected by the presence of the elastic boundary conditions at the ends of an elongated solid in torsional vibration 39

ω_n Angular frequency of vibration of the nth mode of a system 22

$p(t)$ Time-dependent forcing function applied to a mass-spring-damper single

Contents

Chapter 1

Introduction

Civil infrastructure is one of the key components for countries to develop socially and economically. There are a number of examples that depict the importance of civil infrastructure in our lives; they affect society much more than we realize. Massive concrete dams are needed to generate electricity, large bridges and deep tunnels connect otherwise isolated towns and cities, highways enable fast and safe traffic, thick concrete tanks safely contain nuclear material, and fantastic stadiums are built to house enjoyable shows.

We tend to note the importance of these structures only when they are lacking or during their construction. But once they are standing and successfully operating, they fulfill their function and our attention diverts. We see them as everlasting immutable pieces of steel and concrete. Despite their appearance, structures are not immutable, they change, for a variety of reasons, and as time goes on, they tend to deteriorate. This brings up one very important task for governments to manage, which is, the maintenance of civil infrastructure.

We do not only want to build new infrastructure, but also to keep what we already have safe and functional. This latter task is naturally not as rewarding as the former: a new bridge is built in one or two years, which solves a specific problem in a short period of time and calls our attention very much, but we are already used to the benefits of the existing infrastructure, and thus, we cannot see the maintenance work gradually done over the decades which keeps it functional. Therefore civil infrastructure maintenance tends to be politically unattractive, so funding is usually scarce, increasing the problem even more.

Maintenance of civil infrastructure is therefore an enormous responsibility for all society, not only for our government leaders, but also for private

companies, professionals, architects and engineers, the academia and the users too. The application of early and responsible maintenance actions saves public funds in comparison to lately applied maintenance; and this is the least important benefit. Early maintenance prevents catastrophes, which often involve irrecoverable social, environmental and economic losses [1–4].

Once aware of these drastic consequences, it is not difficult to acknowledge the benefits of early maintenance actions, but it is much more difficult to decide when and how to make these actions, and of course, how much to invest. To this end, good quality information is highly appreciated to feed an efficient infrastructure management plan and produce well-founded decisions for conservation actions. And there is no other way to gather good quality information than from accurate structural inspections. The field of civil infrastructure maintenance is therefore composed by a mixture of these three interdisciplinary areas: management, inspection and conservation.

This Thesis focuses on the inspection area for civil infrastructure assessment. There are many criteria to classify inspection techniques. One of these corresponds to the effect that techniques have on the structure under study: if they involve extracting considerable physical samples or otherwise imposing some sort of impairment they are called "destructive testing". Those who do not affect the structure significantly are called "nondestructive testing" (NDT) or "nondestructive evaluation" (NDE) techniques. Destructive techniques are necessary to produce direct and unquestionable results, for example, to measure material properties, but they are expensive and cannot be extensively applied along the structure nor periodically applied in time. On the other hand, NDT techniques tend to be less expensive, and can be extensively and periodically applied.

The most basic—and extensively used—NDT technique for civil infrastructure condition assessment is visual inspection [5, 6]. This is a very powerful NDT technique which allows detecting deterioration mechanisms and causes of distress without the need of special equipment. On the other hand, it requires an experienced inspector, and only accessible parts of the structure can be inspected successfully. Furthermore, visual inspection is obviously very limited as only superficial macroscopic distresses can be identified. There are a number of more sophisticated NDT techniques capable of providing useful information about the structure, each specialized to satisfy a specific goal [5, 7]. To mention some of them, ultrasonic wave propagation allows detecting internal flaws

hidden within the material [5, 8], resonance vibration allows estimating the material's elastic properties [5, 9], ground penetrating radar allows identifying internal steel reinforcement [5], etc.

As science and technology evolves, researchers continue developing new techniques with higher capabilities, and finding new applications for existing NDT techniques; and that is the general goal of this Thesis, to review, develop and assess the use of a specific NDT technique for condition assessment of concrete civil structures. The goal is to shed light upon an open topic in the field of NDT techniques for concrete structures.

Civil structures are built to support loads and transfer them to the ground safely and efficiently. These loads stress the materials composing the structure. But materials cannot withstand any level of stress; at a certain maximum stress level, materials fail. This maximum stress level is called, in general terms, strength. To be sufficiently safe, concrete structures are designed to work at stress levels far away from their strengths, but there is no accurate way to know the exact stress that these structures actually support. This fact would not sound strange for a structural engineer but it will definitely call the attention of other professionals and scientists of other fields. How is it possible that we design an engineering product (a structure) to have a certain function (to support stresses) and we do not measure the outcome of the product (the actual stresses occurring in the structure)? The problem resides in the experimental difficulty for measuring current stresses in real structures. There has been efforts to develop testing techniques to solve this problem mainly on steel structures [10, 11] and also in concrete structures [12, 13]. As explained in Chapter 2, many of these are destructive testing techniques, which might not be applied in many cases. The topic of having an accurate NDT technique for current stress determination in concrete structures remains open. This is the principal motivation of this Thesis' work.

Within the field of NDT for concrete structures, there are those which rely on the physical phenomenon of mechanical wave propagation. Waves propagating through a solid medium can be measured and provide information about the solid, for example, its elastic modulus, or some geometric feature. In particular, there is an effect called "acoustoelastic" effect, which explains the experimentally observed stress dependence of mechanical wave speed [14]. Thus, this effect provides a pathway for measuring current stresses in solids. This topic has been deeply studied in metals [11, 15], and it has been gaining

importance in concrete during the past decade [16–18]. However, these efforts have not been sufficient to provide a successful tool for stress determination in concrete structural elements yet. The acoustoelastic effect (the change of wave speed due to stress changes) in concrete is so small that the effect is frequently coupled with other material phenomena, so its characterization has been difficult and highly variable.

Another set of NDT for concrete structures are those that rely on vibration or structural dynamics. These tests inspect the whole piece of structure and not some local portion as wave propagation does; so from that view point they are more robust. On the other hand, vibration phenomena are affected by the structure's boundary conditions, involving another influencing factor which introduces more experimental difficulties. Traditionally, the frequency of vibration of elongated elements axially compressed (like piles, columns, or post-tensioned beams) have been studied using the theory of linear-elasticity, which predicts a slight decrement of the frequency of vibration with axial compression increments [19]. However, recent research has shown the opposite behavior: frequency of vibration increases with increasing axial compressions [20, 21]. This behavior is actually in agreement with the acoustoelastic effect previously posed, which in turn, is directly connected to material nonlinearity. However, efforts to use resonance vibration for acoustoelastic characterization, and ultimately for stress determination, did not continue prospering, leaving a knowledge gap which this Thesis aims to fulfill.

The objectives of this Thesis are:

- To increase the knowledge regarding NDT techniques applied for condition assessment of concrete structures.
- To study, both theoretically and experimentally, the phenomenon of acoustoelasticity and material nonlinearity in concrete and its potential for current stress determination.
- To develop an experimental technique for acoustoelastic characterization of concrete elongated elements based on resonance vibration.
- To propose and assess, theoretically and experimentally, a fully NDT technique capable of determining current stresses in concrete elongated elements under compression (columns).

This Thesis contains several contributions to the field of Materials, Structural and Civil Engineering from an applied academic point of view, with

4

potential for field applications. Specific material parameters are analytically posed using the Theory of Finite Elasticity applied to nonlinear materials, in order to unify acoustoelastic observations of resonance tests to the existing acoustoelastic observations of wave propagation tests. Numerical analyses substantiate the analytical developments. These nonlinear parameters are experimentally calculated, to characterize material nonlinearity (acoustoelasticity) of concrete and mortar[1] elements. Thorough experimental details are provided to enable external reproduction and verification of the results. A virtual experiment is presented to study the capability of using acoustoelasticity for stress determination in elongated concrete structural members under compression.

This Thesis is organized in seven chapters and additional appendices. Chapter 1 introduces the topic and objectives. Chapter 2 summarizes the existing theory and background. Chapter 3 contains analytical and numerical developments; it includes the proposition and theoretical development of two material nonlinear parameters, β_E and β_G, their connection with the existing theory of nonlinear elasticity and wave propagation theory, and the analysis of the virtual experiment for stress determination. Chapter 4 presents the experimental procedures, results and discussion that substantiates the development of a resonant-vibration-based-NDT technique for the acoustoelastic characterization of concrete. Chapter 5 contains the experimental procedures, results and discussion carried out to verify the theory of acoustoelasticity using both sets of techniques: wave propagation vs. torsional vibration; it is shown that these do not agree so the chapter includes a final section that discusses these findings. Chapter 6 is a case-study where frequency of vibration is used to monitor internal pressure in a real size concrete structure. Finally, chapter 7 contains the overall conclusions.

---

[1]Mortar materials are concrete-like materials composed of cement, water and fine aggregate (sand) but without coarse aggregate.

Chapter 2

Theory and Background

2.1. Concrete Materials and Structures

Concrete is a mixture of cement, usually Portland cement, water, coarse aggregate (like gravel, granite or limestone chip), fine aggregate (sand) and air. It can also contain mineral or chemical admixtures, added to improve a specific property. Its constituents are put together during mixing, period in which it behaves as a fluid-like material, and then it is poured into a previously constructed formwork. The fresh concrete will then take the shape of the formwork, and after a dormant period, it will harden to become what can be conceived as a manufactured rock. This procedure is far from being as simple as it sounds; it involves many specialized steps, for example, the use of good vibration and compacting techniques depending on the type of structure, the use of a proper curing technique to avoid water evaporation, the use of compatible cement and aggregate to avoid unwanted chemical reactions during its harden state, the amount (and also time of introduction into the mixture) of the admixture material, and many more [22, 23].

The end product, the harden concrete becomes a complex material too. In its harden state, concrete is naturally heterogeneous composed of three phases, solid, liquid and gas. Moreover, its constituents form an "interfacial transition zone", a thin layer at the interface between the aggregate and the cementitious hydration products, which accounts for many of the macroscopic solid properties that we measure. These are characteristics comparable to natural rocks. Like natural rocks, concrete has a high strength when put under compression forces, this is, it has a high compressive strength, but it has a lower tensile

strength. For this reason, steel bars, with higher tensile strength than concrete are embedded into the concrete mass to produce reinforced concrete, an even more complex material, but capable of resisting both compressions and tensions [22, 23]. The use of steel reinforcement gives concrete the capability of resisting bending, which has been key to enable slender and efficient constructions, leaving behind the massive arcs and thick columns, and giving way to thinner slabs, walls, beams and columns.

2.2.   The Behavior of Concrete Under Stress

Structures are built to support loads (dead loads, wind, live loads, earthquakes, etc.) and to transfer them to the ground safely. These loads stress the materials that form the structures. Thus, understanding the behavior of materials under stress is key to allow safe and efficient construction. With this motivation, the behavior of concrete under stress has been a long investigated and well documented field of study [22, 23].

Concrete microscopic complexity is responsible for its mesoscopic and macroscopic-scale behavior. Even in these latter scales, concrete is heterogeneous and not fully isotropic, it is nonlinear, viscoelastic, and time-variant (due to the ongoing hydration reactions that make concrete stiffer and stronger)[22]. Furthermore, the use of steel reinforcements introduces even more complexity. Perhaps the most important effect is the fact that steel bars allow concrete structural members to work partially cracked. Thus, the geometrical properties of the members' cross-sections become stress-dependent, which affects structural behavior in many ways. Such complexities have made scientists and engineers undertake drastic hypotheses in order to ease reinforced concrete design methods and guarantee safety at the same time [22, 23].

This Thesis focuses on the study of concrete members under compression, as it could be the case of columns, arcs or even some loading situations of prestressed and post-tensioned beams. So let us focus the analysis on concrete under simple compression; i.e. an elongated solid whose sections are compressed uniformly. There are standardized procedures that prescribe how to characterize concrete under compression, i.e. how to measure the material's strain-stress relationship, particularly to determine concrete compressive strength and "elastic moduli" [24, 25].

Concrete compressive strength f_c is the most important material property

of structural concrete design. It is the ultimate stress that supports a cylindrical concrete specimen when submitted to simple compression. Figure 2.1 shows the stress-strain relationship of a typical compressive strength test and indicates the compressive strength. Due to concrete complexity, standards specify a number of experimental features, like the specimen's shape, the age of concrete when tested, the loading rate, the curing conditions (temperature and humidity), and others, which need to be respected in order to obtain valid (inter-laboratory-comparable) results [22]. Compressive strength is key to design concrete and specifically to determine the ultimate load that a given structural member supports. However, it does not describe the element's behavior in service[1], where load levels are low. For that we use the elastic moduli.

The elastic modulus of a material is a constant that relates linearly stresses and strains. Because concrete has a clear nonlinear stress-strain relationship, the use of a single elastic modulus to model its full stress-strain range (from 0 to its strength) is theoretically invalid. However, concrete in service is submitted to only ∼20 % of its strength [23], and for low-level compressions, lower than ∼ 30-40 % of concrete compressive strength, its behavior can be approximated to a linear-elastic model [22, 23]; thus, using an elastic modulus within that range of loads has provided practical and useful results for purposes of structural engineering design. Nevertheless, concrete technology specialized literature and structural standards define several "types" of elastic moduli for concrete [22, 24, 26, 27]. Figure 2.1 [22] presents concrete compressive stress-strain relationship, where the various "types" of elastic moduli for concrete under compression are depicted, but there are other definitions for tension and bending. These elastic moduli of concrete take special importance to determine structural deformations in service for design purposes.

The stress-strain relationship presented in Figure 2.1 follows a fairly linear behavior up to ∼40 % compressive strength and then there is a clear nonlinear behavior, where stresses increase at a lower rate than the increments of strain. This type of stress-strain nonlinearity is called softening, and it occurs due to the initiation and coalescence of microcracks [22].

Recent research has shown that during the quasi linear-elastic period of concrete under compression, i.e. when concrete is compressed below 40 % of

---

[1] "Service" makes reference to the state of the concrete being part of a standing structure. Service loads are those that regularly act on a structure. These are much lower than the ultimate or design loads, which are the maximum loads that the structural member supports.
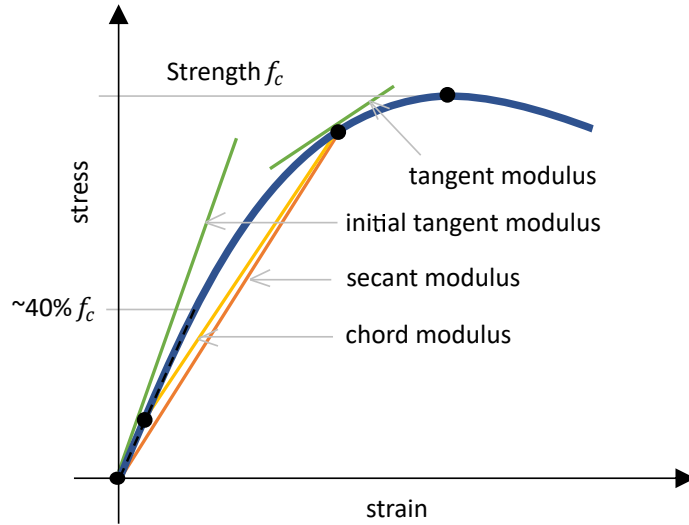
Figure 2.1: Compressive stress-strain relationship, and elastic moduli definitions, proposed by the literature, structural standards and building codes specialized in structural design of concrete.

its strength, it actually follows a minor stiffening behavior [16, 17, 28], meaning that as compressive strains increase, compressive stresses increase at a higher rate. This effect is not only seen in concrete but in other materials, like steel, aluminum, rock, and plastic too [29–33]. Again, this behavior can be conceived as a stress (or strain) dependent modulus of elasticity, where, in this case, the elastic modulus increases with increasing compressions. Thus, any technique capable of characterizing the elastic modulus, should in theory, be capable of characterizing this stiffening effect, like for example mechanical (acoustic) wave propagation techniques. Therefore, the field of science that studies this effect has been known as acoustoelasticity; acoustoelastic effects are those in which mechanical stresses of a solid material affect wave speed. It should be noted though, that this effect is actually a corollary of material nonlinearity [34].

2.3.   Linear Elastic Solid

In order to gain insight about material nonlinearity, acoustoelasticity and other nonlinear effects in concrete, let us first pose the traditional linear theory of elasticity. Let us consider an elongated solid (prismatic bar) with axial

dimension L_1 and base dimensions L_2 and $L_3 = L_2$. This hypothesis focuses the analysis on typical structural elements of the civil engineering field, such as columns and beams. Also, consider the solid to be homogeneous and isotropic. Whenever these hypotheses are in doubt, the necessary clarifications will be done. Figure 2.2 shows a diagram with the bar's dimensions and Cartesian axes 1, 2 and 3.
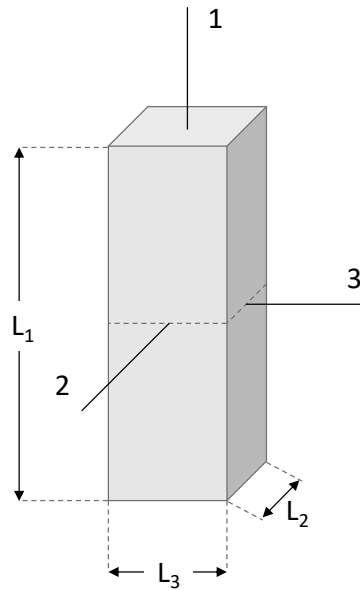
Figure 2.2: Prismatic bar of dimensions L_1, L_2 and L_3 and Cartesian axes.

When this elongated bar is subjected to uniaxial stress, i.e. by applying uniform stresses at their end faces, the expression that relates the normal (longitudinal) stresses σ (in the direction 1) and the strain ε developed in that same direction is the renowned Hooke's Law

$$\sigma = E\varepsilon, \tag{2.1}$$

where the elastic constant is the Young's modulus E. The Hooke's Law established by equation (2.1) is a uniaxial version of a tridimensional law. To describe the tridimensional elastic behavior it is necessary to consider the Generalized Hooke's Law

$$\mathbb{T} = \lambda \mathrm{tr}(\mathbb{D})\mathbb{I} + 2\mu\mathbb{D}, \tag{2.2}$$

where $\mathbb{T}$ is the stress tensor, $\mathbb{D}$ is the strain tensor, $\mathbb{I}$ is the identity matrix, λ and μ are the Lamé second order elastic constants which are related to the

Young's modulus E and the Poisson's ratio ν by

$$\lambda = \frac{E\nu}{(1+\nu)(1-2\nu)}, \qquad (2.3)$$

$$\mu = \frac{E}{2(1+\nu)}. \qquad (2.4)$$

Note that one can go from equation (2.2) to equation (2.1) by identifying that $\sigma = \mathbb{T}_{11}$. Equation (2.2) poses a linear and elastic behavior between stresses and strains, and it is usually applied under the condition of small strains and small displacements, i.e. using the infinitesimal theory of elasticity, which constitutes the approach to describe the majority of civil engineering problems [35].

Another typical stress state is pure shear, which is particularly developed in bars of circular cross-section under pure torsion. This stress state can be studied using the Generalized Hooke's Law described by equation (2.2), which reduces to a scalar equation where the shear stresses τ $(= \mathbb{T}_{12})$ are related to the shear strains γ_τ $(= 2\mathbb{D}_{12})$ by

$$\tau = G\gamma_\tau, \qquad (2.5)$$

where $G(=\mu)$ is the elastic shear modulus.

2.4. Traditional Stress Determination Techniques

In-situ stress determination has been a long studied topic, initially focused on residual stress determination in rock and steel [36]. These topics have been usually studied from a geotechnical or mechanical engineering stand point, respectively. The latter field has developed significantly over the years, ultimately converging into a number of handbooks and standards which detail the proposed techniques [10, 11, 15]. The civil engineering and concrete materials fields of study have adopted some of these techniques and tested them onto concrete material structures.

The most basic techniques for stress determination in concrete are those based on strain relief. They consist in gradually relieving the existing strain (and stress) of a portion of the examined concrete structure by hole drilling,

core drilling, or notch cutting. The strain relief is measured using strain gauges during the intervention. If the type of the existing stress state is known (e.g. uniaxial or biaxial stress field) and the elastic constants of concrete are known, one can back-calculate the existing stress from the measured strain relief by fitting the result into the assumed theoretical behavior.

A number of studies have expanded the theory and practice of these techniques into concrete structures [12, 13, 37, 38]. For instance, Parivallal et al. [39] provide a clear method for implementing the core drilling technique in field. More recent research has continued this line, introducing finite element method [36, 38, 40], and digital image correlation techniques [41], which have improved the methods' accuracy.

The main advantage of these techniques is that they directly measure the strain relief and not some other magnitude that is later processed and converted into strain. On the other hand, the experiments involve a destructive intervention (drilling, coring or notching). Therefore, these techniques present the usual drawbacks of any destructive test, as they cannot be applied extensively, they tend to be expensive and they are not to be applied in delicate structures, such as some post-tensioned beams, liquid containers, nuclear containers, etc. In addition, the intervention creates heat which affect strains development, so specific experimental actions need to be considered to mitigate this problem, like using cooling water, which, in turn, can originate hygrothermal strains and can also affect the electric sensors. Finally, these destructive testing methods cannot be applied for continuous monitoring for obvious reasons, either for overall health condition assessment or for other specific goals, for example, tendon gradual stress losses in post-tensioned and prestressed beams. The use of nondestructive testing techniques could complement or even replace the use of destructive techniques for stress determination of concrete structures. The following two sections describe the fundamental theory of two types of non-destructive testing techniques: mechanical wave propagation-based techniques and resonance (vibration)-based techniques.

2.5. Mechanical Wave Propagation

Propagating mechanical waves are pulses of stress-strain traveling within a medium where energy travels but mass does not. As the pulse goes by, particles vibrate around a fixed point, enabling the pulse to propagate within

the medium, even though each particle stays close to their initial position.

To start the analysis, let us consider a harmonic plane wave traveling within a solid, homogeneous, isotropic, infinite medium. Let us also consider the medium to be linear-elastic, or otherwise consider that the stresses, strains and displacements originated by the wave are so small that the linear-elastic hypothesis holds. Under these hypotheses, it is possible to conclude that there are two possible wave modes capable of propagating [35]. The first mode corresponds to the primary waves or P-waves (also called pressure waves), where the particle motion is parallel to the direction of wave propagation, and the second mode to the secondary waves or S-waves (also called shear waves), where the particle motion is perpendicular to the direction of wave propagation. P-waves travel at a speed V_P given by equation

$$V_P^2 = \frac{\lambda + 2\mu}{\rho} = \frac{E(1 - \nu)}{\rho(1 + \nu)(1 - 2\nu)}, \tag{2.6}$$

where ρ is the medium's density. S-waves propagate at a speed V_S given by

$$V_S^2 = \frac{\mu}{\rho} = \frac{G}{\rho}. \tag{2.7}$$

P and S-waves are called "bulk waves" because they exist in infinite media (in reality, sufficiently far from boundaries). Note that the P and S-wave speeds depend only on the medium's density and two independent elastic constants. Thus, for a given solid with known (or measurable) density, it is sufficient to measure P-wave speed V_P and S-wave speed V_S to find both solid second order elastic constants, using equations (2.6) and (2.7). This procedure (inversion problem) will hold as long as the considered hypotheses are sufficiently valid. To assess the hypotheses validity, two other important features of wave propagation are needed to be presented: frequency and wavelength.

The wave speed V (of both P and S-waves) is related with the particles' frequency of vibration f and with the wave's wavelength λ_ω by [35]

$$V = \lambda_\omega f. \tag{2.8}$$

In many experiments, the frequency f is fixed as it is provided by the transducer that generates the wave. The type and experimental configuration of the transducer determines if only P-waves are generated, only S-waves, or both (or other wave modes not analyzed here). Then, the wave speeds V_P and

V_S are given by equations (2.6) and (2.7); and thus, the wavelength λ_ω is given by equation (2.8).

This technique in which wave propagation is used to characterize the materials elastic properties is widely used and has been vastly documented and standardized [7, 8, 42]. However, as said before, the accuracy of the results are directly dependent on the validity of the hypotheses. For concrete materials, none of the hypotheses are truly valid. Thus, a number of features need to be prescribed in order to allow these to hold. These are:

- The medium can be considered infinite if the wave's wavelength λ_ω is considerably smaller than the medium's dimensions. Thus, frequency f needs to be sufficiently high.
- The medium can be considered homogeneous and isotropic if the wave's wavelength is sufficiently larger than the aggregates that constitute the concrete mass. Thus, frequency f needs to be sufficiently low.
- Stresses and strains created by the propagating wave are small enough (and oscillate so fast) so that nonlinearity and viscosity are usually neglected from the analysis. However, the elastic moduli determined by this technique correspond to the "wave-propagation-dynamic-moduli", and are not equal to the "quasistatic moduli" that concrete has when submitted to service loads [7, 8]. Traditionally, the dynamic modulus of elasticity has been associated to the initial tangent modulus shown in Figure 2.1 [22].

To meet these requirements, standards recommend using ultrasonic wave propagation with frequencies between 20 to 200 kHz. These frequencies create ultrasonic waves with sufficiently large wavelengths to "see" concrete as homogeneous, and sufficiently small to avoid boundary interaction and to enable considering the medium as infinite [7, 8].

The reader should note that this section exposed the very basics of wave propagation. For instance, the very important effect of attenuation has not been introduced, which also prevents using higher frequencies. This and many other important features of wave propagation for concrete inspection are detailed elsewhere [7, 8, 42].

Finally, note that the wave speeds given in (2.6) y (2.7) are not dependent on the stress state of the solid's medium through which they travel. In other words, the wave speed and the medium's stress state are independent. This

characteristic is no longer valid when the medium material is considered non-linear, and a broader theory is needed: the Theory of Acoustoelasticity. Before introducing this theory, let us pose the basics of the second set of nondestructive testing techniques, those based on resonating (vibrating) solids.

2.6. Structural Dynamics: Vibration of Solids and Structures

Structural dynamics is a very broad field of study which touches transversely many other scientific and engineering fields. In civil engineering, structural dynamics is mainly used for structural design, to allow buildings to support wind loads and earthquakes, or as a method for nondestructive structural characterization (nondestructive testing or structural health monitoring). This Thesis focuses on the latter application.

There are many sources that develop the broad topic of structural dynamics [43, 44]. This section contains the very basics of this topic, in order to provide the fundamental theory used in the following chapters. As it is conventional in these textbooks, first, the single degree of freedom systems theory is presented, in order to gain insight about the specific concepts and magnitudes, and then the analysis is extended to multiple degrees of freedom systems, and to distributed-mass solids.

2.6.1. Single Degree of Freedom Systems

The most basic vibrating system, a single degree of freedom system, is represented by a mass m, a spring and a viscous damper connected as depicted in Figure 2.3, and subjected to a time-dependent force $p(t)$. The spring represents the system's stiffness, where the spring's force is opposite and proportional to the spring's elongation; its constant of proportionality is named k. Likewise, the viscous damper provides a force opposite and proportional to its rate of displacement, where its constant of proportionality is c.

The governing equation of motion of the system is

$$m\ddot{x} + c\dot{x} + kx = p(t), \tag{2.9}$$

where x is the mass's displacement (time-depending position with respect to
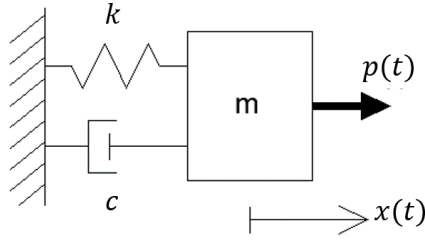
Figure 2.3: Single degree of freedom vibrating system.

rest position) and the dot implies derivation over time t.

When $p(t) = 0$, the system is free, so it is call "free vibration", in contrast to the opposite situation where the vibration is "forced" by $p(t)$. Also, if $c = 0$, the system is undamped, so equation (2.9) reduces to

$$m\ddot{x} + kx = 0. \tag{2.10}$$

Periodic solutions of equation (2.10) are of the form

$$x(t) = x_0 e^{i\omega t}, \tag{2.11}$$

where x_0 is a complex constant that depends on the initial conditions, and ω is the system's angular frequency of vibration, which, in this case, is given by

$$\omega^2 = \frac{k}{m} = \overline{\omega}_1^2. \tag{2.12}$$

The value $\overline{\omega}_1 = \sqrt{k/m}$ is the system's natural angular frequency of vibration. Note that "angular frequency" ω and "frequency" f are related by

$$\omega = 2\pi f. \tag{2.13}$$

For the case of an undamped vibration forced by

$$p(t) = p_0 e^{i\Omega t}, \tag{2.14}$$

where Ω is the forcing force's frequency, we can assume a solution of the form

$$x(t) = x_0 e^{i\Omega t}, \tag{2.15}$$

where both x_0 and p_0 are complex constants, so that by substituting these

16

equations into the equation of motion yields

$$(k - \Omega^2 m)x_0 e^{i\Omega t} = p_0 e^{i\Omega t}. \tag{2.16}$$

When the system is forced, it is common to characterize it using frequency response function (FRF), defined as the "receptance" $R = x_0/p_0$. In this case, the FRF becomes

$$R(\Omega) = \frac{x_0}{p_0} = \frac{1}{k - \Omega^2 m}. \tag{2.17}$$

Note that when the forcing frequency Ω equals the system's natural frequency $\overline{\omega}_1$, the receptance and the response x tend to infinity, i.e. the system resonates. Of course, in reality this does not occur because systems always have some sort of damping, which, even though amplitudes increase considerably around the natural frequency, they do not become infinite, as it is explained below.

When $c \neq 0$, the system is damped. Thus, the free vibration analysis yields a periodic solution

$$x(t) = x_0 e^{-\alpha t} e^{i\omega_1' t}, \tag{2.18}$$

where α is the damping rate, equal to $\xi\overline{\omega}_1$, where $\xi = c/(2\sqrt{km})$, and the system's natural frequency is

$$\omega_1' = \overline{\omega}_1 \sqrt{1 - \xi^2}. \tag{2.19}$$

Note at equation (2.18) that the free vibration $x(t)$ of the viscous damped system oscillates but decreases in amplitude following an exponential decrement given by α, which is real and positive. Also, because the damping ratio ξ tends to be much lower than 1 in concrete structures (in the order to 0.02 [45]), the system's natural frequency of vibration, ω_1', is slightly lower than the free undamped natural frequency $\overline{\omega}_1$.

When the single degree of freedom damped system is forced by $p = p_0 e^{i\Omega t}$, the receptance FRF is

$$R(\Omega) = \frac{1}{(k - \Omega^2 m) + i\Omega c}, \tag{2.20}$$

which is complex. Thus,

17

$$|R(\Omega)| = \frac{|x_0|}{|p_0|} = \frac{1}{\sqrt{(k - \Omega^2 m)^2 + (\Omega c)^2}}, \qquad (2.21)$$

so the receptance and the response peak when $\Omega = \omega_1'$, but do not tend to infinity as it occurs in the undamped case.

2.6.2.   Multiple Degrees of Freedom Systems

Multiple degrees of freedom systems (MDOF) are, of course, capable of representing a broader set of real situations than the single degree of freedom systems. These systems are treated in a similar manner as the single degree of freedom systems, but instead of having scalar magnitudes we now arrange them into matrices to obtain analogous equations. For instance, the equation of motion of an undamped MDOF system with N degrees of freedom is

$$[M]\{\ddot{x}(t)\} + [K]\{x(t)\} = \{p(t)\}, \qquad (2.22)$$

where $[M]$ is the $N \times N$ mass matrix, $[K]$ is the $N \times N$ stiffness matrix, and $\{x(t)\}$ and $\{p(t)\}$ are the $N \times 1$ time-dependent displacement and force vectors, respectively.

To exemplify the analysis, consider a two-floor building submitted to horizontal forces, which can be modeled as a 2DOF system, where the floors (slabs) are the masses, and the columns that connect the floors provide the lateral (bending) stiffness. Figure 2.4 depicts the structural and the MDOF mass/spring models.
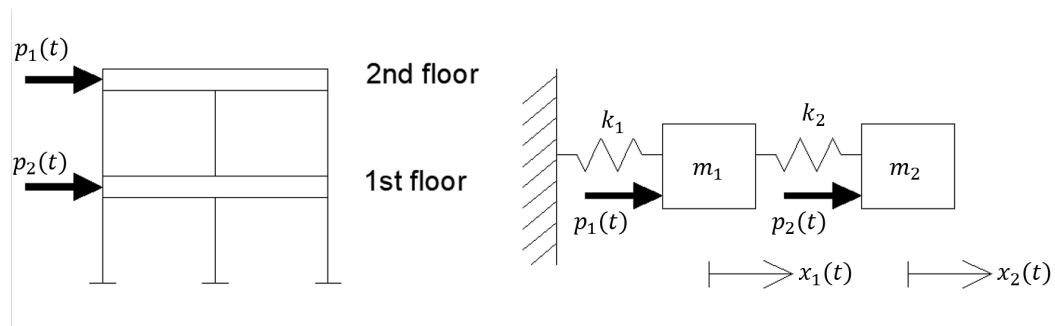
Figure 2.4: Left: Structural model of a two-floor building with floors and columns submitted to horizontal forces. Right: MDOF mass/spring model.

The two governing equations are

$$m_1\ddot{x}_1 + (k_1 + k_2)x_1 - (k_2)x_2 = p_1(t)$$

$$m_2\ddot{x}_2 + (k_2)x_2 - (k_2)x_1 = p_2(t),$$

which can be arranged in matrix form as

$$\begin{bmatrix} m_1 & 0 \\ 0 & m_2 \end{bmatrix} \begin{Bmatrix} \ddot{x}_1 \\ \ddot{x}_2 \end{Bmatrix} + \begin{bmatrix} k_1 + k_2 & -k_2 \\ -k_2 & k_2 \end{bmatrix} \begin{Bmatrix} x_1 \\ x_2 \end{Bmatrix} = \begin{Bmatrix} p_1 \\ p_2 \end{Bmatrix}. \qquad (2.23)$$

The free vibration solution of equation (2.22) is obtained by taking

$$\{p(t)\} = \{0\}.$$

By assuming a solution

$$\{x(t)\} = \{x_0\}e^{i\omega t},$$

we obtain

$$([K] - \omega^2[M])\{x_0\}e^{i\omega t} = 0, \qquad (2.24)$$

so that the only non-trivial solutions for ω are given by

$$\det([K] - \omega^2[M]) = 0. \qquad (2.25)$$

Equation (2.25) yields a set of values $\overline{\omega}_1, \overline{\omega}_2, ..., \overline{\omega}_N$ which are the N undamped system's natural frequencies. By substituting each of these back into equation (2.24), the modal shapes, associated to each frequency, are obtained.

If we consider again the two-floor building example, since it is a 2DOF system, it will have two undamped natural frequencies, $\overline{\omega}_1$ and $\overline{\omega}_2$. The lower frequency, $\overline{\omega}_1$, is associated to the first modal shape $\{\Psi\}_1$, and $\overline{\omega}_2$ to modal shape 2, $\{\Psi\}_2$. These are depicted in figure 2.5.

The analysis of MDOF can be expanded to incorporate viscous damping (or other types of damping), and to forced situations. In the latter case, the FRF functions can be deduced. Due to the multiple degrees of freedom, FRF originate by computing the N^2 terms $x_{0,i}/p_{0,j}$, for $i, j = 1, 2, ..., N$. The analysis becomes considerably more complex than the SDOF analysis, and it falls out of the scope of this thesis. The interested reader can consider the
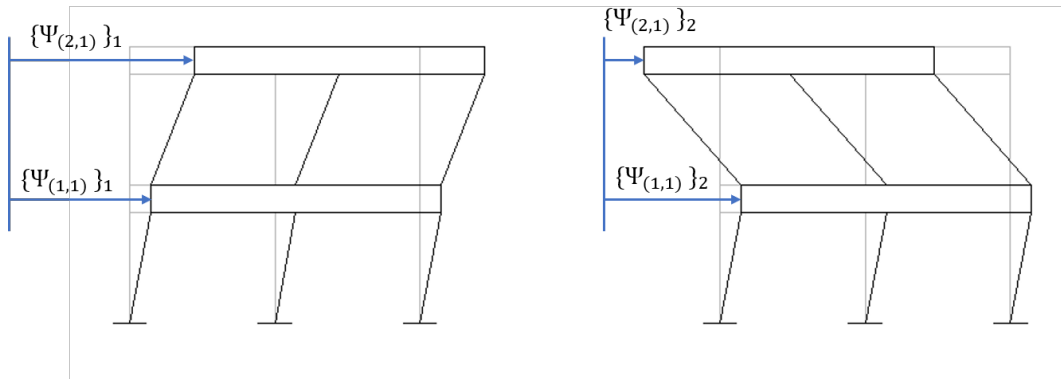
Figure 2.5: Modal shapes of an undamped 2DOF system. Left: first modal shape $\{\Psi\}_1$, associated to natural frequency $\overline{\omega}_1$. Right: second modal shape $\{\Psi\}_2$, associated to natural frequency $\overline{\omega}_2$.

specialized bibliography [43, 44] for further information.

2.6.3. Distributed-Parameter Systems

The previous section presented the basic theory to describe vibration phenomena where vibrating elements, the masses, are discrete. These systems could be regarded as rigid elements (the masses) interconnected by other elastic mass-less elements that provide the system's stiffness. Thus, the model neglects the elastic elements' mass. When the elastic elements' mass cannot be neglected, the discrete system fails, and a distributed-parameter system is needed. It should be noted that many particular systems could be modeled both as discrete and as distributed-parameter systems, depending on the analyses' objective [44].

Let us consider the case of a circular shaft in torsional vibration, or any elongated solid where the torsion of Saint-Venant is valid (warping terms neglected), like long bars with uniform solid-cross-sections. In these cases, the torsional moment in a cross-section is proportional to the rate of twist at that section [46]. That is

$$M(x,t) = GJ\frac{\partial\theta}{\partial x}(x,t), \tag{2.26}$$

where $M(x,t)$ is the torsional moment at time t and section defined by the coordinate x (coordinate along the longitudinal axis), G is the material's elastic shear modulus, J is the torsional constant in units of m^4, and $\theta(x,t)$ is the angle of twist of section x at time t. By applying second's Newton's Law to a

20

differential element without external loading, and substituting equation (2.26) into it we obtain the governing equation of motion [35, 44]

$$GJ\frac{\partial^2\theta}{\partial x^2}(x,t) = \rho I_p\frac{\partial^2\theta}{\partial t^2}(x,t), 0 < x < L \tag{2.27}$$

where ρ is the material's density, I_p is the polar moment of inertia in units of m^4, and L is the shaft's length.

By observing the partial differential equation (2.27), we can try solutions of the form

$$\theta(x,t) = \phi_x(x)Y_t(t),$$

where ϕ_x is a function that only depends on position x, and Y_t is a function that only depends on time t, and obtain

$$\frac{\phi_x''}{\phi_x} = \frac{1}{c_s^2}\frac{\ddot{Y_t}}{Y_t} = -\gamma^2,$$

where a dot over the magnitude indicates derivation over time t, and a quotation mark indicates derivation over position x, $c_s^2 = GJ/\rho I_p$, and γ^2 is a positive constant (γ usually called wavenumber).

Now, by trying sinusoidal solutions of $\phi_x(x)$ and $Y_t(t)$, we find the solution of equation (2.27)

$$\theta(x,t) = [A_1\sin(\gamma x) + A_2\cos(\gamma x)][B_1\sin(\omega t) + B_2\cos(\omega t)], \tag{2.28}$$

where $\omega^2 = c_s^2\gamma^2$, A_1 and A_2 are constants that depend on the shaft's boundary conditions given at $x = 0$ and $x = L$, and B_1 and B_2 are constants that depend on the initial shaft's conditions.

For a shaft pinned at both ends, we have

$$\theta(x = 0, t) = 0 \Rightarrow A_2\cos(\gamma 0) = 0 \Rightarrow A_2 = 0,$$

and

$$\theta(x = L, t) = 0 \Rightarrow A_1\sin(\gamma L) = 0 \Rightarrow \gamma_n = \frac{n\pi}{L}, \text{with } n = 1, 2, 3, ...$$

As seen in the previous expression, there is an infinite number of solutions, given by the family γ_n, that satisfy the boundary conditions, where n is the modal number and takes the values $1, 2, 3, \dots$. These are the infinite modes of vibration, whose shapes are given by introducing the γ_n solution into equation (2.28), which yields

$$\phi_{x,n}(x) = A_2 \sin\left(\frac{n\pi x}{L}\right)$$

where A_2 is an undefined real constant. Note that the modal shapes correspond in this case to sine functions of increasing argument, all being multiples of γ_1. For each nth mode of vibration, there is a corresponding frequency of vibration ω_n, given by the definition of ω; thus the frequency of vibration of each mode is given by

$$\omega_n^2 = \left(\frac{n\pi}{L}\right)^2 \frac{GJ}{\rho I_p}, \ n = 1, 2, 3, \dots \tag{2.29}$$

It should be noted that the problem of a circular shaft in torsional vibration is analogous to a thin rod in axial vibration, and also to a string in transverse vibration [44]; they all consist of solving the same second-order partial differential equation (2.27), with the involved coordinates having a different physical meaning, and using a different set of physical parameters. For the case of the rod in axial vibration, we only need to substitute, in the equation (2.29), stiffness GJ for EA, and I_p for A, with E being the Young's modulus of elasticity, and A the cross-section area. Also, we can compare the circular shaft in torsional vibration (and the rod in axial vibration) to the undamped SDOF system in free vibration. In equation (2.29), we could define a spring of stiffness $k \equiv \pi GJ/L$ and a mass with inertia term $m \equiv L\rho I_p/\pi$, to obtain $\omega_1^2 = k/m$, equal to equation (2.12).

Another typical distributed-parameter structural element is the beam in bending vibration. Most textbooks approach this problem by considering the Euler-Bernoulli beam theory, which neglects the rotational inertia with respect to the displacement inertia, and neglects the shear deformation with respect to the bending deformation [44]. This last hypothesis is valid for beams with length at least 10 times larger than their "bending" width (cross-section dimension) [44]. If this hypothesis is not met, it is necessary to consider the Timoshenko beam theory, which accounts for these effects.

The equation of motion of the Euler-Bernoulli beam is a fourth order partial

differential equation, and it is needed to define two boundary conditions at each beam's end to find the modal shapes and frequencies of vibration. For the case of pinned-pinned boundary conditions (free rotation and fixed displacement at both ends), the frequencies of vibration are [35]

$$\omega_n^2 = \left(\frac{n\pi}{L}\right)^4 \frac{EI}{\rho A}, \ n = 1, 2, 3, ... \tag{2.30}$$

with I being the principal moment of inertia that opposes bending, either I_y or I_z, with x being the coordinate in the axial direction, and y and z the other two coordinates associated to two principal directions forming a Cartesian system. For the case of free-free boundary conditions, the first (fundamental) frequency of vibration is

$$\omega_1^2 \cong \left(\frac{4.730}{L}\right)^4 \frac{EI}{\rho A}. \tag{2.31}$$

For "short" beams, the Euler-Bernoulli beam theory is not valid, and the Timoshenko beam must be considered. The interested reader should refer to the specialized bibliography [47, 48] for detailed information.

Finally, there is another case that matters for the purpose of this thesis, which is the case of bending-torsional vibration of axially loaded elongated solids (beams, columns). Lawrence [19] addresses this problem by considering bending vibration in either direction and torsional vibration, and the elements to be Euler-Bernoulli beams, where torsion is affected by both non-uniform (warping) and Saint-Venant torsion. If the element's cross-section is doubly-symmetric, the three equations of motion decouple and there are three decoupled mode families (two bending and one torsional). The first (fundamental) frequencies of vibration of these three modes, bending with respect to direction 2 (coordinate y), bending with respect to direction 3 (coordinate z), and torsional (θ) are given by

$$\omega_{y,1}^2 = \frac{1}{A\rho}\left[P\left(\frac{\pi}{L}\right)^2 + EI_z\left(\frac{\pi}{L}\right)^4\right], \tag{2.32}$$

$$\omega_{z,1}^2 = \frac{1}{A\rho}\left[P\left(\frac{\pi}{L}\right)^2 + EI_y\left(\frac{\pi}{L}\right)^4\right], \tag{2.33}$$

$$\omega_{\theta,1}^2 = \frac{1}{\rho I_p}\left[\frac{PI_p}{A}\left(\frac{\pi}{L}\right)^2 + EI_w\left(\frac{\pi}{L}\right)^4 + GJ\left(\frac{\pi}{L}\right)^2\right], \tag{2.34}$$

23

where P is the axial force, positive in tension, I_y and I_z are the principal moments of inertia with respect to directions 2 and 3, respectively, and I_w is the warping moment of inertia.

This topic is further studied in Chapter 3, but here it is necessary to note that the compressive axial load P tends to reduce the bending and torsional frequencies of vibration (because compression is negative). Therefore, this theory predicts reductions of the frequency of vibration as axial compression increases—within small enough (service) loads. However, recent research have observed the opposite behavior for concrete materials due to the nonlinear stiffening effect of concrete under compression [16, 17, 28]. A broader theory is needed to account for these findings, this is the Theory of Acoustoelasticity, which is presented in the next section.

2.7. Approaches for Stress Determination: Theory of Acoustoelasticity

2.7.1. Introduction

Experiments in metals and plastic materials carried out during the early years of the 20th Century proved the dependence between the solids' current stress and mechanical wave propagation [34]. These observations were not explained by the classical linear-elastic theory of materials, which, as shown in equations (2.6) and (2.7), predicts independence between wave speed and applied mechanical stress.

The topic moved forward by introducing linear empirical relationships between wave speed and stress, related by "acoustoelastic coefficients" [14, 15, 34]. However, it achieved a breakthrough when Hughes and Kelly [14] discovered that this applied stress-wave speed dependence can be explained by the fact that materials' constitutive equations (stress-strain relationships) may not be perfectly linear. In fact, slight material nonlinearity between stresses and strains would affect the speed in which mechanical waves travel through the deformed (stressed) medium.

Hughes and Kelly [14] obtained expressions of mechanical wave speed that depend on the solid's stress state. Their analysis started by considering the medium a Murnaghan solid [49]. The Murnaghan solid is a hyperelastic nonlin-

ear, homogeneous and isotropic solid material, in which stresses and strains are related by five elastic constants (see Chapter 3 for more details). These elastic constants are the two "second order" classic elastic constants, either the Lamé constants λ and μ, or the engineering constants E and ν, plus three "third order" elastic constants l, m, and n, later named "Murnaghan constants". In a solid body under uniaxial stress and considering a set of Cartesian axes, as the one given in Figure 2.2, the expressions of bulk wave propagation given by Hughes and Kelly [14] are

$$\rho_0 V_{11}^2 = \lambda + 2\mu + \frac{\sigma}{3K}\left[2l + \lambda + \frac{\lambda + \mu}{\mu}\left(4m + 4\lambda + 10\mu\right)\right] \quad (2.35)$$

$$\rho_0 V_{12}^2 = \rho_0 V_{13}^2 = \mu + \frac{\sigma}{3K}\left(m + \frac{\lambda n}{\mu} + 4\lambda + 4\mu\right) \quad (2.36)$$

$$\rho_0 V_{22}^2 = \rho_0 V_{33}^2 = \lambda + 2\mu + \frac{\sigma}{3K}\left[2l - \frac{2\lambda}{\mu}\left(m + \lambda + 2\mu\right)\right] \quad (2.37)$$

$$\rho_0 V_{21}^2 = \rho_0 V_{31}^2 = \mu + \frac{\sigma}{3K}\left(m + \frac{\lambda n}{4\mu} + \lambda + 2\mu\right) \quad (2.38)$$

$$\rho_0 V_{23}^2 = \rho_0 V_{32}^2 = \mu + \frac{\sigma}{3K}\left(m - \frac{\lambda + \mu}{2\mu}n - 2\lambda\right) \quad (2.39)$$

where ρ_0 is the material's density in the undeformed state, $K = \lambda + 2\mu/3$, and σ is the applied uniaxial stress along direction 1, equivalent to $\mathbb{T}_{11}$, as per equations (2.1) and (2.2). In equations (2.35) to (2.39), the bulk wave speed magnitudes V_{ij} correspond to a wave propagating parallel to direction i and polarized in direction j, with $i, j \in \{1, 2, 3\}$; thus, wave speeds with equal subindices correspond to P-waves and with different subindices correspond to S-waves.

With the equations posed by Hughes and Kelly [14], the research and applications that followed, involving acoustoelasticity, initially focused on assessing structures made of metal and polymer [29–32, 50–54]. These satisfactory research gave way to acoustoelastic analysis and characterization of more complex materials, such as concrete or rock [16–18, 20, 28, 33, 55–70].

2.7.2. Classical nonlinear (acoustoelastic) characterization of rock and concrete

Despite the fact of having a 3-D model given by the elastic Murnaghan solid model, capable of explaining the observed acoustoelastic effects, many research have opted for considering a 1-D solid model, which is of course less general but equally accurate in the appropriate conditions, and easier to manage. This model, known as the "classical nonlinear solid", is defined by the nonlinear-elastic constitutive equation

$$\sigma = E(1 + \beta\varepsilon + \delta\varepsilon^2 + ...)\varepsilon, \tag{2.40}$$

where σ is the stress in the material, associated to a certain plane and direction, ε is the strain associated to the same plane and direction, E is some elastic constant, and β, δ,... are nonlinear elastic constants. Attention should be paid when using equation (2.40), as it is a 1-D simplification of a more complex 3-D general problem. In particular, the material elastic constants E, β, δ,... have one physical meaning if equation (2.40) represents an elongated solid (a "bar" with one dimension much larger than the other two) composed of a nonlinear material, or a different one if it represents an infinite medium. The former case can be used to study the problem of a vibrating nonlinear solid bar, whereas the latter case is used for a bulk wave traveling through the nonlinear solid. For the latter case, and to distinguish it from the bar, let us rewrite the equation

$$\sigma = E_{bulk}(1 + \beta_{bulk}\varepsilon + \delta_{bulk}\varepsilon^2 + ...)\varepsilon. \tag{2.41}$$

where $E_{bulk} = E(1-\nu)(1+\nu)^{-1}(1-2\nu)^{-1}$ for a P-wave, or $E_{bulk} = G$ for an S-wave (E, ν and G being the Young's modulus, Poisson's ratio and shear modulus of elasticity, respectively). Similarly, the nonlinear material parameters β, δ, are different depending on the conditions of the solid . For instance, Otrovsky and Johnson [71] have found the value of β_{bulk} in terms of the third order elastic constants

$$\beta_{bulk} = \frac{3}{2} + \frac{l+2m}{\lambda+2\mu}, \tag{2.42}$$

which is associated to "wave propagation conditions" (a wave traveling through an infinite medium); in the following chapters other β-values (namely β_E and β_G), associated to other conditions, are derived.

Before moving into the use of acoustoelasticity for current stress determination/monitoring, it is necessary to highlight that there are abundant studies regarding nonlinear parameter characterization; there have been developed a number of techniques that exploit the characteristic features observed in nonlinear materials, and allow characterizing β and δ-values; for example, higher harmonic generation, mixed frequency response, sub-harmonic generation and resonant frequency shift with amplitude of the forcing force [43, 44, 72–75]. These techniques rely on submitting the material to dynamic displacement (strain) fields of significant amplitudes in order to activate the material nonlinearity, and, in general, they have been applied onto solids in a quasistatic-unstressed rest state, i.e. no quasistatic external load. On the other hand, the whole point of this research is to study and develop NDE techniques capable of estimating the external quasistatic loads. Thus, the potential NDE techniques to be developed are applied onto the already stressed solid, state in which the overall material and structural behavior differs from the unstressed state (as shown in the following chapters).

2.7.3. Acoustoelasticity for stress determination in concrete

The fact that wave speed is stress sensitive holds the potential of being used for stress determination. In the last decade, several researchers have made efforts to develop NDE methods capable of determining current stress levels in concrete. During these years, the leading approach has been the use of the acoustoelastic effect using wave propagation techniques [16–18, 28, 55–61, 63–65, 67–70]. However, wave speed is also damage sensitive. In samples under uniaxial compression, researchers have found that the acoustoelastic effect dominates at stress-levels lower than around 30 % or 40 % of the concrete compressive strength, i.e. within the elastic regime. At higher stress levels the effect of damage (microcracking coalescence) starts to progressively dominate concrete behavior [18, 28, 67].

However, even within the "elastic regime" of concrete under compression, there exist minor viscoelastic [76] and micro-plastic effects [77], which can affect the acoustoelastic results. Therefore, concrete material classical nonlinear behavior and its applicability for stress determination are still under research. For instance, only very few studies have calculated the third order elastic con-

stants of concrete material [17, 64], as most researchers have characterized classical material nonlinearities using the 1-D approximation, i.e. the nonlinear parameter β_{bulk}, or even the empirical approach using "acoustoelastic coefficients" that relate stress to wave speed directly.

From among the mentioned research focused on acoustoelastic characterization in concrete materials for stress determination/monitoring, there are four of them of particular interest. Payan et al. [17] studied the ultrasonic wave speed stress-dependence of a cylindrical concrete specimen under quasi-static uniaxial compression, using the coda wave propagation technique, and determined the specimen's material Murnaghan constants. The novelty of their results, besides determining concrete Murnaghan constants for the first time, rely on their technique, which does not need to measure absolute wave speed values but only their variation during a loading test. Because the uncertainty of the variation of the wave speed is much lower than the uncertainty of the absolute wave speed, the obtained l, m and n results are more accurate. On the other hand, the use of the coda wave technique undertakes several debatable assumptions, for example, the fact that the coda waves are mainly S-waves, where rigorously they are not. Moreover, only one loading cycle is shown, so there is no assessment of how elastic the behavior is for an entire loading-and-unloading cycle. Nogueira and Rens [64] computed the Murnaghan constants of multiple concrete mixtures using a direct wave propagation technique, where the concrete was subjected to one cycle of applied compression loads. They do not assess the measurements uncertainty nor the elastic behavior either. Shokouhi et al. [18] studied the Rayleigh wave speed dependence of a concrete sample under uniaxial compression. They applied several loading and unloading cycles and were able to decouple the acoustoelastic effect from damage (microcracking) effects. They concluded that acoustoelastic phenomenon dominates the wave speed stress-dependence, showing a stiffening behavior, for stresses between 0 and 35 % of the concrete strength. Finally, Lundqvist and Rydén [20] studied the acoustoelastic effects of a large-scale post-tensioned concrete beam. The main distinction of their investigation is that they used vibration resonance instead of wave propagation to monitor acoustoelasticity. They found that the specimen's vibrational modal frequencies increased when modest levels of axial compression were applied (by tensing the tendons).

The use of resonance techniques, including bending and torsional modes, have been gaining attention to substantiate mainly the acoustoelastic effects,

and also nonlinear nonclassical material descriptions (material conditioning effects, hysteresis and damage in unstressed specimens) [72, 78–81]. This research is focused on material acoustoelasticity specifically for concrete under mechanical stress, so it does not consider broader nonclassical material parameters. The reader interested in nonclassical nonlinear material descriptions should refer to the specialized bibliography [72, 79–81].

The main advantage of using vibration frequency instead of wave speed is that the former is a global measurement, less affected by local material variability. On the other hand, the main drawback for vibration measurements is that frequency is affected by the test sample's boundary conditions whereas direct wave speed is not. The use of vibration frequency measurements to monitor stresses in concrete elements has not received much attention beyond the initial work by Lundqvist and Rydén [20]. Although Lundqvist and Rydén clearly demonstrate the acoustoelastic behavior in their beam sample, they do not provide a specific theoretical description of the physical phenomenon, and do not discuss factors that affect the frequency-stress relationship, such as the effect of boundary conditions, geometric nonlinearity or the effect of non-uniform torsion. This research expands and deepens the analysis on the use of frequency of vibration for acoustoelastic characterization and stress determination in concrete elements.

Chapter 3

Theoretical development and numerical analysis of the vibration of an elongated nonlinear solid

3.1. Introduction

Disclaimer: Most of the content in sections 3.2 and 3.4 of this chapter has been published in: A. Spalvier, L.D. Domenech, G. Cetrangolo, J.S. Popovics, "Torsional vibration technique for the acoustoelastic characterization of concrete, Materials and Structures, 53:7, 2020, https://doi.org/10.1617/s11527-020-1438-6.

This chapter contains the theoretical development necessary to understand the relationships between the elastic parameters of a solid, its stress state, and its frequency of vibration. The analysis considers the three affecting factors: geometric nonlinearity, non-uniform torsion (warping), and changing boundary conditions. These factors, which are often neglected without proper justification, could affect the frequency of vibration results depending on the properties of the sample. The analyses posed in this chapter consider all these factors together as a function of applied compressive stress. Then, they document the theoretical background and mathematical description to characterize the relationship between torsional frequency of vibration and compressive uniaxial loading. This chapter is therefore important to enable the developing test-

ing techniques capable of characterizing concrete nonlinearity, which would in turn, shed light on the field of nondestructive estimation of mechanical stresses in solids.

The specific objectives of this chapter are: to develop and analyze a theoretical description capable of explaining the frequency of vibration increments observed in concrete bars under uniaxial compression, to provide the theoretical formulation that could be promptly used to fit the experimental measurements of the following chapters, and to assess the possibility of using this formulation for stress determination of concrete structural members subjected to uniaxial external load.

3.2. Theory for the characterization of material nonlinearity using torsional vibration

This section examines nonlinear material properties of concrete members under uniaxial stress and details a testing method capable of characterizing material nonlinearity.

3.2.1. Quasi-static dynamic problem

Let us consider again the same elongated prismatic bar of dimensions L_1, L_2, and $L_3 = L_2$, shown in figure 2.2. Let us apply an external quasi-static load (P, tension positive) uniformly distributed on the prism's end faces, where the lateral faces have no displacement restrictions. These conditions create a quasi-static stress field with the non-null principal stress σ and strain ε acting along the longitudinal axis (direction 1).

Then, let us consider a dynamic stress field superimposed onto the previously applied quasi-static uniaxial stress field. The dynamic field corresponds to the fundamental torsional vibration mode acting along the longitudinal direction. Let us assume then that the quasi-static stress field from the applied compressive load deforms the solid creating displacements that are much greater than those caused by the dynamic stress field (vibration).

3.2.2. Vibration of the linear-elastic bar axially loaded

Let us first assume an axially loaded prismatic beam that is simply supported, with end-twists impeded, and composed of an isotropic and linear-elastic material. The theory of linear elasticity under small strains and the double symmetry of the section leads to the existence of four uncoupled vibration mode families: one longitudinal, two transversal (bending), and one torsional. The torsional equation of motion is [19]

$$\frac{\partial^2 C_\theta}{\partial t} + \frac{n^2\pi^2}{\rho L_1}\left[\frac{1}{I_p}\left(GJ + \frac{\pi^2 E I_w}{L_1^2}\right) + E\varepsilon\right]C_\theta = 0, \qquad (3.1)$$

where ρ is the density of the material, I_p is the polar moment of inertia, J is the torsional constant, I_w is the warping moment of inertia, E is the Young's modulus, G is the shear modulus of elasticity, n is the modal number, and ε is the axial strain (tension positive) produced by the external load in a quasi-static state. C_θ is a function that describes the amplitude of vibration with time, where $\theta(x,t) = C_\theta \sin(n\pi x/L_1)$ and θ is the angle of twist. The sine function in the product represents the vibrational mode shape and x and t are the position along the bar's longitudinal axis and time variables, respectively.

Solving equation 3.1 for $n = 1$, yields the frequency of the fundamental torsional mode $\omega_{1,lin}$

$$\omega_{1,lin}(\varepsilon)^2 = \frac{1}{\rho I_p}\left[E I_p \varepsilon\left(\frac{\pi}{L_1}\right)^2 + E I_w\left(\frac{\pi}{L_1}\right)^4 + GJ\left(\frac{\pi}{L_1}\right)^2\right], \qquad (3.2)$$

where "lin" stands for "linear material"[1]. The first term within the brackets corresponds to the effect of geometric nonlinearity, known as the P–δ effect. Note that compressive strains ($\varepsilon < 0$) caused by the quasistatic load reduce the fundamental frequency of vibration. This effect has also been named as the "string effect", because, as it occurs in a string, uniaxial tension increases the natural frequency of vibration and compression reduces it. The second term considers the non-uniform torsion or warping effect, whose consideration is very important in open-sections, such as those used for steel structures

---

[1]It should be noted that "linear material" refers to the linearity between the 2nd Piola stress tensor $\mathbb{S}$ and the Lagrange strain tensor $\mathbb{E}$. Nevertheless, $\omega_{1,lin}$ is affected by the geometric nonlinearity introduced by considering the finite deformation ε, produced by the external axial load.

like I-beams, but not as much for solid-section members, such as those used in concrete structures, usually rectangles or circles. Finally, the third term represents Saint-Venant classical torsion theory. A more detailed discussion of this topic is given in the following section, where the quantitative influence of these three factors is analyzed.

3.2.3. Acoustoelasticity: a nonlinear material model

This denomination origins from the fact that the nonlinearity between stresses and strains can be addressed by considering strain dependent (or stress dependent) elastic "constants", or "parameters". For example, the nonlinear relationship of stresses and strains in a bar under uniaxial stress can be modeled using a parabolic relationship, where the applied stress σ and the observed strain ε are defined by

$$\sigma(\varepsilon) = E_0(1 + \beta_E \varepsilon)\varepsilon. \tag{3.3}$$

In equation (3.3), β_E is a nonlinear elastic parameter associated to the strain dependency of the Young's modulus E. The subindex 0 has been added to the Young's modulus E_0 to indicate the fact that it is the Young's modulus of the solid in the undeformed state. Thus, let us define the "instantaneous" Young's modulus E_ε, which is strain and stress dependent, which comes from deriving the stress with respect to strain, i.e.

$$E_\varepsilon(\varepsilon) = \frac{\partial \sigma(\varepsilon)}{\partial \varepsilon} = E_0(1 + 2\beta_E \varepsilon). \tag{3.4}$$

Figure 3.1 contains a graph that shows a possible nonlinear relationship between stress and strain; note there the varying slope which means a varying instantaneous Young's modulus E_ε.

The example of nonlinear material shown in figure 3.1 exhibits a stiffening material behavior, i.e., as stresses increase, strains also increase but to a lower extent. The opposite case is when instantaneous Young's modulus decreases with increasing stresses, that would be the case of a softening behavior. A nonlinear stiffening effect has been previously observed in concrete under uniaxial compression by various researchers [16, 17, 28] for levels of compression lower than 30 % the failure load, i.e. where concrete behaves fundamentally elastically; material softening starts to control after achieving 50 % the failure
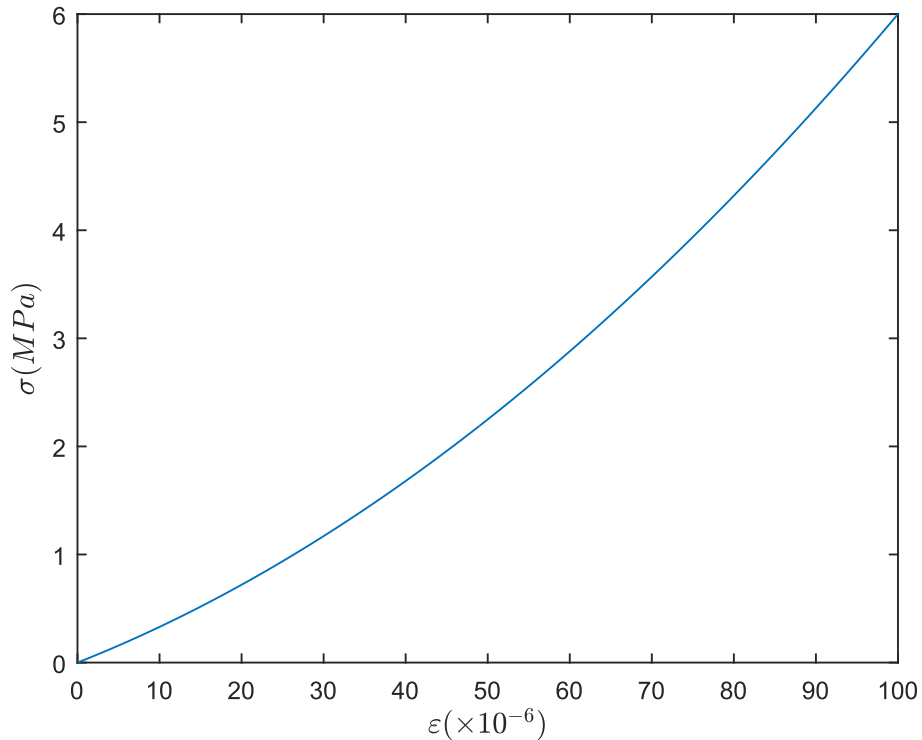
Figure 3.1: Nonlinear stress-strain generic relationship.

load [18, 28].

The equations (3.3) and (3.4) are simple expressions that allow modeling, with certain limitations, the dependency of P-waves propagating longitudinally, and the frequency of longitudinal vibration of an elongated solid, under uniaxial stress. This is a problem in which, the quasistatic uniaxial stress is applied first, the bar takes the associated strains, and then the dynamic event takes place (either a propagating wave or a resonance vibration). The velocity of wave propagation or the frequency of vibration are therefore affected because the material is pre-deformed, thus, behaving with an "effective" elastic parameter that controls the dynamic event; this effective parameter is the E_ε and not E_0.

The problem of a bar under uniaxial stress (pre-deformed) subjected to torsional vibration can be analyzed in the same manner. In pure torsion, the cross-sections of the bar are under pure shear (where warping is neglected, as it is demonstrated below in this section). Thus, equation (2.5) applies. However, because the vibration event occurs when the bar is pre-deformed it should be considered an "instantaneous" shear modulus G_ε, thus

$$\tau = G_\varepsilon \gamma_\tau, \tag{3.5}$$

and

$$G_\varepsilon(\varepsilon) = \frac{\partial \tau(\varepsilon)}{\partial \gamma_\tau} = G_0(1 + \beta_G \varepsilon), \tag{3.6}$$

with G_0 being the shear modulus at the unstrained state, and β_G being a nonlinear elastic parameter associated with the stress and strain dependency of the shear modulus G.

Note that the present model poses strain dependent Young's modulus and shear elastic modulus that vary linearly with strain. This fact comes from considering only the square terms of the strain in the constitutive relationships. Other researchers [76] have considered higher powers of strains; these are certainly necessary for very soft materials, such as rubber, or for concrete to model a wider range of the stress-strain relationship where both stiffening and softening occurs at different stress levels. For our case, below 30 - 40 % of concrete compressive strength, the present assumption is reasonable.

The present theoretical approach, which provided equation (3.4) and (3.6) presents several advantages and disadvantages. The main advantage is its simplicity, which allows addressing acoustoelastic dynamic problems by considering the strain dependent elastic parameters E_ε and G_ε instead of the usual E and G. On the other hand, the theoretical development is not general as it is a 1D version of a more complex 3D constitutive equation. Thus, there are many acoustoelastic-dynamic phenomena that cannot be described using this approach. For example, this approach cannot describe P or S wave traveling through the solid bar perpendicularly to the direction of the applied uniaxial stress. To study the full 3D problem it is necessary consider the complete 3D constitutive equation.

From the literature [17, 20, 56] and from this investigation's experiments, it has been observed that the E_ε and G_ε increase around 2–3 % due to the acoustoelastic effect. These apply to concrete bars submitted to compressive strains of around 100×10^{-6}. Considering these increments, let us go back to equation (3.2) to inspect how the three factors—geometric nonlinearity, non-uniform torsion (warping) and Saint–Venant torsion—affect torsional angular frequency of vibration.

To simplify the interpretation of 3.2, consider the general aspect-ratio

relationship $L_2 = \alpha L_1$ (for experiments in Chapters 4 and 5, the samples had $\alpha = 1/4$). Let us calculate the involved parameters using their definitions, thus: $I_p = L_2^4/6 = \alpha^4 L_1^4/6$, $J \cong 0.1338 L_2^4 = 0.1338 \alpha^4 L_1^4$, and $I_w \cong 1.34 \times 10^{-4} L_2^6 = 1.34 \times 10^{-4} \alpha^6 L_1^6$. Rearranging 3.2 and substituting the calculated terms within the brackets gives

$$\omega_1(\varepsilon)^2 = \frac{\pi^2}{\rho L_1^2} \left[E_\varepsilon(\varepsilon)\varepsilon + E_\varepsilon(\varepsilon)\frac{I_w}{I_p}\left(\frac{\pi}{L_1}\right)^2 + G_\varepsilon(\varepsilon)\frac{J}{I_p} \right] \tag{3.7}$$

$$\cong \frac{\pi^2}{\rho L_1^2} \left[E_\varepsilon(\varepsilon)\varepsilon + 7.94 \times 10^{-3}\alpha^2 E_\varepsilon(\varepsilon) + 0.80 G_\varepsilon(\varepsilon) \right]. \tag{3.8}$$

Note in equation (3.7) that the subindex "lin" in ω_1 has been removed. Also this equation shows that only the warping term (second term within the brackets) depends on the aspect-ratio parameter α; this is an interesting characteristic that gains importance in order to extend these laboratory results to field tests.

Now let us consider the typical acoustoelastic increments of 2 % for a uniaxial strain of $\varepsilon^* = -100 \times 10^{-6}$ (note the negative sign because it is compression). In other words, consider $E_\varepsilon(\varepsilon^*) = 1.02E_0$ and $G_\varepsilon(\varepsilon^*) = 1.02G_0$ where the sub-index 0 stands for undeformed (zero strain) state. By substituting those expressions into equation (3.8) we obtain

$$\omega_1(\varepsilon^*)^2 = \frac{\pi^2}{\rho L_1^2} \left[-1.02 \times 10^{-4}E_0 + 8.1 \times 10^{-4}\alpha^2 E_0 + 0.82G_0 \right]. \tag{3.9}$$

Considering that $G_0 = E_0/(2(1+\nu_0))$, from equation (2.4), and that $\nu_0 \cong 0.2$ (typical Poisson's ratio for concrete), we get $E_0 \cong 2.4G_0$. Therefore, we see in equation (3.9) that the Saint–Venant term (third term within the brackets) is several orders of magnitude higher than the geometric nonlinearity (first term within the brackets). This relationship is true for all values of uniaxial compressive strain within concrete's elastic range and is independent of the value of α. The warping term (second term within the brackets) affects the Saint–Venant term by more than 1 % only for values of α higher than 2; i.e., affects if $L_2 > 2L_1$. Note that typical elongated structural elements, such as columns and beams, have α-values between 0.5 to 0.03, much lower than 2; thus, the warping term can be neglected in these cases. This fact was

validated with a numerical simulation presented in section 3.4. Therefore, it becomes clear that the effects on angular frequency produced by geometric nonlinearity and warping, and also the influence of sample aspect ratio, can be neglected with respect to the acoustoelastic increments of frequency resulting from the Saint–Venant torsional term. Under this model, the uniaxial quasi-static strains are small enough to neglect the nonlinear geometric effects but large enough to activate the material nonlinearity.

Based on the previous discussion, let us consider a simplification of equation 3.7, where both the geometric nonlinearity and warping terms have been neglected. Thus, the strain-dependent fundamental ($n = 1$) torsional angular frequency $\omega_1(\varepsilon)$ is

$$\omega_1(\varepsilon) = 2\pi f_1(\varepsilon) = \frac{\pi}{L_1}\sqrt{\frac{G_\varepsilon(\varepsilon)J}{\rho I_p}}, \tag{3.10}$$

where f_1 is the fundamental frequency of torsional vibration. Thus, by squaring 3.10 we obtain

$$\omega_1(\varepsilon)^2 = (2\pi f_1(\varepsilon))^2 = \left(\frac{\pi}{L_1}\right)^2 \frac{G_\varepsilon(\varepsilon)J}{\rho I_p}. \tag{3.11}$$

Let us then normalize the strain dependent fundamental frequency $f_1(\varepsilon)$ with respect to the condition in which $\varepsilon = 0$, i.e. the undeformed state, thus

$$\frac{f_1(\varepsilon)^2}{f_1(0)^2} = \frac{\omega_1(\varepsilon)^2}{\omega_1(0)^2} = \frac{G_\varepsilon(\varepsilon)}{G_0(0)}. \tag{3.12}$$

Now let us substitute the definition of G_ε given in equation (3.6) into equation (3.12), to obtain

$$f_1(\varepsilon)^2 = (1 + \beta_G \varepsilon) f_1(0)^2. \tag{3.13}$$

Note that by carrying out experiments in which a prismatic bar is axially loaded, it is possible to measure the axial strains ε and the fundamental torsional frequency of vibration $f_1(\varepsilon)$ for the unloaded case and at least one distinct level of ε; these values allow computing the nonlinear (shear) parameter β_G by carrying out a simple linear regression. Thus, equation (3.13) governs the set of experiments presented in Chapters 4 and 5.

Note that an analogous analytical procedure can be deduced by considering the longitudinal mode of vibration of the bar instead of the torsional mode.

In this new case, we get

$$\frac{f_{L,1}(\varepsilon)^2}{f_{L,1}(0)^2} = \frac{\omega_{L,1}(\varepsilon)^2}{\omega_{L,1}(0)^2} = \frac{E_\varepsilon(\varepsilon)}{E_0(0)}, \tag{3.14}$$

where the subindex L has been added to indicate it corresponds to the "longitudinal" mode. Now using the definition of E_ε given by equation (3.4) and substituting it into equation (3.14), we get

$$f_{L,1}(\varepsilon)^2 = (1 + 2\beta_E \varepsilon)\, f_{L,1}(0)^2. \tag{3.15}$$

Equation (3.15) can be used, in theory, to compute β_E by measuring the change of frequency of the longitudinal mode during a uniaxial loading test. However, there are two reasons why parameter β_E was not investigated any further. First, its experimental characterization is much more cumbersome as it requires access to their end faces to attach transducers, apply impacts, and yet assure good boundary condition characterization. In second place, our preliminary tests showed that the application of the load modifies the axial boundary conditions too much, so that the model fails to fully explain the actual behavior of the bar. This effect of changing boundary condition also affects the torsional mode, but to a much lesser extent. To solve this problem, a correction procedure is employed so that the proposed model can be used satisfactorily.

3.2.4. The effect of changing boundary conditions

Consideration of changing boundary conditions of the system is needed for some laboratory or field situations. Equation (3.10) was obtained assuming that the prismatic bar was simply supported with impeded (fixed) twist at the ends; however, the boundary conditions of a given element will likely differ from this idealized condition. For example, in the experiments described in Chapters 4 and 5, the samples were not simply supported; a more appropriate model for these experiments would be to consider the prismatic bar with matched torsional springs, with a spring constant that depends on the uniaxial stress $k = k(\sigma)$.

Let us neglect the geometric nonlinearity and non-uniform torsion, the general equation that governs the torsional vibration phenomenon of a bar with uniform section is [35]

$$\frac{\partial^2 \theta}{\partial x^2} - \frac{\rho I_p}{GJ}\frac{\partial^2 \theta}{\partial t^2} = 0. \tag{3.16}$$

Under these new boundary conditions, we find the system's frequencies by solving

$$\frac{2kL_1}{GJ\left(\frac{\omega}{c_s}L_1\right) - \frac{(kL_1)^2}{GJ\left(\frac{\omega}{c_s}L_1\right)}} = \tan\left(\frac{\omega}{c_s}L_1\right) \tag{3.17}$$

where $c_s^2 = GJ/(\rho I_p)$. The full derivation of equation (3.17) is provided in Appendix 3. Equation (3.17) is graphically represented in Figure 3.2, where the left side of equation (3.17) corresponds to the blue curve and the right side to the red curve. The values of ω that satisfy equation (3.17) are $\hat{\omega}_i$ with $i = 0, 1, 2, ...$ These solutions are indicated by the points of intersection of the blue and red curves in Figure 3.2, and allow computing ω for fixed values of L_1 and c_s. Note that to model the cases in which the twists at the ends are either fully restricted (fixed-fixed) or fully unrestricted (free-free), these situations are described by substituting $k \to \infty$ and $k = 0$, respectively, in equation (3.17). In both cases, the left side of equation (3.17) becomes zero; in other words, the blue curve becomes horizontal and overlapped with the x-axis. Therefore, it is clear that the fixed-fixed and free-free cases produce one set of matching solutions $\hat{\omega}_i = \omega_i$. For other values of k, there is a low-frequency root, $\hat{\omega}_0$, that corresponds to a "nearly rigid vibration" of the bar due to the presence of the springs at the end boundaries. Moreover the fundamental frequency increases from ω_1 to $\hat{\omega}_1$. Figure 3.2 shows these two effects.

Equation (3.17) enables the calculation of both k and G by measuring $\hat{\omega}_0$ and $\hat{\omega}_1$ at a given level of compressive stress. The significance of this procedure is explained the Materials and Methods section of Chapter 4.

3.3. Derivation of β_E and β_G as a function of the third order elastic constants

The nonlinear parameters β_G and β_E were presented in section 3.2.3, where their physical meaning and simplicity have been shown. The use of β_G for concrete nonlinear characterization is developed in Chapters 4 and 5. However, as stated before, the β_E and β_G nonlinear elastic parameters are very useful
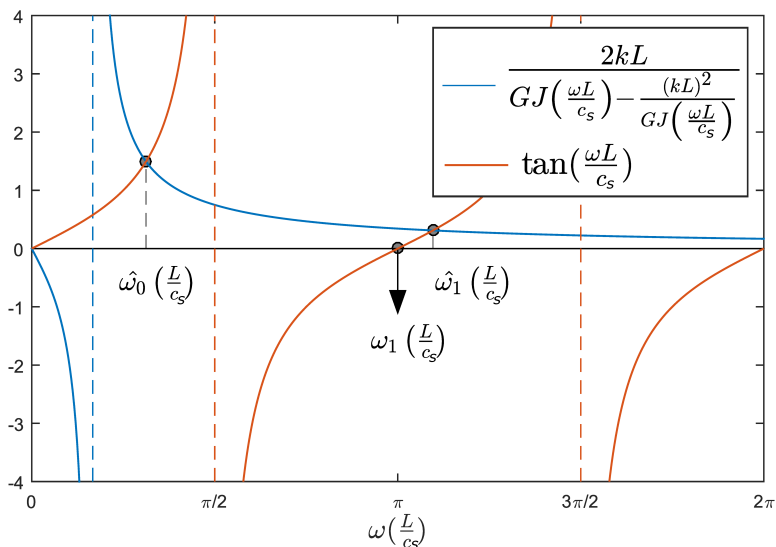
Figure 3.2: Graphical representations of the functions in equation (3.17) for arbitrary values of G, J, L, and k. The dots represent solutions to 3.17 ω_1, $\hat{\omega}_1$, and $\hat{\omega}_0$. Dashed lines represent values where the equation (3.17) becomes undefined.

to explain certain nonlinear behavior of elongated solids (bars), and they are not general elastic parameters capable of explaining a wider variety of situations, like for example waves propagating in solid media under stress. As introduced in Chapter 2, a general approach was taken by Hughes and Kelly [14] to explain the stress dependence of bulk wave speed. For a solid under uniaxial stress, they established the relationships between all possible bulk wave propagating modes in the solid and the uniaxial stress value (see equations (2.35) through (2.39)). To that end, they considered a nonlinear solid model previously posed by Murnaghan [49], which, for the case of an (initially) isotropic and homogeneous material, the elastic behavior can be fully described by the two traditional elastic constants, plus three additional elastic constants, l, m, and n, known as the third order elastic constants. All research regarding acoustoelasticity and material nonlinearity, refer directly or indirectly to these third order elastic constants. This section derives the analytical relationships between the β_G and β_E and the third order elastic constants l, m, and n. This theoretical development is a key topic of this thesis as it enables results comparison against the existing literature.

The analysis consists of considering a prismatic bar composed of an elastic nonlinear material. The first step is to apply a finite deformation compatible with a uniaxial stress state due to a quasistatic load. The second step consists

40

of applying a small deformation starting from the position resulting from the first step. The second deformation field represents the vibration of the solid, which, since it happens to be several orders of magnitude smaller than the initial quasistatic deformation, it is possible to accept the hypothesis of linearity (its effects are obtained by linearization around the first state). The position that attains the application of the second step is not actually calculated; instead, only the rigidity of the element to take that deformation is calculated, and that rigidity is used to derive the nonlinear parameters β_G and β_E with respect to l, m, and n.

3.3.1. Derivation of β_E

The derivation starts by considering an elongated prismatic solid of dimensions L_1, L_2 and L_3, where $L_1 >> L_2 = L_3$. Consider a system of Cartesian axes 1, 2 and 3, in which direction 1 corresponds to the longitudinal axis of an elongated prismatic bar, and axes 2 and 3 are perpendicular to axis 1. The parameters X_1, X_2 and X_3, are the material coordinates (Lagrange coordinates) that determine the position of each material point in the reference configuration; this reference configuration is considered to be equal to the undeformed state of the solid prism. The parameters x_1, x_2 and x_3 are the spatial coordinates (Euler coordinates) that indicate the resulting position of the material points after the deformation has occurred.

Let us apply a deformation (displacement) field compatible with a uniaxial stress state produced by a dead load of value P uniformly acting onto both end faces. Figure 2.2 depicts the prismatic bar, the Cartesian axes and geometric dimensions.

The mentioned deformation field is defined by

$$x_1 = aX_1 \tag{3.18}$$

$$x_2 = bX_2 \tag{3.19}$$

$$x_3 = bX_3, \tag{3.20}$$

where a is the longitudinal stretch, along direction 1, and b corresponds to the lateral stretch along both directions 2 and 3. Note that a and b are dimensionless magnitudes that represent a type of "strain", which we have called

41

"stretch" in order to differentiate them from the other magnitudes of strain. The definition of a and b are given implicitly by equations (3.18)-(3.20); this is, they transform the position of a particle in the initial configuration to the position of that particle in the deformed configuration.

Figure 3.3 shows a diagram of the deformation field compatible with a uniaxial stress applied along axis 1.
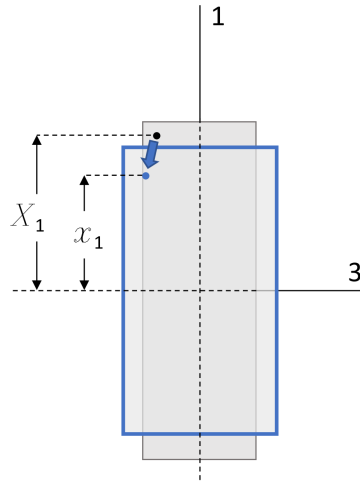
Figure 3.3: Undeformed prismatic bar with black thin outline and deformed prismatic bar with blue thick outline. A generic material point indicated by the black dot moves to the blue dot after the deformation, as indicated by the arrow.

The deformation field χ becomes defined by

$$\chi = \begin{bmatrix} x_1 \\ x_2 \\ x_3 \end{bmatrix} = \begin{bmatrix} aX_1 \\ bX_2 \\ bX_3 \end{bmatrix}. \tag{3.21}$$

The deformation gradient $\mathbb{F}$ becomes

$$\mathbb{F} = \nabla_m \chi = \begin{bmatrix} a & 0 & 0 \\ 0 & b & 0 \\ 0 & 0 & b \end{bmatrix}, \tag{3.22}$$

where ∇_m implies the gradient operation in material coordinates.

Thus, the right Cauchy-Green strain tensor $\mathbb{C}$ becomes

$$\mathbb{C} = \mathbb{F}^T \mathbb{F} = \begin{bmatrix} a^2 & 0 & 0 \\ 0 & b^2 & 0 \\ 0 & 0 & b^2 \end{bmatrix}. \tag{3.23}$$

The strain tensor $\mathbb{C}$ yields the square of the local distances in a given material point due to the deformation. With $\mathbb{C}$, the Green-Lagrange strain tensor $\mathbb{E}$ can be calculated as

$$\mathbb{E} = \frac{1}{2}\left(\mathbb{C} - \mathbb{I}\right) = \begin{bmatrix} \frac{a^2-1}{2} & 0 & 0 \\ 0 & \frac{b^2-1}{2} & 0 \\ 0 & 0 & \frac{b^2-1}{2} \end{bmatrix}, \tag{3.24}$$

where $\mathbb{I}$ is the identity tensor. The strain tensor $\mathbb{E}$ yields one half of the square of the local distance changes.

Once the strain tensor is computed, it is necessary to relate the development of the strains with the stresses, which, for this case, a nonlinear relationship is to be considered. The constitutive equation of the material becomes defined from the strain energy density ψ, in which a given stress at a specific plane and direction is calculated as the derivative of the strain energy density with respect to the strain at that same plane and direction, thus

$$\mathbb{S}_{ij} = \frac{\partial \psi}{\partial \mathbb{E}_{ij}}, \tag{3.25}$$

where $\mathbb{S}$ is the Cosserat stress tensor (or second Piola-Kirchhoff stress tensor) where i, j take the values $1, 2$, or 3.

At this point it is needed to assume some specific strain energy density function that describes adequately the experimental observations and characteristics to be modeled. To this end, let us consider the material to be an hyperelastic solid material of Murnaghan, which is the same hypothesis taken by Hughes y Kelly [14] to derive the equations (2.35) through (2.39). The Murnaghan strain energy density is defined as

$$\psi = \frac{1}{2}(\lambda + 2\mu)I_1^2 - 2\mu I_2 + \frac{1}{3}(l + 2m)I_1^3 - 2mI_1 I_2 + nI_3, \tag{3.26}$$

where I_1, I_2 and I_3 are the three invariants of the strain tensor $\mathbb{E}$, defined as

$$I_1 = \text{tr}(\mathbb{E}) \tag{3.27}$$

$$I_2 = \frac{1}{2}\left[\text{tr}^2(\mathbb{E}) - \text{tr}(\mathbb{E}^2)\right] \tag{3.28}$$

$$I_3 = \det(\mathbb{E}). \tag{3.29}$$

The Murnaghan strain energy density function contains third order terms, i.e. cubic terms, which produce a nonlinear constitutive relationship; these terms are not included in the traditional strain energy functions that produce linear stress-strain relationship. Once the specific strain energy function ψ is known as a function of the elastic constants of the solid (λ, μ, l, m and n), the stress tensor $\mathbb{S}$ can be calculated by applying equation (3.25). Then it is possible to calculate the Cauchy stress tensor in its material version σ_m using

$$\sigma_m = \mathbb{F}J_{\mathbb{F}}^{-1}\mathbb{S}\mathbb{F}^T, \tag{3.30}$$

with $J_{\mathbb{F}} = \det(\mathbb{F})$. The Cauchy stress tensor σ describes the stresses being taken by the solid in its present configuration[1], i.e., in the deformed configuration. Specifically, the stress tensor σ establishes the stress vector defined in each point x_1, x_2, x_3 of the deformed solid at certain plane defined by its normal vector. The Cauchy stress tensor in its material version σ_m yields the stress of the solid at the deformed configuration, in a point and plane given by the material coordinates X_1, X_2, X_3. It is easier to work with σ_m instead of σ because the undeformed dimensions are known, and they remain unchanged by definition, and the opposite happens to the deformed dimensions.

Each element of the stress tensor σ_m is a function of the five elastic constants and of the stretch values a y b. In particular, we need to know $\sigma_{m,11}$ and $\sigma_{m,22}$, which are

$$\sigma_{m,11} = \{a[(\lambda/2 + \mu)(a^2 + 2b^2 - 3) - 2m(2(a^2/2 - 1/2)(b^2/2 - 1/2)$$
$$+ (b^2/2 - 1/2)^2) + n(b^2/2 - 1/2)^2 - 2\mu(b^2 - 1) + 3(l/3 + (2m)/3)(a^2/2 + b^2$$
$$- 3/2)^2 - 2m(b^2 - 1)(a^2/2 + b^2 - 3/2)]\}/b^2, \tag{3.31}$$

and

---

[1]Note that the same symbol, σ, has been adopted here to express the Cauchy stress tensor, and elsewhere in this thesis to express the uniaxial stress in a bar.

$$\sigma_{m,22} = ((\lambda/2 + \mu)(a^2 + 2b^2 - 3) - 2m(2(a^2/2 - 1/2)(b^2/2 - 1/2)$$
$$+(b^2/2 - 1/2)^2) - 2\mu(a^2/2 + b^2/2 - 1) + 3(l/3 + (2m)/3)(a^2/2 + b^2 - 3/2)^2$$
$$-2m(a^2/2 + b^2 - 3/2)(a^2/2 + b^2/2 - 1) + n(a^2/2 - 1/2)(b^2/2 - 1/2))/a. \tag{3.32}$$

There are also two boundary conditions associated to the considered uni-axial stress state. These need to be applied now in order to calculate a and b. The first boundary condition establishes that the lateral faces are free from normal stresses, thus

$$\sigma_{m,22} = 0,$$

which implies equating equation (3.32) to zero. From this boundary condition we produce a relationship between a and b, given by

$$b = [4\lambda - 12l - 2m - n + 4\mu + 4a^2l - 2a^2m + a^2n$$
$$-(4a^4m^2 - 4a^4mn - 24la^4m + a^4n^2 + 8la^4n - 32a^2\lambda m$$
$$+8a^2\lambda n - 8a^2m^2 + 8a^2mn - 16a^2m\mu + 48la^2m - 2a^2n^2$$
$$+8a^2n\mu - 16la^2n + 32la^2\mu + 16\lambda^2 + 32\lambda m$$
$$-8\lambda n + 32\lambda\mu + 4m^2 - 4mn + 16m\mu - 24lm + n^2$$
$$-8n\mu + 8ln + 16\mu^2 - 32l\mu)^{1/2}]^{1/2}/(2(-2l - m)^{1/2}). \tag{3.33}$$

The second boundary condition corresponds to the applied uniaxial load on the end faces of the specimen, thus

$$\sigma_{m,11} = \frac{P}{(bL_2)^2}, \tag{3.34}$$

where P is the applied load that does not vary during the deformation. In other words, this implies assuming a situation where the load is constant, for example during a load-controlled loading test or in a column submitted principally to dead load. Figure 3.4 shows the boundary conditions values expressed with black dots or blue dots, in the undeformed and deformed configurations, respectively.

By applying this second boundary condition, we would obtain a relationship between the applied load P and the stretch value a. However, for our purposes, we do not need to actually apply this second boundary condition. Instead,
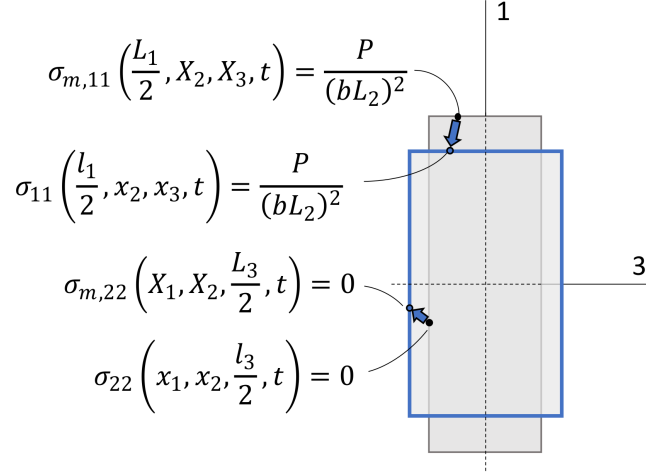
Figure 3.4: Diagram of the deformed prismatic solid showing the applied stress boundary conditions, where l_1 is the deformed length L_1.

let us use equation (3.33) and substitute it into equation (3.31) to obtain an expression of $\sigma_{m,11}$ as a function of a and of the five elastic constants, expressed as

$$\sigma_{m,11} = \sigma_{m,11}(a, \lambda, \mu, m, l, n). \tag{3.35}$$

The resulting equation is too long so it is omitted (see "T11" in the code in Appendix 2). It is needed to achieve a relationship between the stress $\sigma_{m,11}$ and the engineering strain ε_{11} expressed in an analogous form as the equation (3.3), i.e. to be a polynomial function of second order expressed as

$$\sigma_{m,11}(\varepsilon_{11}) = C_0 + C_1\varepsilon_{11} + C_2\varepsilon_{11}^2. \tag{3.36}$$

To this end, two more steps are followed. First, equation (3.35) needs to be expressed as a function of ε_{11} instead of as a function of a. Then a Taylor series expansion is carried out to equation (3.35) to achieve the form needed as in equation (3.36).

The first step consists then in obtaining the relationship between the engineering strain ε_{11} and the stretch a. Considering that the engineering strain ε_{11} is defined as

$$\varepsilon_{11} = \frac{l_1 - L_1}{L_1}, \tag{3.37}$$

with l_1 being the length of the deformed prism. Then, knowing that

$$l_1/2 = x_1 = aX_1$$

$$L_1/2 = X_1,$$

we obtain the wanted relationship

$$a = \varepsilon_{11} + 1. \tag{3.38}$$

By substituting equation (3.38) in (3.35) and carrying out the Taylor series expansion of second order around 0, we obtain the expression of equation (3.36), in which the coefficients C_0, C_1, y C_2 are obtained matching term to term:

$$C_0 = 0 \tag{3.39}$$

$$C_1 = \frac{\mu(3\lambda + 2\mu)}{(\lambda + \mu)} \tag{3.40}$$

$$\begin{aligned} C_2 = [(8l + 4m)(3\lambda^3 n + 50\lambda\mu^3 + 30\lambda^3\mu + \ 4l\mu^3 \ + 8m\mu^3 + 12\mu^4 \\ +68\lambda^2\mu^2 + 24\lambda m\mu^2 + 18\lambda^2 m\mu + 3\lambda^2 n\mu)]/[16(\lambda + \mu)^3 \times (2l + m)]. \end{aligned} \tag{3.41}$$

Let us now analyze the obtained coefficients and compare them to the coefficients of equation (3.3). Note that it is consistent to have $C_0 = 0$ because it implies a null deformation if the applied stress is null. Note also that the coefficient C_1 corresponds to the Young's modulus in the undeformed state E_0, such as it occurs in equation (3.3). This is a consistent result, which can be assessed by observing that if we take $l = m = n = 0$, the equation (3.41) becomes the Hooke's Law shown in equation (2.1). Finally, by comparing C_2 with equation (3.3) we obtain

$$C_2 = E_0\beta_E.$$

Thus, by dividing C_2 by C_1 (which is equal to E_0) we obtain the expression of the nonlinear parameter β_E as a function of the second order elastic constants λ and μ, and of the third order Murnaghan elastic constants l, m, and n

$$\beta_E = [(3\lambda^3 n + 50\lambda\mu^3 + 30\lambda^3\mu + 4l\mu^3 + 8m\mu^3 + 12\mu^4 + 68\lambda^2\mu^2 +$$
$$24\lambda m\mu^2 + 18\lambda^2 m\mu + 3\lambda^2 n\mu]/[4\mu(\lambda + \mu)^2(3\lambda + 2\mu)]. \tag{3.42}$$

The expression of β_E given by equation (3.42) takes a simpler form if it is expressed as a function of the elastic engineering constants in the undeformed state (Young's modulus E_0 and Poisson's ratio ν_0)

$$\beta_E \ E_0 = 2 \ m - l \ (-1 + 2 \ \nu_0)^3 + E_0 \left(\frac{3}{2} + 2\nu_0\right) + \nu_0{}^2 \ [3 \ n - 2 \ m \ (3 + 2\nu_0)] \tag{3.43}$$

3.3.2. Derivation of β_G

To derive the relationship between the nonlinear parameter β_G and the Murnaghan third order elastic constants l, m, and n, let us take the analogous steps as during the derivation of β_E, with some exceptions. The most important difference is the fact that β_G is associated to the dependency of the shear modulus G with respect to the prism's deformation due to the applied load. For that reason, we need to consider two deformation fields, the deformation due to the uniaxial stress and the field of small strains due to the torsion.

First, let us impose the deformation field compatible with the uniaxial stress (usually applied quasistatically in a loading test). This deformation can be described from the stretch values a and b. The boundary conditions are the same as during the derivation of β_E, so that a and b have again the same relationship given by equation (3.33).

At this point, the deformation $\chi^{(1)}$ is defined as

$$\chi^{(1)} = \begin{bmatrix} x_1^{(1)} \\ x_2^{(1)} \\ x_3^{(1)} \end{bmatrix} = \begin{bmatrix} aX_1 \\ bX_2 \\ bX_3 \end{bmatrix} \tag{3.44}$$

where the superindex (1) implies that the coordinates are referred to the intermediate state of deformation, before the application of the torsional field.

To apply now the torsional deformation field, let us first define the parameter Θ as the twist-per-unit-length, which we assume to be constant along the entire length of the bar (in direction 1). This hypothesis implies that each

section rotates proportionally to its position along axis 1, and its angle of twist is

$$\theta(x_1^{(1)}) = \Theta x_1^{(1)}, \tag{3.45}$$

Once the definition of Θ is known, the deformation of the prism after applying the torsional deformation becomes

$$\chi = \begin{bmatrix} x_1 \\ x_2 \\ x_3 \end{bmatrix} = \begin{bmatrix} x_1^{(1)} \\ \cos(\Theta x_1^{(1)})x_2^{(1)} - \sin(\Theta x_1^{(1)})x_3^{(1)} \\ \cos(\Theta x_1^{(1)})x_3^{(1)} + \sin(\Theta x_1^{(1)})x_2^{(1)} \end{bmatrix}. \tag{3.46}$$

To express the deformation as a function of the coordinates in the undeformed configuration, let us substitute equation (3.44) into (3.46), to obtain

$$\chi = \begin{bmatrix} x_1 \\ x_2 \\ x_3 \end{bmatrix} = \begin{bmatrix} aX_1 \\ \cos(\Theta aX_1)bX_2 - \sin(\Theta aX_1)bX_3 \\ \cos(\Theta aX_1)bX_3 + \sin(\Theta aX_1)bX_2 \end{bmatrix}. \tag{3.47}$$

It is necessary to clarify that the proposed torsional deformation field consists of a field in which the prism's cross-sections rotate but remain in the same plane. This hypothesis is exact for bars with circular cross-section, so the theory of Saint-Venant torsion fully describes those problems. In bars with non circular cross-sections it is necessary to consider the effect of warping to improve precision. However, as previously demonstrated in section 3.2 (and numerically verified in section 3.4), warping effects for solid-sections elongated prisms are so small that the considered hypotheses do not disturb significantly the derivation of β_G. Thus, Saint-Venant torsion theory is sufficiently precise in this case.

Once the deformation vector χ is known, we can calculate the tensors $\mathbb{F}, \mathbb{C}, \mathbb{E}, \mathbb{S}$ and σ_m following their definitions and procedure analogous as during the derivation of β_E. Thus,

$$\mathbb{F} = \nabla_m \chi,$$

$$\mathbb{C} = \mathbb{F}^T \mathbb{F},$$

49

$$\mathbb{E} = \frac{1}{2}\left(\mathbb{C} - \mathbb{I}\right),$$

$$\mathbb{S}_{ij} = \frac{\partial \psi}{\partial \mathbb{E}_{ij}},$$

$$\sigma_m = \mathbb{F}J_{\mathbb{F}}^{-1}\mathbb{S}\mathbb{F}^T.$$

Let us expand the expression of $\sigma_{m,12}$ which corresponds to the shear stress due to the torsional field. This stress is sufficiently small so that its relationship with Θ can be considered linear. Therefore, let us consider the expression of $\sigma_{m,12}$ which is an expression that depends on the five elastic constants and also of the stretch a and Θ. Thus, we are considering that the relationship between $\sigma_{m,12}$ and Θ is equivalent to the Saint-Venant torsion theory, where the shear stress is proportional to the twist-per-unit-length Θ, so that

$$\sigma_{m,12} = G_\varepsilon \Theta(X_3), \tag{3.48}$$

where G_ε is the instantaneous shear modulus, affected by the uniaxial deformation. In that expression, let us use equation (3.38) to substitute a for $\varepsilon_{11}+1$, to express G_ε as a function of the engineering strain ε_{11}. By applying a Taylor approximation at $\varepsilon_{11} = 0$, the expression becomes

$$G_\varepsilon = D_0 + D_1 \varepsilon_{11} \tag{3.49}$$

where D_0 and D_1 are coefficients that depend on the five elastic constants. Carrying out the math and expressing the results as a function of the Young's modulus E_0 and the Poisson's ratio ν_0 we get

$$D_0 = G_0,$$

$$D_1 = \beta_G G_0 = G_0(3 + \nu_0) + \frac{m(2 - 4\nu_0) + n\nu_0}{2}, \tag{3.50}$$

thus, the nonlinear parameter β_G is given by

$$\beta_G = 3 + \nu_0 + \frac{m(2 - 4\nu_0) + n\nu_0}{2G_0}, \tag{3.51}$$

3.4. Numerical validation of β_E and β_G

The objective of this section is to validate the relationships of β_E and β_G with respect to the third order elastic constants l, m, and n; or in other words, to validate equations (3.43) and (3.51). To this end, a series of finite element method (FEM) models have been built using COMSOL Multiphysics. Moreover, these series of models were employed to verify the conclusions drawn at section 3.2 and in Chapters 4 and 5, where the the warping effect and geometric nonlinearity effect have been neglected with respect to the acoustoelastic effect of the Saint-Venant term.

3.4.1. FEM model geometric and material description

Three models were built. All three involved prismatic solids of uniform square cross-section $L_2 \times L_3$ with $L_2 = L_3 = 0.15$ m. They had the same material properties, as indicated in Table 3.1, and their only input difference was their length L_1; these were 0.60 m, 1.20 m and 2.40 m, for models 1, 2 and 3, respectively. The selected material properties were those considered by Payan et al. [17] for their concrete specimen.

Table 3.1: General material and geometric properties of the FEM model.

E_0 (GPa)	42.39
ν_0	0.21
G_0 (GPa)	17.5
ρ (kg/m^3)	2386
l (GPa)	-3007
m (GPa)	-2283
n (GPa)	-1813
L_2 (m)	0.15

All three FEM models were formed by meshing the solid into tetrahedral elements (COMSOL's automatic meshing). The number of elements and their size varied depending on the model. The effect of the mesh on the results was considered by refining the mesh until the processed results of β_G and β_E did not change more than 1 % in two successive refinements trials of the same virtual experiment. Figure 3.5 shows the considered model's geometry for the case of model 1 ($L_1 = 0.60$ m). This model contained 23357 tetrahedral elements of an average volume of 0.58 cm^3.
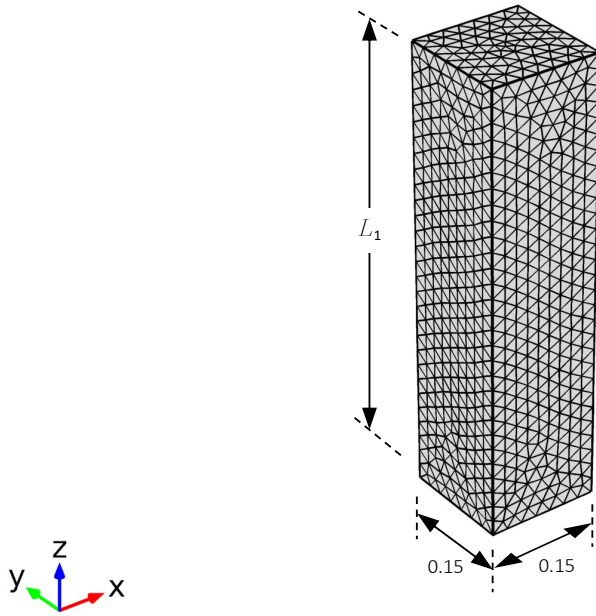
Figure 3.5: Geometry of model 1 ($L_1 = 0.60$ m) showing dimensions and tetrahedral mesh, units in meters.

3.4.2. FEM model virtual testing

The FEM model consisted of carrying out a virtual test, which was basically a simulation an actual experimental test as in Chapter 4. Thus, the virtual test consisted of carrying out a loading test in which the prism was submitted to compression loads. This was done by assigning the applied compressive stress onto the prism's end faces and sweeping the value of the compressive stress from 0 to 6 MPa in steps of 1 MPa; thus, seven loading cases were carried out for each of the models 1, 2 and 3. At each loading case, two "step studies" were performed.

First, the "stationary" step study was carried out in order to obtain the deformed solid associated to the applied load level. In this study, the geometric nonlinearity was enabled, and the boundary conditions were set accordingly to represent the same case as in section 3.3 (where the expressions of β_G and β_E where derived), i.e. no lateral displacement restrictions. The resulting

uniaxial strain was "measured". Then, using the solution of the stationary step study (i.e. the deformed solid) an "eigenfrequency" study was applied to obtain the fundamental torsional and the fundamental longitudinal frequencies of vibration

Thus, for each model, the virtual test yielded uniaxial strain values (ε) and frequencies of vibration (fundamental torsional f_1 and fundamental longitudinal $f_{L,1}$). We can then use torsional frequency vs. strain data to find the best fit β_G parameter using equation (3.13); and also use the fundamental longitudinal frequency vs. strain data to find the best fit β_E parameter using equation (3.15). Figure 3.6 shows the fundamental mode shapes of vibration for the longitudinal and torsional modes.
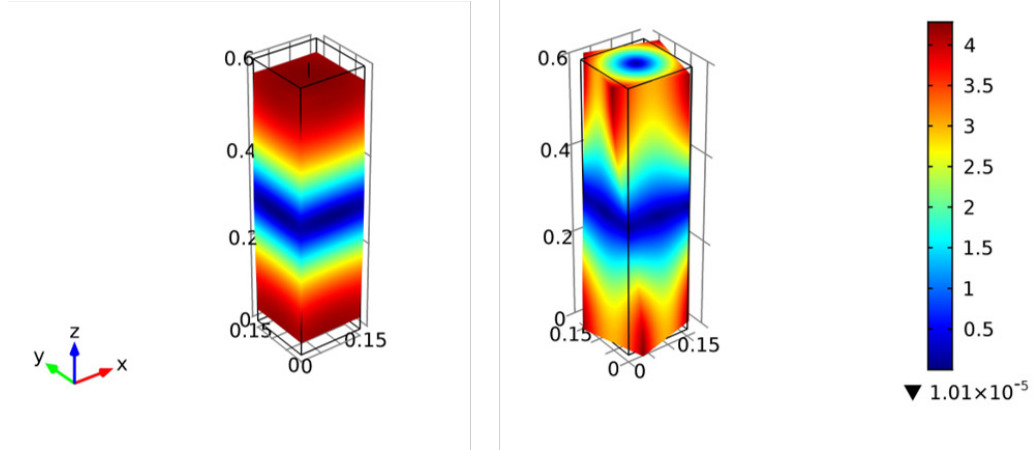
Figure 3.6: Fundamental longitudinal (on the left) and torsional (on the right) modal shapes of vibration obtained for model 1 ($L_1 = 0.60$ m) where the dynamic (vibrational) displacement field is shown in codes of color, in arbitrary units.

3.4.3. Analytical and numerical comparison of β_E and β_G

The analytical values of β_E and β_G obtained by introducing the material data of Table 3.1 into equations (3.43) and (3.51), respectively, are

$$\beta_E = -109.0$$

and

$$\beta_G = -83.3.$$

53

Figure 3.7 shows the frequency increments obtained for model 2 with $L_1 = 1.20$ m, but the increments do not differ among models. The graphs presented in Figure 3.7 show that the longitudinal frequency is more sensitive to load than the torsional frequency. The values of β_E and β_G obtained numerically are presented in Table 3.2, including the relative differences of these results with respect to the analytical results.
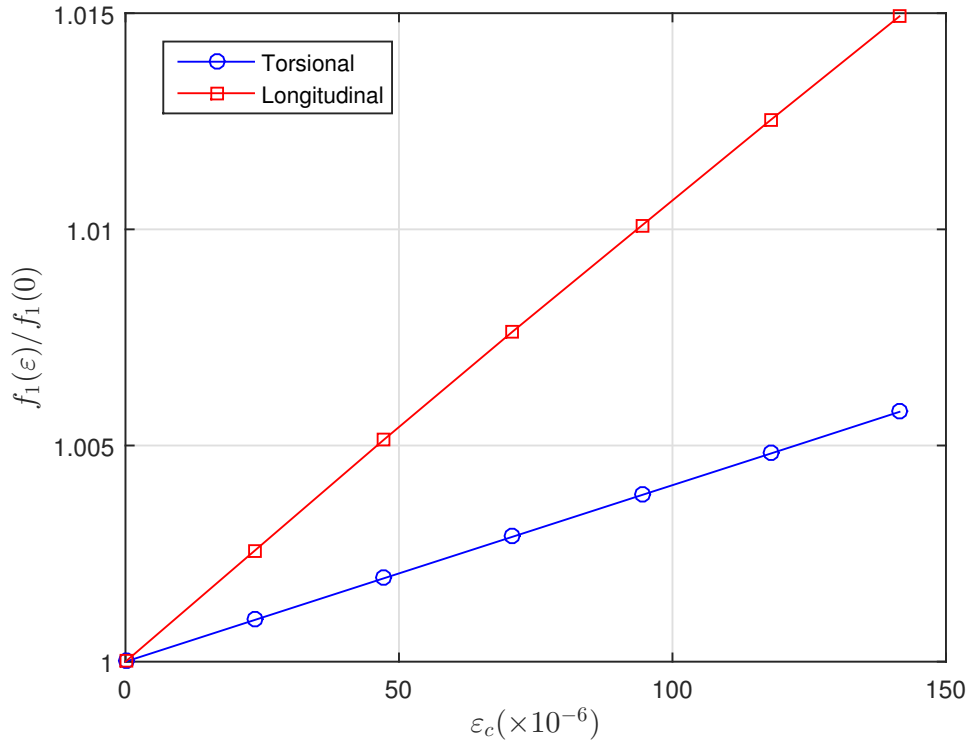
Figure 3.7: Results of frequency increments of model 2 ($L_1 = 1.20$ m) of the torsional mode, with $f_1(0) = 1038.3$ Hz, and of the longitudinal mode, with $f_{L,1}(0) = 1755.2$ Hz, with respect to compressive strains $\varepsilon_c(= -\varepsilon)$.

Table 3.2: Numerical results of β_E and β_G for the three FEM models (different L_1), including their relative differences with respect to the analytical values.

L_1 (m)	β_E	β_G	dif. β_E (%)	dif. β_G (%)
0.6	-107.0	-83.3	-1.9	0.0
1.2	-108.0	-83.3	-0.9	0.0
2.4	-108.0	-82.9	-1.0	-0.4

From the results presented in Table 3.2 it can be observed that there are minimal differences between the numerical and analytical values of β_E and

β_G. Only model 1, with L_1=0.60 m showed a relative difference of β_E larger than 1 %. This minimal differences could be due to the addition of several error sources, such as neglecting the geometric nonlinearity, the application of a Taylor expansion of second order during the derivation of β_E, and numerical deviations. Finally, it becomes clear from observing the three β_G results in Table 3.2, that neglecting the effects of warping and geometric nonlinearity during the derivation of β_G in section 3.3 was a valid assumption. This fact is depicted in Figure 3.8 where the frequency increments of the three models have been plotted; there it can be seen that the three curves overlap.
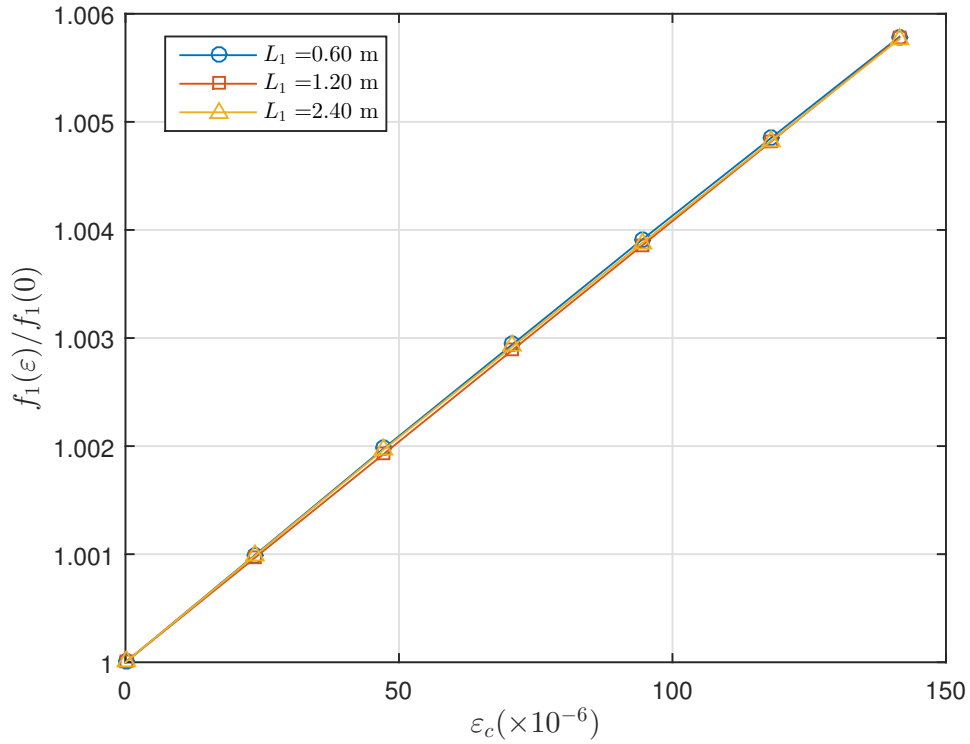
Figure 3.8: Results of fundamental torsional frequency increments of models 1, 2 and 3, (L_1 =0.60 m, L_1 =1.20 m, and L_1 =2.40 m, respectively) with respect to compressive strains $\varepsilon_c(= -\varepsilon)$.

3.5.   Relationship between wave speed and β_G

To obtain β_G from wave propagation techniques, one could measure three different wave modes during a loading test, for example S-wave speed V_{21}, S-wave speed V_{23} and P-wave speed V_{22}, then use Hughes and Kelly's equations

(2.37), (2.38) and (2.39), to calculate l, m, and n, and then use equation (3.51) to calculate β_G. This is an inverse problem where the physical properties l, m, and n, need to be found from the experimental observations V_{21}, V_{23} and V_{22}. However, when the math is carried out, it occurs that the S-wave speed V_{21} observation becomes dependent on m and n (and not of l) with a relationship which corresponds exactly to the definition of β_G given by the equation (3.51). This fact enables computing β_G directly from observations of one wave mode only, V_{21}, instead of three wave modes. This section presents the analysis of the relationship between these two magnitudes.

The dependence between the velocity of wave propagation in solids and the applied uniaxial stress has been presented in equations (2.35) through (2.39). The factors that multiply the stress σ in those equations, are responsible for the wave speed stress-dependence. These factors have been named "acoustoelastic factors", and have been defined in numerous forms. The acoustoelastic factors are naturally a function of the second and third order elastic constants. Here, let us deepen into the wave mode propagating in direction 2 with a wave polarization in direction 1. It should be noted that the election of wave modes traveling in direction 2 (or 3), which are transverse directions, are experimentally more convenient than those traveling in direction 1, in the longitudinal direction, because specimens such as beams or columns are accessible to their lateral faces but no to their end faces, easing attaching transducers and cabling. Furthermore, within the three possible modes traveling in direction 2 (V_{21}, V_{22} and V_{23}), the one polarized in direction 1, V_{21}, is the most sensitivity to uniaxial stress in concrete specimens [17, 64].

Let us rewrite equation (2.39):

$$\rho V_{21}^2 = \rho V_{31}^2 = \mu + \frac{\sigma}{3K}\left[m + \frac{\lambda n}{4\mu} + \lambda + 2\mu\right],$$

where all the elastic parameters and density ρ are by definition stress-independent, $K = \lambda + \frac{2}{3}\mu$ and $\mu = G_0$.

Now, let us observe that any of the equations (2.35) through (2.39) can be expressed as a linear relationship between the square of the velocity V vs. the applied stress σ which, by carrying out a Taylor series expansion, take the form

$$\rho V^2(\sigma) = \rho V_0^2 + 2\rho V_0 \frac{\Delta V}{\Delta \sigma}\sigma, \tag{3.52}$$

where V_0 is the wave speed in the undeformed solid. In equation (3.52), the term $\Delta V/\Delta \sigma$ is the slope of the stress-dependent velocity and the applied stress. Traditionally, this slope has been named the acoustoelastic coefficient because of the early approaches for stress determination using wave propagation phenomena. In this case, because we are considering the wave-mode 21, let us define the acoustoelastic coefficient A_{21} as the slope

$$A_{21} = \frac{\Delta V}{\Delta \sigma}. \tag{3.53}$$

Let us compare equations (2.39) and (3.52) term to term, thus

$$\frac{m + \frac{\lambda n}{4G_0} + \lambda + 2G_0}{3(\lambda + \frac{2}{3}G_0)} = 2\rho V_{21,0}.A_{21}, \tag{3.54}$$

where the subindex 21 of $V_{21,0}$, specifies that the wave speed corresponds to that mode. Let us rewrite equation (3.51),

$$\beta_G = 3 + \nu_0 + \frac{m(2 - 4\nu_0) + n\nu_0}{2G_0},$$

isolate m from it, and substitute it into (3.54), and express the Lamé constants λ and μ in terms of the engineering constants E_0 and ν_0, to obtain

$$\beta_G = 1 + 3\nu_0 + 2\sqrt{2E_0\rho(\nu_0 + 1)}A_{21}. \tag{3.55}$$

Now, let us express ν_0 in terms of E_0 and $V_{21,0}$, to obtain

$$\beta_G = 1 + 3\nu_0 + \frac{2E_0}{V_{21,0}}A_{21}. \tag{3.56}$$

Note in equation (3.56) that β_G could be estimated directly by measuring A_{21}, which depends only on V_{21} and the applied stress σ. This is an interesting result because it reduces the experimental complexity given that only one wave-mode is necessary, thus, only one pair of transducers would be needed. This equation enables comparing the results of β_G obtained from two different techniques, the one developed in this Thesis, based on torsional vibration, and the one based in wave propagation.

Finally, let us observe in (3.56), that the factor $A_{21}/V_{21,0}$ is actually the slope of the wave-speed increment ($V_{21}/V_{21,0}$) vs. stress (σ). Thus, let us define this slope $\overline{A_{21}}$ as

$$\overline{A_{21}} = \frac{A_{21}}{V_{21,0}} = \frac{\Delta \frac{V_{21}}{V_{21,0}}}{\Delta \sigma}. \tag{3.57}$$

Thus, by substituting this definition into equation (3.56) we obtain

$$\beta_G = 1 + 3\nu_0 + 2E_0\overline{A_{21}}, \tag{3.58}$$

which means that only by measuring the increment of the wave speed V_{21} (and not necessarily its value) during a test in at least two different levels of stress, it is possible to estimate β_G, provided that E_0 and ν_0 are known or measured. This is an important observation because it enables the application of other testing techniques, such as coda wave interferometry [17] which relies in measuring the relative wave speed variation but cannot measure the actual value of wave speed. Moreover, by considering from the literature that $\overline{A_{21}} \cong$ 0.15 % per MPa [17, 56] and using that value to inspect equation (3.58), we see that the term $2E_0\overline{A_{21}}$ should take values around -150, so the term $3 \times \nu_0$ (which for concrete takes values between 3×0.15 to 3×0.24) could be neglected or roughly estimated without incurring much error on β_G.

3.6. Theoretical analysis of the stress estimation of columns from vibration acoustoelastic tests

3.6.1. Computation of the existing strain ε_1

This section poses a theoretical description of an experiment prepared to estimate current strains (or stresses) on an elongated structural member.

Let us consider an elongated prism, for example a concrete column of square cross-section, which is being submitted to an applied uniaxial stress σ_1 and it is therefore strained with ε_1. Here the subindex 1 refers to the state of stress-strain "1". From equation (3.13) we know the relationship of the fundamental torsional frequency of vibration of the specimen under stress, f_1 (also associated to state 1 of stress-strain), and the fundamental torsional frequency of vibration of the unstressed (undeformed) element, f_0, the nonlinear material parameter β_G and the applied uniaxial strain ε_1, which we rewrite as

$$f_1^2 = f_0^2 \left(1 + \beta_G \varepsilon_1\right) \tag{3.59}$$

Note that for this analysis we have changed the nomenclature, in which, the previous meaning of the subindex "1" implied $n = 1$, meaning the first or fundamental frequency of vibration. This nomenclature has been dropped now. For this analysis, let us only refer to the fundamental frequency of vibration, and let us relate the subindices 0, 1, 2, 3, ... to different levels of strain (and stress), 0, ε_1, , ε_2, ε_3,... respectively (or 0, σ_1, , σ_2, σ_3, ... respectively).

Also, let us now assume that we have already characterized the concrete material, and thus, we know the value of β_G. However, we do not know the fundamental frequency of vibration in the undeformed state, f_0, and we want to carry out a test to estimate the current strain ε_1.

At the current loading state, state 1, we can measure the torsional frequency f_1. We can then load (or unload) the column, to reach another loading state, state 2, and while doing that we can measure the change of strains $\Delta\varepsilon_{21}$, and in the new state we can also measure the new frequency of vibration f_2, which also behaves following

$$f_2^2 = f_0^2 \left(1 + \beta_G \varepsilon_2\right). \tag{3.60}$$

Thus, by subtracting equation (3.59) from (3.60) we get

$$f_2^2 - f_1^2 = f_0^2 \left(1 + \beta_G \varepsilon_2\right) - f_0^2 \left(1 + \beta_G \varepsilon_1\right) = f_0^2 \beta_G \Delta\varepsilon_{21} \Rightarrow$$

$$\frac{f_2^2 - f_1^2}{f_1^2} = \frac{\beta_G \Delta\varepsilon_{21}}{1 + \beta_G \varepsilon_1}. \tag{3.61}$$

We can isolate ε_1 from equation (3.61) which yields

$$\varepsilon_1 = -\frac{1}{\beta_G} + \frac{\Delta\varepsilon_{21}}{\frac{f_2^2 - f_1^2}{f_1^2}}. \tag{3.62}$$

However, because the value of ε_1 is very sensitive to small changes of measured frequencies, it is better to carry out tests at a series of loading i states, where i goes from 1 through N. In each i loading state, we measure $\Delta\varepsilon_{i1}$ and f_i. Thus, we can apply equation (3.61) to every i state, so that we have

$$\frac{f_i^2 - f_1^2}{f_1^2} = \frac{\beta_G \Delta\varepsilon_{i1}}{1 + \beta_G\varepsilon_1}. \tag{3.63}$$

From these test results, the slope of the line that fits the data to equation (3.63) corresponds to $\beta_G/(1 + \beta_G\varepsilon_1)$, from which ε_1 can be calculated. This reasoning is depicted in Figure 3.9 with created data.
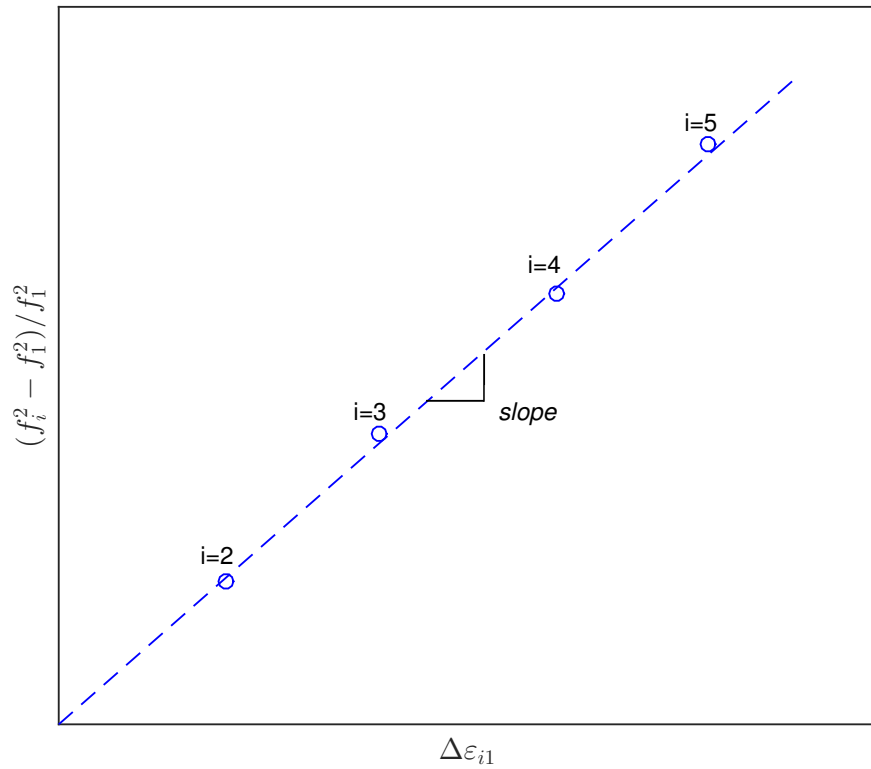
Figure 3.9: Created data of "measured" values of frequency increments $(f_i^2 - f_1^2)/f_1^2$ with respect to $\Delta\varepsilon_{i1}$ in order to depict the extraction of ε_1.

By carrying out an experiment with the explained characteristics, one can calculate ε_1 using

$$slope = \frac{\beta_G}{1 + \beta_G\varepsilon_1} \Rightarrow$$

$$\varepsilon_1 = \frac{1}{slope} - \frac{1}{\beta_G}. \tag{3.64}$$

3.6.2. Monte Carlo analysis to study error of ε_1

It is useful to calculate the expected error of ε_1 and σ_1 from typically known experimental uncertainties of the involved parameters. To obtain the expected error, a Monte Carlo analysis was carried out by simulating the experiment 5000 times in MatLab and taking the standard deviation of the relative difference between the "virtual-experimental" ε_1 and the assumed value ("exact"). To start the analysis, the "exact" values of the involved parameters were selected and calculated. These are presented in Table 3.3.

Table 3.3: Material and geometric exact theoretical properties considered for the Monte Carlo analysis.

E_0 (GPa)	30
ν_0	0.2
ρ (kg/m^3)	2400
β_E	-156
β_G	-120
L_1 (m)	0.6
L_2 (m)	0.15
L_3 (m)	0.15
ε_1 ($\times 10^{-6}$)	-100
σ_1 (MPa)	-3.046

Note that ε_1 and σ_1 are parameters that the virtual experiment expects to calculate. The virtual experiment consisted in carrying out $N = 20$ loading states, starting from state 1, with applied strain ε_1 and sequentially increasing the applied strain at every i state in steps of $\Delta\varepsilon_{i1}$. The presented formulation allows calculation of all the involved parameters. In particular, during the virtual experiment, at each step we measure $(\Delta\varepsilon_{i1})_{exp}$, $(f_i)_{exp}$, and we have previously characterized our concrete and measured $(\beta_G)_{exp}$. The subindex "exp" stands for experimental measurement, which implies that they have an inherent uncertainty. Here, these uncertainties are modeled by considering that they behave following a Normal distribution with zero mean and a certain standard deviation, presented in Table 3.4.

Thus, after running the virtual experiment once we obtain N measurements of frequencies of vibration $(f_i)_{exp}$ (one for each i step) and $N-1$ measurements of strain increments $(\Delta\varepsilon_{i1})_{exp}$, obtaining virtual-experimental results as depicted in Figure 3.9. By applying equations (3.63) and (3.64), it is possible to find the virtual-experimental result of initial strain $(\varepsilon_1)_{exp}$. Because $(\varepsilon_1)_{exp}$

Table 3.4: Uncertainties of the "experimental" measurements considered for the Monte Carlo analysis.

	Standard deviation
$(\beta_G)_{exp}$	0.1
$(\Delta\varepsilon_{i1})_{exp}$	0.1×10^{-6}
$(f_i)_{exp}$	0.1 Hz

was found from "uncertain" parameters, $(\varepsilon_1)_{exp}$ will differ from the "exact" value ε_1. This difference is assessed by considering their relative difference (error) calculated as

$$\text{Error}(\varepsilon_1) = \frac{(\varepsilon_1)_{exp} - \varepsilon_1}{\varepsilon_1}. \tag{3.65}$$

Due to the randomness of the errors of the involved parameters ($(f_i)_{exp}$, $(\Delta\varepsilon_{i1})_{exp}$ and $(\beta_G)_{exp}$), the obtained $\text{Error}(\varepsilon_1)$ also varies if the experiment is run several times. Thus, we can know which would be the range of most probably values of $\text{Error}(\varepsilon_1)$ by building its distribution. Here the distribution of $\text{Error}(\varepsilon_1)$ was built by running the virtual experiment a large number of times, in this case 5000 times, and computing the $\text{Error}(\varepsilon_1)$ for each run. These data are presented in the histogram shown in Figure 3.10.

The standard deviation of the distribution of $\text{Error}(\varepsilon_1)$ was found to be 10 %, meaning that approximately 68 % of the obtained values of $(\varepsilon_1)_{exp}$ differ from the actual value ε_1 less than 10 %. A similar conclusion can be drawn for the expected error of σ_1 if E_0 and β_E have been well characterized. A 10 % error standard deviation is a fair result for such a challenging goal like this one (to estimate the actual stress of a column from fully nondestructive testing).

It should be noted that this virtual experiment depends on many variables which may substantially affect the obtained distribution of $\text{Error}(\varepsilon_1)$, and thus, they may increase or decrease the error standard deviation. For instance, improving or reducing the accuracy of the measurements obviously tends to affect the experimental accuracy likewise (improving the experimental accuracy means reducing the error standard deviation). If one cannot have access to equipment with enough accuracy, increasing the number of measurements (N) would also improve the experimental accuracy. Selecting additional modes of vibration from which to assess nonlinearity could also improve the accuracy, but this is out of the scope of this thesis. Also, having a material with higher nonlinearity (higher values of β_G) improves the experimental accuracy and the
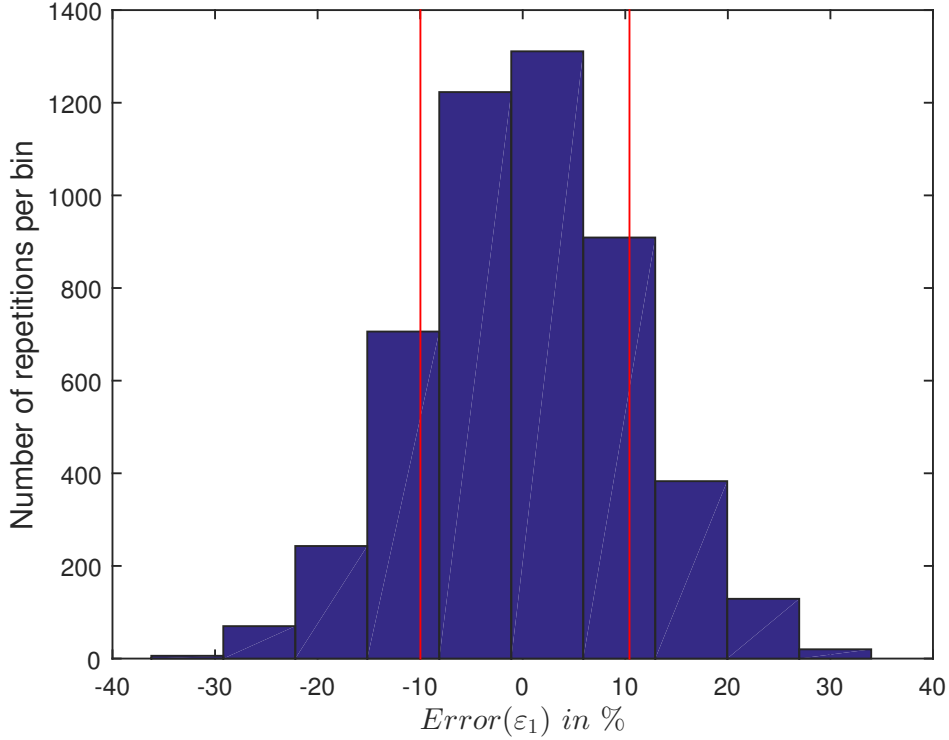
Figure 3.10: Histogram showing the distribution of Error(ε_1) in % from a Monte Carlo analysis involving 5000 runs. Red lines indicate one standard deviation away from zero.

opposite happens for lower material nonlinearity.

3.7. Conclusions

Based on the analytical and numerical developments presented in this chapter, the following conclusions can be drawn.

- Material nonlinear parameters β_E and β_G were defined based on 1D constitutive equations of elongated prisms. These are associated to the rate of change of the strain dependent Young's modulus E_ε, and the strain-dependent shear modulus G_ε, respectively. These nonlinear material parameters are capable of modeling the acoustoelastic effect, i.e. the frequency of vibration increments observed when elongated prisms are uniaxially compressed.

- In general terms, in order to use torsional vibration for acoustoelastic characterization, the effect of non-uniform torsion and geometric non-

linearity (P-δ effect) should be considered as they are coupled with the acoustoelastic effect. However, they can be neglected for any specimen with solid cross-section that exhibits an aspect-ratio L_2/L_1 lower than 2, which corresponds to essentially all typical beam-type concrete elements with solid sections. In these cases, the Saint-Venant torsion term dominates, so the problem can be successfully modeled using the strain-dependent shear modulus G_ε. This fact was verified using an FEM model in COMSOL.

- Boundary conditions affect the frequencies of vibration of the element. Ideally, boundary conditions should not be affected by the applied external load. However, if they do, their effect must be somehow characterized and decoupled from the results in order to characterize material nonlinear parameters. For the case of torsional vibration for acoustoelastic characterization, the existence of imperfect boundary conditions (springs of constant k instead of free ends or fixed ends) shifts the fundamental frequency of vibration and creates a "nearly rigid" low frequency mode; these two modes can be used to back-calculate the concerning magnitudes k and G.

- The problem of a nonlinear elongated prism under quasistatic compression was studied using the Theory of Finite Elasticity, and the expressions of β_G and β_E were analytically calculated in terms of the third order elastic constants l, m and n. These expressions were successfully verified numerically using an FEM model in COMSOL.

- It was shown that monitoring the variation of the wave speed mode 21 (V_{21}) with respect to stress is sufficient to calculate β_G. This provides a method to compare the use of a torsional technique for acoustoelastic characterization (or stress determination) to the traditional acoustoelastic techniques based on wave propagation.

- A virtual test was run using MATLAB, involving a column of known properties and unknown applied quasistatic uniaxial stress (and strain). Measurements were simulated by considering given uncertainties, and equations were applied to calculate the "current applied strain". A Monte Carlo analysis showed that the "estimated" (calculated) current applied strain is very sensitive to the rest of the involved material properties and measurements; however, under certain conditions (accurate measurements and sufficient nonlinearity), it is possible to obtain ac-

ceptable estimation of the unknown applied stress (and strain).

Chapter 4

Development of an experimental technique based on torsional vibration for the acoustoelastic characterization of concrete

4.1. Introduction

Disclaimer: Most of the content in this chapter has been published in: A. Spalvier, L.D. Domenech, G. Cetrangolo, J.S. Popovics, "Torsional vibration technique for the acoustoelastic characterization of concrete, Materials and Structures, 53:7, 2020, https://doi.org/10.1617/s11527-020-1438-6.

The objective of this chapter is to provide a robust experimental description of the use of the torsional resonance technique for the acoustoelastic (nonlinear) characterization of concrete, based on the theory detailed in Chapters 2 and 3. The observed nonlinear stiffening behavior of concrete in one dimension was modeled using a nonlinear parameter β_G, which corresponds to the rate of change of the dynamic shear modulus G with respect to the uniaxial compressive strain ε. The experimental results fit well the theoretical description given in Chapter 3, demonstrating and quantifying the acoustoelastic behavior of concrete samples. The analyses posed in this chapter document the experimental procedure to characterize the relationship between torsional frequency of vibration and compressive uniaxial loading. This approach provides a pathway for nondestructive estimation of in situ compressive stress in concrete

structural members.

4.2. Materials and methods

4.2.1. Specimens

The experimental campaign comprised two types of specimens: prismatic specimens of nominal dimensions $15 \times 15 \times 60$ cm³ and standard companion cylinders of dimensions 10 cm of diameter and 20 cm tall. Three concrete mixture designs were tested, A, B and C. The prismatic specimens were used in the acoustoelastic tests, i.e. to characterize concrete's acoustoelasticity by computing β_G, and the companion cylinders to find concrete's standard compressive strength. Three companion cylinders per mixture were tested to measure standard compressive strength. One prismatic specimen per mixture was used for the acoustoelastic tests; these specimens were named 1, 2, and 3, cast from mixtures A, B and C, respectively. Other two prismatic specimens, cast from mixture A, were employed to characterize the boundary condition stress-dependency (see subsection Studying changing boundary conditions, below) and to correct frequency measurements due to temperature changes (see subsection Controlling effect of temperature, below). Mixture B had a very low water-to-cement ratio (w/c), around 0.32, whereas A and C had w/c around 0.42. Mixtures A and B were composed of granitic chip coarse aggregate with 25 mm maximum aggregate size, while mixture C contained 50 % of the same coarse aggregate plus another 50 % of granitic chip coarse aggregate with 12 mm maximum aggregate size. These three mixtures reasonably represent the range of mixtures expected for precast concrete. The mixtures were provided by a precast concrete company, so the exact mixture designs and weight batches are proprietary. Table 1 contains the mixtures' compressive strengths, calculated from 3 cylinders per mixture, tested at day 28 after casting, following ASTM C39/C39M [25] and ASTM C192/C192M [82]. Table 4.2 contains the dynamic elastic constants characterization results for prisms 1, 2 and 3, measured following ASTM C215 [9] prior to carrying out the acoustoelastic tests.

Table 4.1: Mean and standard deviation values of compressive strength (f_c) for mixtures A, B and C, obtained from standard cylinders.

	Mean f_c (MPa)	Std. dev. (MPa)
A	30.7	1
B	47.9	1.6
C	29.6	2.8

Table 4.2: Properties of prism specimens 1, 2 and 3, carried out prior to acoustoelastic test loads.

Specimen Name	1	2	3
Concrete Mixture	A	B	C
ρ (kg/m^3)	2251.2	2386	2318.7
E_0 (GPa)	33.2	43.13	34.43
G_0 (GPa)	13.92	18.03	14.57
Poisson's ratio ν_0	0.192	0.196	0.182

4.2.2. Acoustoelastic test procedure

After characterizing the prisms, they were subjected to four loading/unloading cycles by applying compressive load steps of approximately 1 MPa between 0 and 6 MPa under load control. The applied load was kept constant at each load step for 5 minutes before the resonance tests were carried out.

Figure 4.1 shows the testing configuration. The load was applied onto the prism through end platens that reacted against a steel frame. Two 16 mm-thick neoprene pads were placed directly in contact to the concrete prism end faces in order reduce stress concentrations and to acoustically isolate the prism from the loading system. The longitudinal (axial) strains were measured using a pair of strain gauges (Tokyo TML model PL-90-11-1LJC) attached onto opposing faces of the prism.

The resonance tests were performed at each load step by applying five low-energy impacts with a steel-tipped hammer. Signals were acquired by conditioned accelerometers connected to a NI 9215 / NI cDAQ 9174 unit that was connected to a personal computer. In order to decouple the fundamental torsional mode from other modes of vibration, the specimen was impacted close to the bottom end, towards one corner, and the acceleration signals were
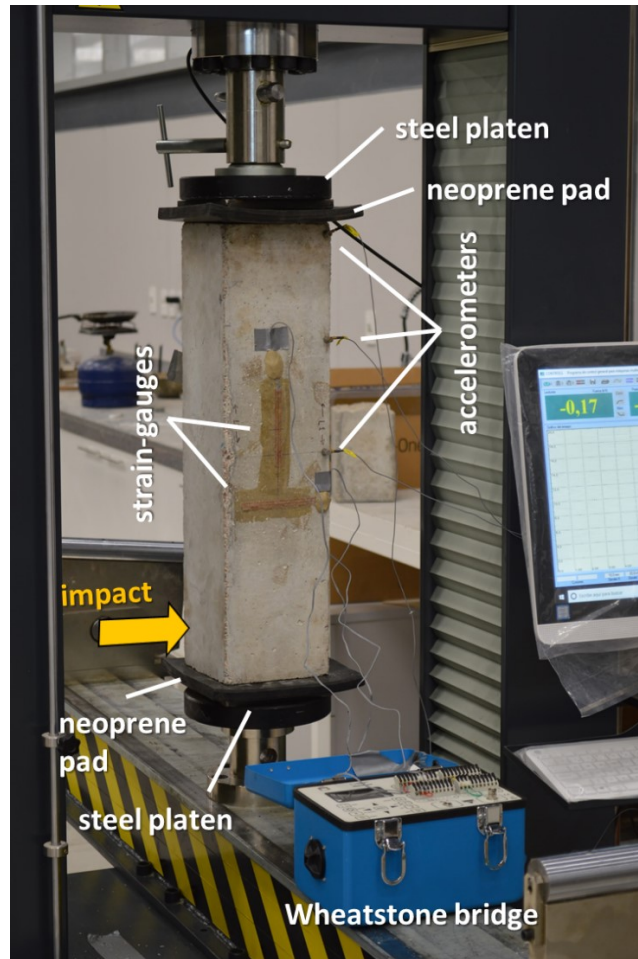
Figure 4.1: Experimental configuration for the acoustoelastic tests and scheme showing the geometric configuration of the accelerometers and the impact for vibration measurements.

measured on the upper side of the prism, perpendicular to the direction of impact, as depicted in Figure 4.1.

4.2.3.   Signal processing

The time-domain raw signals consisted of 25,000 points, acquired at a 100 kHz sampling rate. Each signal was processed using MATLAB platform (The MathWorks Inc.). A half-Tukey window (200 points long, 2000 μs) was applied to the first portion of the signal that affects approximately the first 4 periods of the vibration signal; this process reduced the transient effect of the impact and yielded more consistent results. The signals were then padded with 500,000 zeros at their tails. Then, the Fast Fourier Transform routine

was applied to obtain the amplitude spectrum of each signal. The five signals associated with each impact event were averaged in the frequency domain to obtain three (one per accelerometer) average amplitude spectra per load step. The frequencies of vibration were peak-picked from the amplitude spectra. The signals from all three accelerometers were used for peak-picking the frequency of vibration associated with "mode 0" (the nearly rigid mode of vibration), denoted as $\hat{\omega}_0$ in Chapter 3. The signal from the top-most accelerometer was used for peak-picking the frequency of vibration associated with "mode 1", which corresponds to the first "nearly fundamental" torsional mode, denoted as $\hat{\omega}_1$.

4.2.4. Studying changing boundary conditions

Equation (3.13) is the fundamental equation that governs the experiments. It relates the fundamental torsional frequency of vibration f_1 (corresponding to a free-free boundary condition) with the measured compressive strains ε. By carrying out a load test and measuring f_1 and ε we can extract β_G. However, the neoprene pads at the samples' ends restrain slightly their free end twist. Thus, it is not possible to directly measure f_1; rather, we can measure $\hat{f}_0$ ($=\hat{\omega}_0/2\pi$) and $\hat{f}_1$ ($=\hat{\omega}_1/2\pi$), as explained in the Changing boundary conditions section of Chapter 3.

The procedure to obtain f_1 involved characterizing the neoprene pad prior to carrying out the acoustoelastic tests. To this end, a preliminary test using another prism cast from concrete batch A (not specimen 1) was conducted. Three loading/unloading cycles were applied, and at each loading step measurements of $\hat{\omega}_0$ and $\hat{\omega}_1$ were taken; equation (3.17) was used to determine the corresponding spring constant k. Then an empirical relationship (without explicit physical meaning) between the computed k values and the measured stress σ values was established. For this purpose, let us propose an equation of the form

$$k(\sigma) = a_k \times \log_e\left(-b_k\sigma + c_k\right) + d_k, \tag{4.1}$$

where σ is the stress in MPa (where compression takes negative values), and a_k, b_k, c_k and d_k are the coefficients to be found by the regression analysis. Equation (4.1) was then used for the acoustoelastic tests of the three prisms 1, 2 and 3. Thus, in these tests, k was estimated by measuring the applied stress

σ and by applying equation (4.1) for each loading step. Then, by knowing k and by measuring $\hat{f}_1$, equation (3.17) is used to find $G_\varepsilon(\varepsilon)$. Then, ω_1 and f_1 are computed from equation (3.10).

4.2.5. Controlling effect of temperature

After calculating the free-free fundamental frequency of vibration at each load step, a correction was applied to account for the effects of material temperature. Because the experiments were carried out in a standard structural laboratory, temperature variations during a given test (one loading and unloading cycle) did not vary significantly. However, for tests carried out on different days, the temperature variations were more significant and likely affected the frequency results. The temperature correction was carried out by regularly measuring the free-free fundamental torsional frequency of vibration on an unloaded "control prism". This prism was cast from mixture A and was housed on the same room as prisms 1, 2 and 3. The measured free-free fundamental frequency of vibration f_1 of prisms 1, 2 and 3 was adjusted as indicated by the percentage change observed in the control prism. The obtained frequencies resulted in temperature-corrected boundary condition-corrected frequencies of vibration, which were finally used to compute β_G. Because temperature changes during each loading/unloading cycle were very minor, the slopes of frequency vs. strain were not measurably influenced. Therefore β_G results were not affected by temperature changes. This correction was carried out to allow comparison of frequency data among different loading/unloading cycles and specimens.

4.2.6. Summary of test procedure and calculations

Step 1: Using a concrete sample from batch A (not specimen 1), carry out an acoustoelastic test to measure the applied uniaxial stress σ and associated torsional frequencies $\hat{f}_0$ and $\hat{f}_1$ (or $\hat{\omega}_0$ and $\hat{\omega}_1$) in several loading/unloading steps. Use equation (3.17) to determine the corresponding spring constant k (pad's torsional stiffness). Fit equation (4.1) to the σ vs. k data by finding the coefficients a_k, b_k, c_k and d_k.

Step 2: Run the acoustoelastic test on the concrete samples by measuring the applied stress σ, strain ε and frequency $\hat{f}_1$ (or $\hat{\omega}_1$). Use equation (4.1), with the known a_k, b_k, c_k and d_k, to find k at each load step of known stress σ. For

each load step, introduce the measured $\hat{\omega}_1$ and calculated k into equation (3.17) and find $G_\varepsilon(\varepsilon)$. Then, calculate ω_1 and f_1 with equation (3.10). Simultaneously measure the fundamental torsional frequency of the control prism.

Step 3: Correct the obtained f_1 by using the fundamental torsional frequency measured on the control prism to account for temperature variations.

Step 4: Apply a linear regression to fit equation (3.13) using the corrected f_1 and the measured ε data. From the best fit coefficients of slope and Y-intercept, find β_G and $f_1(0)$.

4.3. Results and discussion

4.3.1. Signal results

Figure 4.2a shows a typical raw time-domain signal collected by the top-most accelerometer during a given load step of the acoustoelastic tests. Note it is a clean signal with an excellent SNR. Figure 4.2b shows the amplitude spectra of five signals collected during one load step. There, note that the spectra overlap, showing good consistency between independent impulse vibration measurements. This figure shows the frequency peaks associated to modes 0 and 1, from which $\hat{f}_0$ and $\hat{f}_1$ were identified, respectively.
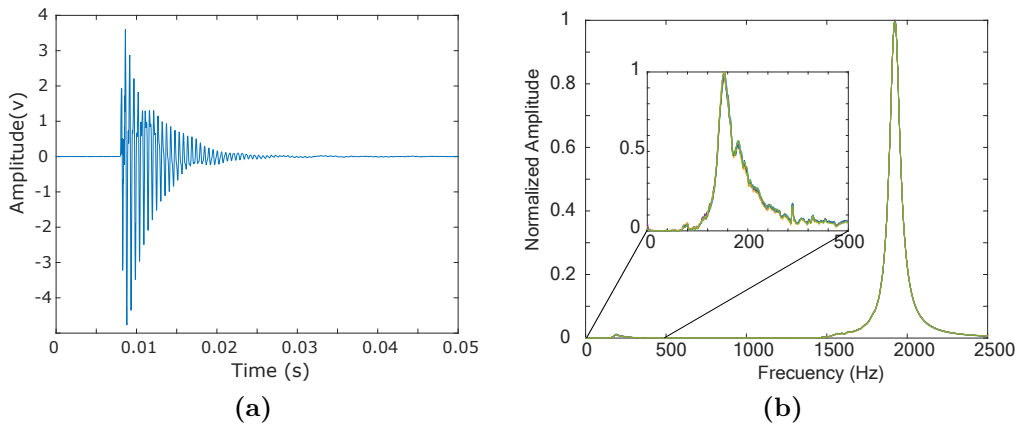
Figure 4.2: Example raw time domain signal acquired by the top-most accelerometer; (b) five overlapping amplitude spectra, normalized with respect to the maximum showing both nearly fundamental torsional mode (mode 1) at about 1900 Hz and the nearly rigid mode (mode 0) at about 180 Hz.

As seen in Figure 4.2b, most of the vibrational energy excites mode 1, vibrating around 1900 Hz and only a minor portion of the energy excites mode

0, around 180 Hz. This fact has to do with the characteristics of the impact event and sensing configuration. It should be noted that mode 0 corresponds to the "nearly rigid" mode discussed above. The measurement of mode 0 frequency is necessary to characterize the spring constant k, in order to decouple the effect of changing boundary conditions from the acoustoelastic effect.

4.3.2. Characterization of the boundary conditions

A preliminary prismatic sample cast from batch A was employed to characterize the torsional springs constants k with respect to the applied stress σ. Figure 4 shows the obtained results.
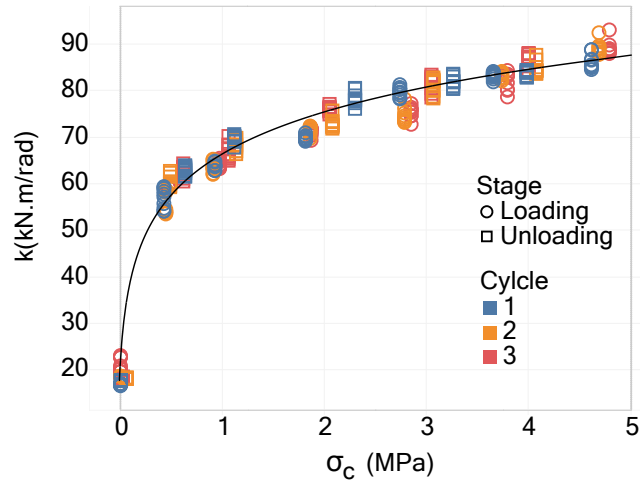
Figure 4.3: Value of k with respect to applied compressive stress σ_c $(= -\sigma)$ during loading and unloading cycles 1, 2 and 3 for preliminary prism cast from batch A. The continuous line is the best fit line using the function form shown in equation (4.1).

In Figure 4.3, the superimposed black curve represents a best fit to the data following equation (4.1), where $a_k = 14.01$ kN.m/rad, $b_k = 15.57$ MPa^{-1}, $c_k = 0.3458$ and $d_k = 31.91$ kN.m/rad, and σ is the applied stress in MPa where a negative value indicates compression. The regression to the data yielded a coefficient of determination R$^2 = 0.980$ demonstrating excellent fit. Note that the form of the equation used to fit the data is not good for stress values very close to zero because there is a pole at $\sigma \cong +0.03$ MPa caused by the log$_e$ fitting function. However, this does not imply a problem for the analysis because we focus on the structural/material behavior at compression stresses higher than 1 MPa, which correspond to those found in typical concrete structures. Thus,

the frequency results obtained at compression stresses lower than 1 MPa are not included in the following discussion. In Figure 4.3, values of k increase from 65 kN.m/rad at 1 MPa to 90 kN.m/rad at 5 MPa. This load-dependence of k affects the computation of β_G because the measured frequencies change due to both the acoustoelastic effect and the change of k. If the load dependence of k had not been considered, β_G would have been overestimated by 20-30 %. Note that other boundary conditions could imply greater or lesser influences; for example, a column under compression restrained by beams at both ends is likely to have a high k value that would probably be independent of applied compression.

4.3.3. Torsional frequency vs. uniaxial strain

Figure 4.4 presents the variation of fundamental torsional frequencies as a function of the uniaxial strains obtained during the loading and unloading cycles of prism 1 (for data acquired at compressions higher than 1 MPa). There is a clear positive correlation between frequency and compressive strain, where frequency increases as compressive strain increases. Cycles 3 and 4 are more similar to each other than the rest. This implies that the behavior tends to become more consistent as the sample is subjected to more loading/unloading cycles, as would occur in a real structural element. Similar results were found for prisms 2 and 3.

Note that the first loading cycle starts at frequency approximately 1890 Hz and after unloading it reaches frequency value close to 1885 Hz. This fact is not observed in the other three cycles as prominent as in cycle 1. This observation suggests that some mechanism involving softening, e.g. damage, may be occurring during loading cycle 1. It appears that stiffening (acoustoelastic) and softening (damage or other) effects compete each other, which reduces the slope (lower β_G value) of the first loading cycle with respect to the subsequent cycles. In cycle 1, the loading (blue) curve consistently stays above the unloading (orange) curve, while the opposite happens in cycle 2. The characteristic observed in cycle 2, where the unloading curve is above the loading curve, was also observed in the other prisms. We cannot explain this behavior with the proposed theoretical model, which predicts overlapping loading and unloading curves. The causes underlying this behavior require deeper study and are not within the scope of this research.

74
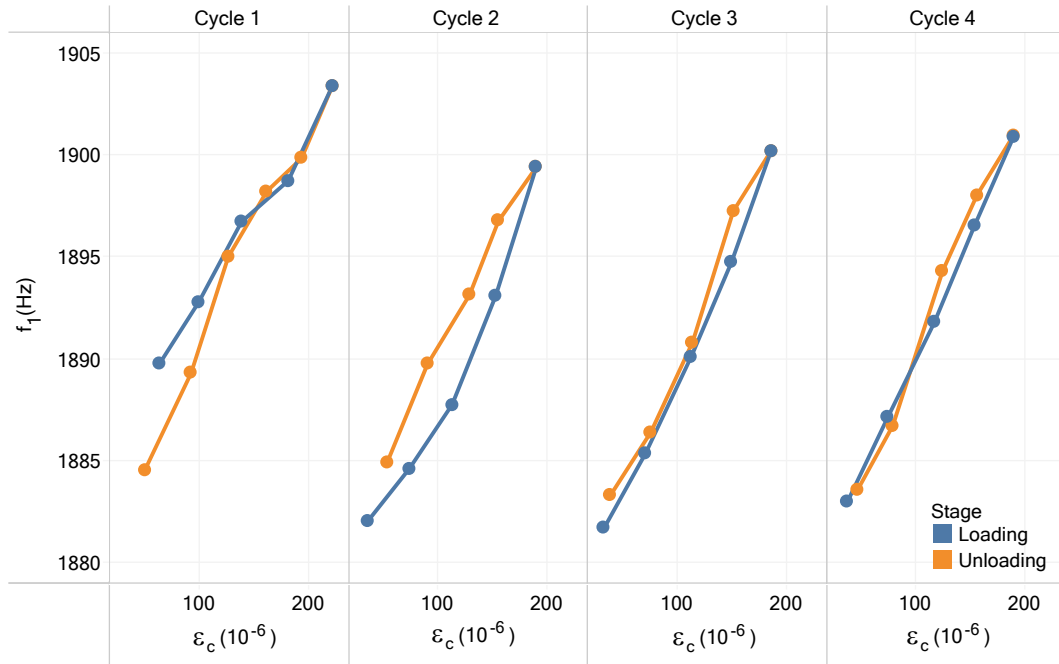
Figure 4.4: Fundamental torsional frequencies corrected considering boundary conditions and temperature with respect to the uniaxial compressive strain ε_c $(= -\varepsilon)$, obtained during the loading and unloading cycles of the acoustoelastic test of prism 1.

Figure 4.5 presents the squared frequency increment results for prisms 1, 2 and 3 with respect to the measured strains. The frequency increment was calculated at every load step as $f_1(\varepsilon)/f_1(0)$ where $f_1(\varepsilon)$ corresponds to the temperature-corrected free-free fundamental frequency of vibration computed at every load step, and $f_1(0)$ is the estimation of that magnitude at zero strain. This estimation was obtained from the linear regression described by equation (3.13).

Figure 4.5 depicts good consistency between the three prisms, both for loading and unloading cycles. Even though the prisms were made from different concrete mixtures, the slopes of frequency increments are very similar.

4.3.4. Results of β_G parameter

Figure 4.6 presents the results of β_G for every prism at every loading/unloading cycle. The β_G values of loading cycle 1 are always lower (in absolute value) than those from subsequent loads. This finding is consistent with the hypothesis that softening occurs during loading cycle 1 and therefore the stiffening effect (associated with negative β_G values) competes with the
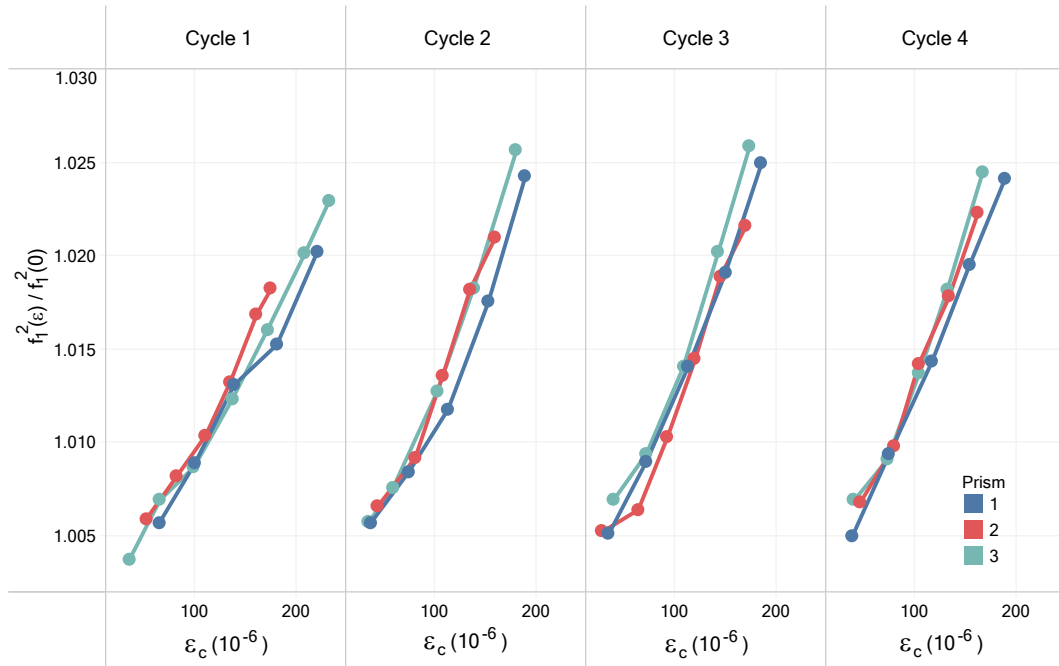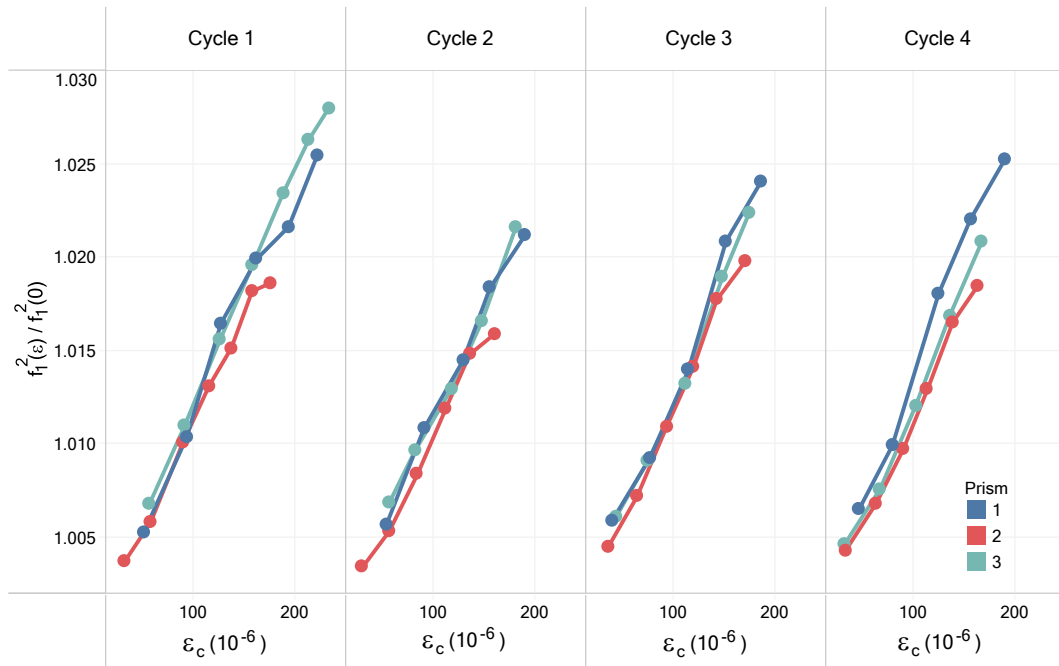
Figure 4.5: Frequency increment results with respect to uniaxial compressive strain $\varepsilon_c \ (= -\varepsilon)$ of prisms 1, 2 and 3 for (a) loading and (b) unloading cycles.

initial softening due to damage or other effect (associated with positive β_G values). After the first loading cycle, β_G values stay within a range of -103 to

-142 for all the three prisms. Table 4.3 shows the mean and standard devia-tion results of β_G associated with each prism for the seven loading/unloading cycles.
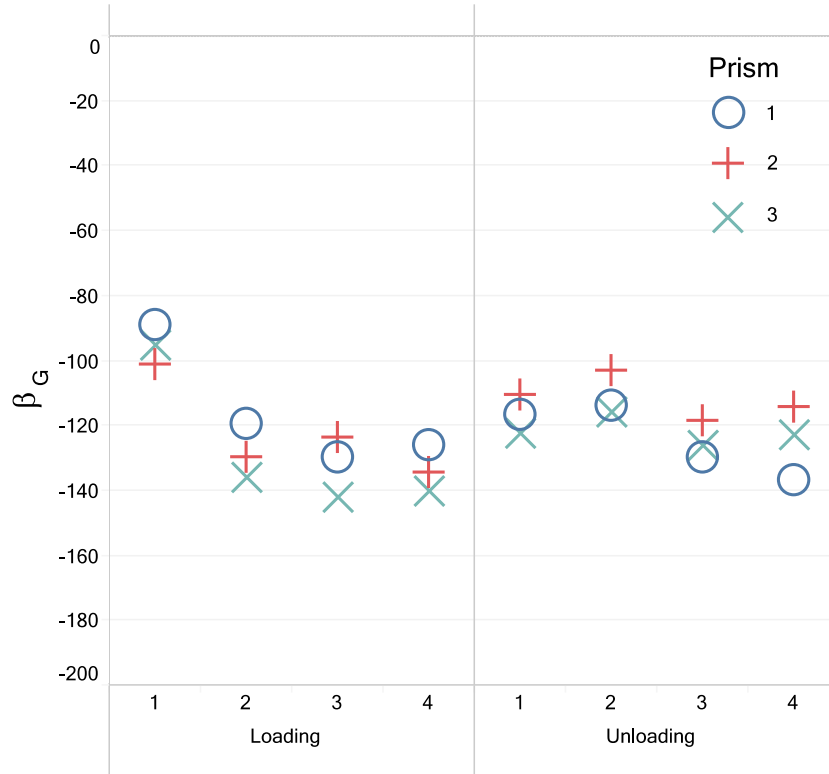
Figure 4.6: Results of β_G for the four loading and unloading cycles of the specimens 1, 2, and 3.

Table 4.3: Mean and standard deviation results for β_G for each prism, neglecting loading cycle 1.

Prism	Mean	Std. dev.
1	-125	8
2	-119	11
3	-129	10

Observe in Table 4.3 that specimen 2, with highest Young's modulus E_0 and compressive strength f_c obtained the lowest mean β_G (in absolute value).

Let us also analyze the variability of the average β_G values among concrete mixtures by computing the coefficient of variation (CV), i.e. the standard deviation over the absolute value of the mean. The CV of the average β_G results among mixtures is 4.1 %, lower in value than both the initial dynamic

Young's modulus and compressive strength, with CV = 14.7 % and 28.5 %, respectively. This analysis is summarized in Table 4.4 where properties among the three mixtures are compared. This suggests that an estimated value of β_G could be used for a concrete that has not been directly characterized, without incurring much error. Characterization of more mixtures is needed to confirm this presumption.

Table 4.4: Summary of concrete properties, including the mean, standard deviation and coefficient of variation (CV) among mixtures.

	Mean	Std. dev.	CV %
ρ (kg/m^3)	2319	67	2.9
E_0 (GPa)	36.9	5.4	14.7
G_0 (GPa)	15.5	2.2	14.2
ν_0	0.19	0.007	3.8
f_c (MPa)	36.1	10.3	28.5
β_G	-125	5	4.1

4.3.5. Comparison with β_G values obtained from literature

The author could not find previous reports that explicitly calculate the nonlinear parameter β_G of concrete. However, it is still possible to use the frequency shift data provided by Lundqvist and Rydén [20] to compute their specimen's β_G, but without applying boundary condition nor temperature corrections. By simply introducing their frequency data into equation (3.13) and applying a linear regression, we obtain β_G = -166 ; this value of β_G is in the same order of magnitude as those presented previously in this chapter, even though our experimental configurations have considerable differences.

To deepen the analysis, let us use the results from the FEM numerical model detailed in Chapter 3 to determine β_G values using second and third order elastic constants experimentally determined in previously published research [17, 64]. Table 4.5 contains the concretes' material properties and β_G associated with the findings of Payan et al. [17] and Nogueira and Rens [64].

Table 4.5 shows that the previously reported concrete's second and third order elastic constants yield results of β_G that are similar (yet lower in value over all) than the β_G values obtained in this research. Their associated β_G

Table 4.5: Second and third order elastic constants of concrete concretes reported elsewhere, with their corresponding β_G according to the numerical model detailed in Chapter 3.

Ref.	ρ (kg/m^3)	E_0 (GPa)	ν_0	l (GPa)	m (GPa)	n (GPa)	β_G
[64]	2327.1	31.31	0.211	-536	-994.5	-885.8	-48
[64]	2308.8	30.07	0.194	-762.6	-1056.5	-1096.8	-57
[64]	2268.3	29.42	0.203	-140	-648.9	-450.1	-32
[17]	N/A	42.39	0.21	-3007	-2283	-1813	-83

values range between -32 and -83 whereas here these range between -119 to -129. Note that these two investigations [17, 64] computed the concrete's third order elastic constants using wave propagation based techniques whereas in the experiments presented here a vibration based technique was used; these fact might explain the differences of measured β_G values, also supported by the β_G (equal to -166) computed from Lundqvist and Rydén's vibration-based data [20]. This topic is investigated and discussed in Chapter 5.

Once the nonlinear parameter β_G of a concrete mixture is established or reasonably estimated for a concrete mixture, a loading/unloading test could be performed in-situ on a concrete element composed of the mixture to estimate the applied stress therein. Using data from that test, equation (3.13) could be used to calculate the current uniaxial strain (ε_1), and thus the current uniaxial stress (σ_1). Details of this potential test are given in Chapter 3.

4.4. Conclusions

Based on an experimental test series and the theoretical model proposed in Chapter 3 (that relates the torsional frequency of vibration in concrete samples with the applied compressive strain and stress), it is verified the model's predictions are true. This is, the existence of a positive correlation between vibration frequency and applied compressive stress, within the limits of compressive strain applied here, caused by the material stiffening nonlinearity (acoustoelasticity). To quantify and characterize this behavior, the nonlinear parameter β_G was utilized, which corresponds to the rate of change of the shear dynamic modulus G with respect to the level of compressive strain. Based on the results presented in this chapter, the following conclusions can be drawn.

- The torsional frequency of vibration of the tested concrete prisms shows

a positive correlation with the applied uniaxial quasi-static compression strain and stress level. The influence of the nonlinear material stiffening dominates over that of geometric nonlinearity (P-δ effect) and possible material softening.

- The effect of changing boundary conditions cannot be neglected with the used experimental configuration. A theoretical-empirical correction to decouple this effect from that corresponding to the material nonlinearity was therefore proposed. Other experimental configurations or field characteristics may increase or reduce the effect of changing boundary conditions on the acoustoelastic effect; this characteristic must be assessed for each situation.

- The initial loading cycle of all prisms yielded β_G values around -95, that were clearly lower (in absolute value) than those obtained from subsequent loading/unloading cycles on the same sample, which averaged -125. Thus, competing stiffening (acoustoelastic) and softening (damage or other) effects occur during the first loading cycle.

- The obtained value of β_G neglecting the first load cycle is consistent among the range of concrete mixtures considered, even though other mixture parameters such as Young's modulus and compressive strength vary significantly. The values of β_G obtained numerically from previously published results, which used vibration-based techniques, are of the same order of magnitude as the ones computed in this investigation. Results of β_G computed from previous studies based on wave propagation techniques yielded values of β_G lower than those computed here.

- Once the nonlinear parameter β_G of a concrete mixture is established, a loading/unloading test could be performed to estimate applied stresses of a concrete element composed of that mixture.

Chapter 5

Experimental comparison of techniques for acoustoelastic characterization: torsional vibration vs. wave propagation

5.1. Introduction

The equations (2.35) through (2.39), developed by Hughes and Kelly [14], relating the mechanical wave speed with applied uniaxial strain (or stress) were presented in Chapter 2. These equations could be used to estimate applied stress in a known solid by measuring wave speed, or inversely, one could measure wave speed and applied stress to find the solid's second order elastic constants (λ and μ) and the third order elastic constants l, m and n. Also, Chapter 3 presented the equations developed in this investigation, particularly equation (3.13), relating torsional frequency of vibration with respect to applied uniaxial strain (or stress). These magnitudes are related by the second order elastic constant G $(= \mu)$ and the nonlinear parameter β_G. This equation could also be used to find the applied uniaxial stress in a known solid by measuring frequency of vibration, or inversely, to compute β_G by measuring applied stresses and torsional frequency of vibration. Such a test was detailed in section 3.6. Moreover, Chapter 3 also contains the analytical development showing the expression of β_G in terms of the third order elastic constants l, m and n (equation (3.51)), including a numerical analysis that substantiates the

81

analytical findings. The present chapter describes and discusses the experiments developed to verify these analytical and numerical findings.

The typical experimental tests designed to measure l, m and n in concrete under compression involve carrying out a loading test of a concrete sample, and during the test, measuring the applied stress and/or strains, as well as the velocity variation of three ultrasonic wave-modes. Thus, using the corresponding equations (2.35) through (2.39), l, m and n can be determined. For concrete materials, this was carried out by Payan et al. [17], and by Nogueira and Rens [64]. The objective of this chapter is to carry out a similar test and obtain a "wave propagation-based" β_G, using equation (3.58) and at the same time determine β_G from torsional frequency of vibration. This is the first time that a study employs these two techniques on the same specimen, for acoustoelastic characterization of concrete, and compares their results. Thus, with both approaches equations (3.58) and (3.51) would be verified, which would in turn verify that the acoustoelastic effect (concrete stiffening effect) is responsible for both effects: the positive correlations between wave speed and uniaxial compression and between frequency of vibration and uniaxial compression.

The experiments described in this section involved loading a concrete-material specimen, measuring stresses, strains, wave propagation velocity and torsional frequency of vibration. Thus, β_G was computed from both techniques: ultrasonic wave propagation, and torsional resonance. It would be expected to find equal (or very similar) β_G results, which would prove that the proposed theory agrees with the experimental observations. However, preliminary tests carried out in concrete samples showed results of β_G computed from the wave propagation technique an order of magnitude lower than β_G results computed from the torsional resonance technique. One of the main differences between both techniques is the frequency of vibration at which the dynamic phenomena are occurring, much higher in the case of wave propagation, $\sim$150 kHz, than for torsional resonance $\sim$2 kHz. It was therefore initially presumed that there could be an effect of the intrinsic concrete heterogeneity, in which the existence of aggregate of considerable size could be affecting propagating waves, and thus, producing lower values of β_G. Note that a shear wave centered at 150 kHz traveling at 2000 m/s would have a wavelength of 1.3 cm, which are of the same order of magnitude as the coarse aggregate size. If this was true, it would mean that wave propagation "sees" concrete more linear than resonance tests. Therefore, to address this issue, a mortar concrete sample was cast (cement,

water and sand, without coarse aggregate), so that the solid could be considered homogeneous both for wave propagation and for resonance. The following description involves the mortar sample. Moreover, other affecting factors that could alter the measured β_G were considered, and specific experimental actions were taken; these are, for example, the effect of temperature, the conditioning effect (slow dynamics) produced by the actuator - experimentally observed as an instantaneous softening which tends to recover in time- and the damaging effect due to increasing the maximum historical compressions -also observed as a softening effect- [83, 84]. These descriptions are presented in Materials and Methods section, and the results analyzed in the Results and Discussion section.

The reader will note that despite the mentioned experimental considerations, the wave propagation technique yielded β_G results considerably lower than the torsional resonance technique, meaning that the previously posed theory is incomplete. Thus, a final section has been included in order to pose an extended theory, which includes concepts of viscoelasticity, and is potentially capable of successfully explaining the observed experiments. It should be noted that there are other possible influencing factors that may also explain the apparent discrepancy and these were not addressed in this Thesis; some of these are: inaccuracies while measuring nonlinearity (β_E) from quasistatic stress and strain data, as well as the assumed relationship between β_E and β_G, the hypothesis of considering Poisson's ratio to be frequency independent when calculating dynamic shear moduli G from P-waves, longitudinal vibration and bending vibration, and also the fact that frequencies of vibration, from which dynamic elastic moduli are calculated, depend on the dynamic strain range used for their characterization [72, 83].

5.2. Materials and Methods

5.2.1. Material and Specimens

The experimental campaign comprised two mortar prismatic specimens of nominal dimensions $15 \times 15 \times 60$ cm^3 and three standard companion cylinders of dimensions 10 cm of diameter and 20 cm tall. One prismatic specimen was used in the acoustoelastic test. The second prismatic specimen was set aside to control temperature variations. The companion cylinders were used to find

the mortar's compressive strength. The mortar mixture had a water to cement ratio of 0.68. The mixture proportions are given in Table 5.1.

Table 5.1: Mixture proportions of mortar mixture design expressed as weight per m^3 of mortar mixture, with constituents in SSD condition.

	weight (kg)
Portland cement	400
water	272
sand (SSD)	1883

"SSD" means saturated surface dry condition.

The average compressive strength of the three cylinders was 20.4 MPa, tested at day 28 after casting, following ASTM C39/C39M [25] and ASTM C192/C192M [82].

5.2.2. Characterization of Second Order Elastic Constants

Prior to carrying out the acoustoelastic testing program, which involved loading the sample several times, various nondestructive tests were performed. First, the specimen was measured and weighed to calculate density. Afterwards, the mortar sample was tested using traditional longitudinal, flexural and torsional resonance, as indicated in ASTM C215 [9]. With these, the dynamic elastic moduli E and G (or μ) were calculated.

Finally, the mortar specimen was characterized using traditional wave propagation techniques. A pair of P-wave ultrasonic transducers were attached on opposing lateral sides of the prismatic specimen, using the UPV Pundit equipment. The pulse, with a frequency spectrum centered at 54 kHz, was sent by the sending transducer, traveled through the solid, and sensed by the receiving transducer, where the time of flight was measured. The P-wave speed V_P was computed by dividing the distance between transducers into the time of flight. Note that, by definition, $V_P = V_{22,0}$ using the axes convention of equation (2.35) through (2.39). Similarly, V_P was also measured using another pair of transducers model Olympus V1548 which sent/sensed pulses with frequency spectrum centered at 150 kHz (originated from a pulser model Olympus 5072PR). Once the V_P was measured, the dynamic E can be computed using equations (2.6). The dynamic G (= μ) can be estimated by considering a reasonable value of Poisson's ratio.

84

5.2.3. Acoustoelastic Testing Program

The acoustoelastic testing program was divided into three tests: Test 1, Test 2 and Test 3, which were performed in order from 1 to 3. These are depicted in a stress vs. time graph, presented in Figure 5.1.
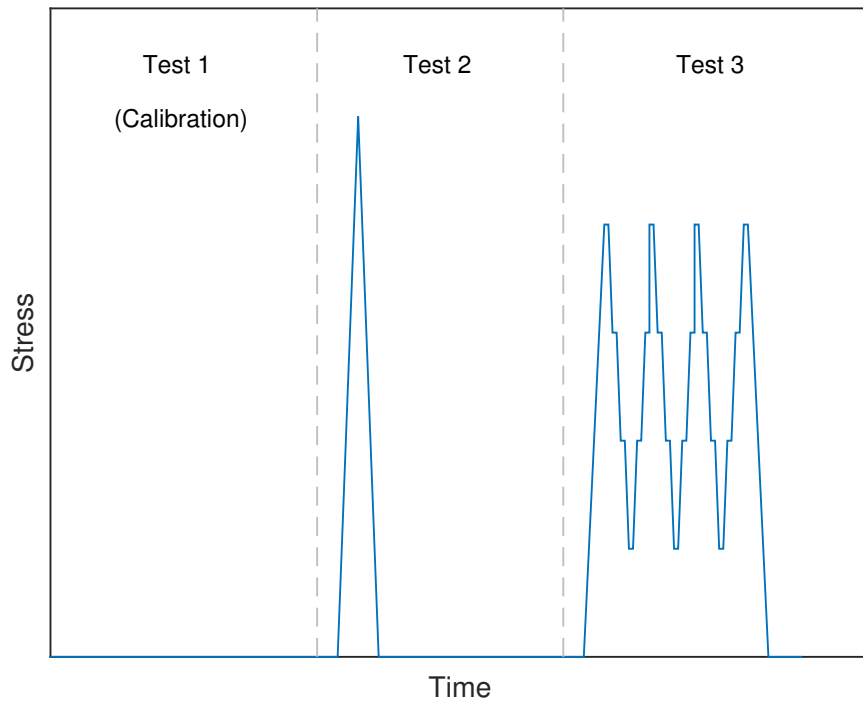
Figure 5.1: Diagram of testing program protocol indicating tests 1, 2 and 3 in time.

Each of these tests had their own specific goal in order to improve the accuracy to determine β_G. Each test involved monitoring the S-wave speed V_{21} and/or torsional vibration frequency. The objective of Test 1 was to study the effect of temperature on S-wave speed and to establish a correlation between the testing specimen and the control specimen. The objective of Test 2 was to submit the specimen to a maximum historical compressive stress (which would not be exceeded in Test 3), and also to observe slow dynamic effects, like material softening and gradual recovery. The goal of Test 3 was to measure β_G with both techniques and to compare the obtained results.

5.2.4. Testing configuration and signal processing for wave speed monitoring

The testing configuration for wave speed monitoring consisted of attaching a pair of S-wave transducers model Olympus V1548 onto opposing sides of the prisms' lateral faces. These were set so that wave polarization would be parallel to the loading direction, thus, to send/sense S-waves traveling at speed V_{21}. Figure 5.2 depicts the experimental configuration.
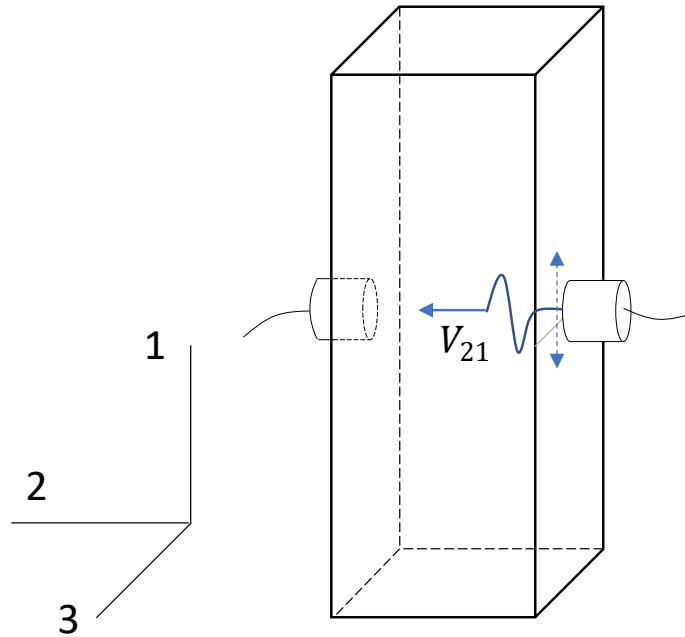
Figure 5.2: Diagram of wave speed monitoring experimental configuration, showing transducers, and indicating direction of wave propagation with continuous blue arrow V_{21} and direction of wave polarization with dashed blue arrow.

Sixteen individual pulses (not a burst) were produced by a pulser model Olympus 5072PR to excite the sending S-wave transducer and sent through the specimen. These propagating waves were sensed by the receiving S-wave transducer on the opposite side of the specimen. The analog pulses were acquired and digitized by a Tektronix oscilloscope model TDS 2004B with 25 MHz sampling frequency. The sixteen pulses were time-averaged by the oscilloscope. The time-averaged signal was transferred to the controlling personal computer. Three of these time-averaged time-domain signals were recorded with the personal computer and were averaged once more in order to improve the signals' vertical resolution. These "improved" time domain signals were recorded at a rate of one every 90 s.

The digitized time-domain signals were processed using MatLab in order to monitor S-wave speed V_{21}. The very first signal was recorded during Test 1, which became the "base signal". The S-wave arrival of the base signal was determined by direct observation of the arriving pulse. The signals were filtered using a Butterworth 750 kHz low pass filter of 2nd order. Then they were windowed using a Tukey window in order to keep the first two cycles of the S-wave arrival. All the windowed time domain signals were "splined" by interpolating 200 points between each consecutive pair of signal points, artificially creating signals with 500 MHz sampling rate. Then these were cross-correlated against the base signal in order to quantify the arrival time variations, and thus the wave speed V_{21} changes. Figure 5.3 shows a typical raw signal collected using the shear wave setup and a processed signal superimposed.
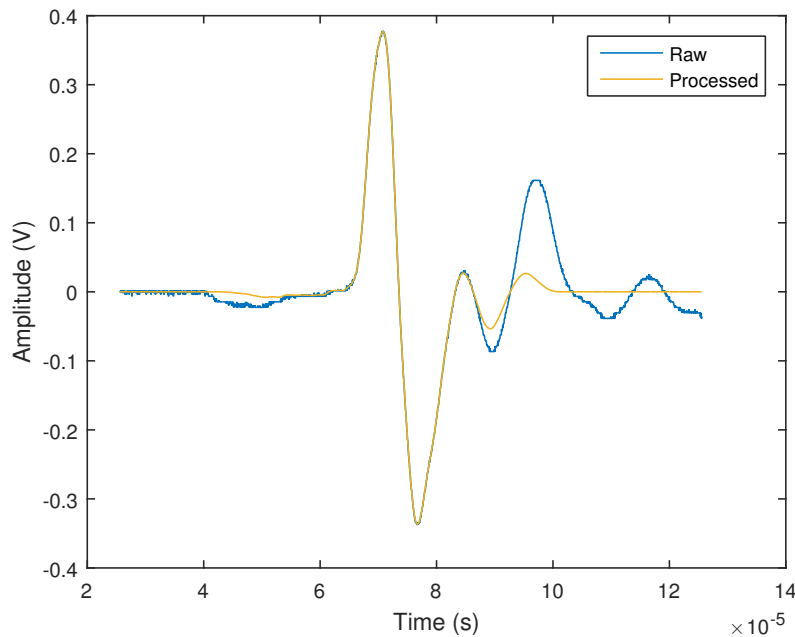
Figure 5.3: Typical signal acquired with the shear wave mode 21 setup. In blue the raw signal and in yellow the processed signal.

5.2.5. Testing Configuration and Signal Processing for Vibration Monitoring

The testing configuration and signal processing used within this testing program was identical as explained in Chapter 4. The low-energy impacts

were applied to the sample in moments where S-waves were not propagating. A special preliminary test was carried out to verify that S-wave speed was not affected by the impacts, or, in other words, that the impacts were not conditioning the material.

5.2.6. Test 1: Effect of Temperature on Wave Speed

Test 2 and 3 involved monitoring wave speed changes during several hours, where temperature varied and affected the experimental results. Test 1 was run in order to study the effect of temperature on the material, and specifically to investigate the possibility of using a control specimen to account for these temperature changes.

To pose a possible correlation equation between control and testing specimen, let us start by assuming that the elastic modulus G is linearly affected by temperature changes. Thus the temperature-dependent and strain-dependent shear modulus, $G_{\varepsilon,T}$, is related to the existing temperature T and the applied uniaxial strain ε with

$$G_{\varepsilon,T}(\varepsilon, T) = G_{0,T0} \left(1 + \beta_G \varepsilon\right) \left(1 + b_G \Delta T\right), \tag{5.1}$$

where $\Delta T = T - T_0$ and T_0 is a reference temperature which is arbitrarily selected and must then remain unchanged; $G_{0,T0}$, is the elastic shear modulus of the material at 0 strain (undeformed state) and at temperature T_0, and b_G is the factor relating temperature changes with shear modulus changes. Note that the use of this equation assumes that G is temperature dependent but not β_G.

Note that equation (5.1) is basically the same as the equation (3.6) with the difference that the temperature factor $(1 + b_G \Delta T)$ has been introduced to account for temperature shifts. At temperature $T = T_0$ equation (5.1) becomes equivalent to (3.6). Let us call that factor $i_G(\Delta T)$, thus

$$i_G(\Delta T) = (1 + b_G \Delta T) = \frac{G_{\varepsilon,T}}{G_{\varepsilon,T0}}, \tag{5.2}$$

where $G_{\varepsilon,T0} = G_{0,T0} \left(1 + \beta_G \varepsilon\right)$.

From this model, b_G is the parameter that relates temperature shifts and their effect on the shear modulus G. However, our preliminary experiments have shown that this relationship is hysteretic, which complicates its model-

ing and characterization testing. Thus, instead of characterizing b_G, it was opted to use the control specimen and assume that the variations $i_G(\Delta T)$ that undergoes the testing specimen are linear with the variations $i_{G,(C)}(\Delta T)$ that undergoes the control specimen. This is

$$i_G(\Delta T) = n_T + m_T \times i_{G,(C)}(\Delta T), \qquad (5.3)$$

where the subindex (C) stands for "control", and m_T and n_T are the two linear coefficients needed to be determined during a calibration test.

Note also that the increments of G are proportional to the increments of S-wave speed V_S squared. So, $i_G(\Delta T)$ can be directly measured by measuring the S-wave speed change on a sample that is only subjected to temperature changes, that is

$$i_G(\Delta T) = \frac{G_{\varepsilon,T}}{G_{\varepsilon,T0}} = \frac{V_{\varepsilon,T}^2}{V_{\varepsilon,T0}^2}, \qquad (5.4)$$

where $V_{\varepsilon,T}$ and $V_{\varepsilon,T0}$, are the S-wave speeds measured with the sample at uniaxial strain ε and temperature T, and at temperature T_0, respectively (note that the subindices "S" and "21" of the wave speeds V have been dropped to ease the nomenclature, but these still correspond to S-waves mode 21). By substituting equation (5.4) into (5.3) we obtain

$$\frac{V_{\varepsilon,T}^2}{V_{\varepsilon,T0}^2} = n_T + m_T \times \frac{V_{0,T,(C)}^2}{V_{0,T0,(C)}^2}, \qquad (5.5)$$

where (C) indicates the control specimen, and the subindex $\varepsilon = 0$ for the control.

Thus, coefficients m_T and n_T can be obtained from a calibration test involving monitoring S-wave speed variations on both unloaded specimens ($\varepsilon = 0$). This was done during Test 1. The coefficients n_T and m_T are those that best fit equation (5.5) during this test.

Once the calibration test is carried out, and factors m_T and n_T determined, we can consider any test in which temperature changes are occurring coupled to other effects (such as in Tests 2 and 3), and decoupled the former from the latter. An S-wave speed measurement can be corrected for temperature variations by isolating $V_{\varepsilon,T0}^2$ from equation (5.5), which yields

$$V_{\varepsilon,T0}^2 = \frac{V_{\varepsilon,T}^2}{n_T + m_T \times \left(\frac{V_{T,(C)}}{V_{T0,(C)}}\right)^2}, \tag{5.6}$$

where $V_{\varepsilon,T}$ is the measured S-wave speed on the testing specimen at a given temperature T, $V_{\varepsilon,T0}$ is the temperature corrected S-wave speed, that is, the wave speed that the testing specimen would have had at temperature T_0, $V_{T,(C)}$ is the S-wave speed of the control, measured at the same time than $V_{\varepsilon,T}$ and $V_{T0,(C)}$ is the S-wave speed measured during the calibration test at temperature T_0.

Test 1 (the calibration test) consisted of placing both the testing specimen and the control in their exact experimental configuration that they would have during Test 2 and Test 3, and to monitor S-wave speed on both samples in a lapse where no other effects were occurring but only temperature variations. The experimental configuration used for Test 1 is detailed in section 5.2.4 and lasted 35 hours. The temperature T_0 was 17.6 ^oC , which corresponded to the air temperature reading when the base signal was collected. The factors m_T and n_T were computed from the S-wave speed data collected during that time, using equation (5.5). These best-fit coefficients were used in Tests 2 and 3 to "normalize" S-wave speeds to temperature T_0 by applying equation (5.6).

5.2.7. Test 2: Peak Load and Long-term Monitoring

Test 2 consisted of gradually applying up to 4.5 MPa of uniaxial compression onto the testing specimen, and then gradually releasing it to reach 0 stress once again, both at a rate of 500 N/s. During the loading/unloading cycle, longitudinal strains were measured at a rate of one per second using a pair of strain gauges attached to opposing sides of the specimen, connected to a Wheatstone bridge in a quarter bridge configuration. S-wave speed V_{21} were monitored both in the testing specimen and in the control specimen, using the experimental setup explained in section 5.2.4. The S-wave monitoring was prolonged for approximately 75 hours after releasing the stress.

Test 2 had two objectives. First, to apply a maximum compressive load (4.5 MPa) that would not be exceeded during Test 3. Based on the Kaiser effect, if the maximum historical load is not exceeded during a given test, then no significant material damage occurs. Thus, because in Test 3 compressions reached up to 3 MPa, no significant damage occurred during Test 3. This is

important because Test 3 would be used to characterize acoustoelasticity.

The second objective consisted in monitoring the specimen during a long period of time in order to study the existence of material conditioning/recovery due to slow dynamics effects.

5.2.8. Test 3: Acoustoelastic Test

Test 3 consisted of carrying out four loading and unloading cycles onto the testing specimen and, throughout the test, carry out torsional vibration and S-wave propagation tests. Load was increased and decreased at a rate of 100 N/s. Within each loading cycle, five load steps were defined, in which load was kept constant for 10 minutes, to allow measuring torsional vibration. The testing protocol is shown in Figure 5.4. The longitudinal strains were measured using a pair of strain gauges and a Wheatstone bridge, at a rate of one per second.
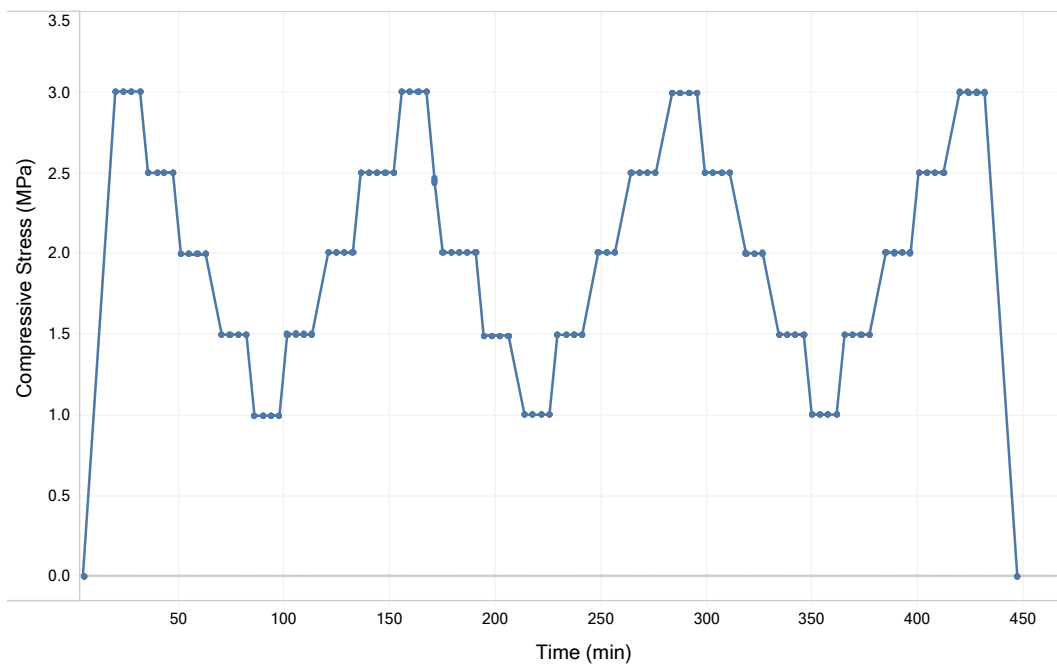
Figure 5.4: Applied compressive stress in time during Test 3. Markers point the times in which torsional vibration measurements were taken.

Torsional vibration measurements were taken only during the steps in which load was kept constant. The experimental configuration and procedure is detailed in section 5.2.5. The S-wave propagation measurements were taken continuously and not only during the load steps; more experimental details

91

are given in section 5.2.5. Figure 5.5 is a photograph showing the testing configuration used during Test 3. The torsional vibration measurements were used to calculate β_G as detailed in Chapters 3 and 4. The S-wave speed measurements were corrected for temperature as explained in section 5.2.6 and then they were used to calculate β_G using equation (3.58).
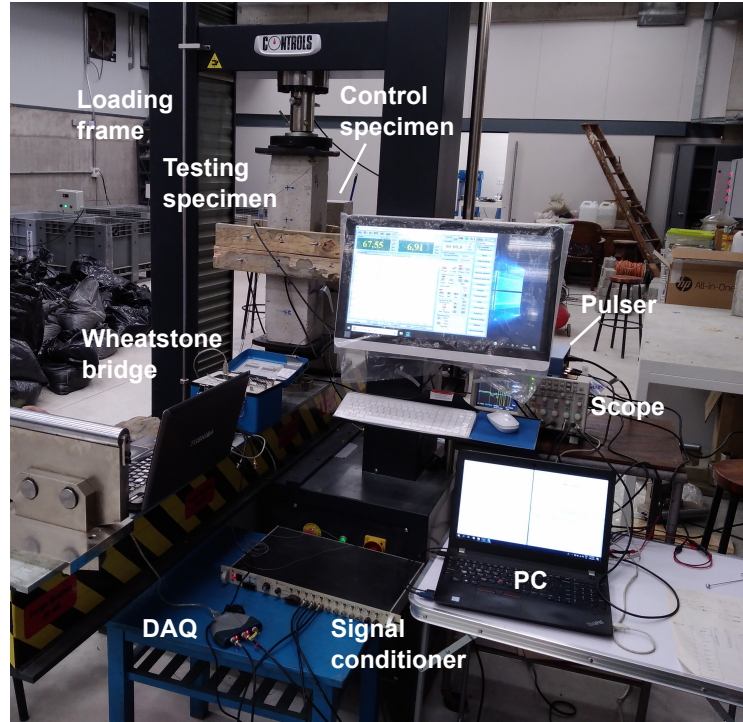
Figure 5.5: Photograph of the testing configuration employed for Test 3.

5.3.   Results and Discussion

5.3.1.   NDE Characterization Results

The density of the testing specimen was 1981 kg/m^3. Results of resonance vibration are presented in Table 5.2. Results of P-wave speed are presented in Table 5.3.

5.3.2.   Results of Test 1: Effect of Temperature on Wave Speed

Figure 5.6a presents the results of wave speed variations associated to S-wave speed $V_{0,T}$, which is a vertically polarized S-wave, that is, a 21 mode, and

Table 5.2: Results of resonance tests (free vibration) on testing specimen and computation of dynamic shear modulus G.

Mode	f (Hz)	G (GPa)
flexural	1214.2	$9.54^{(1)}$
longitudinal	2852.2	$10.00^{(1)}$
torsional	1689.0	9.79

(1) Poisson's ratio considered 0.18 for calculations.

Table 5.3: Results of P-wave speed tests and calculation of dynamic shear modulus G.

Transducers	Speed (m/s)	G (GPa)
54 kHz	3908	$11.81^{(1)}$
150 kHz	3926	$11.91^{(1)}$

(1) Poisson's ratio considered 0.18 for calculations.

control S-wave speed $V_{T,(C)}$, collected during Test 1, where air temperature measurements have been superimposed. In that figure it is observed that both magnitudes, $V_{0,T}$ and $V_{T,(C)}$ are overlapping and they both lag from the temperature curve; where wave speed decreases as temperature increases. Note also that the $V_{0,T}$ measurements are plotted against the left y-axis and the $V_{T,(C)}$ against the right y-axis. These axes are not synchronized on purpose (to allow the magnitudes to overlap) and show that their scale only differs by linear shifts. This shows, qualitatively, that a linear transformation between these magnitudes is sufficient to account for the long term thermal effects on S-wave speed. This trend is better depicted in Figure 5.6b which shows the relationship between these magnitudes.

Figure 5.6b shows the $V_{0,T}$ plotted with respect to control data $V_{T,(C)}$, in terms of the square of their increments. These sets of data were used to apply the linear regression given by equation (5.5), to find the coefficients m_T and n_T. The linear regression yielded a coefficient of determination R^2 equal to 0.99 and the obtained best fit coefficients are $m_T = 1.1745$ and $n_T = -0.1753$.

5.3.3. Results of Test 2: Peak Load and Long-term Monitoring

Figure 5.7 presents the results of S-wave collected during Test 2. The top graph contains the uncorrected results and the bottom graph the temperature-
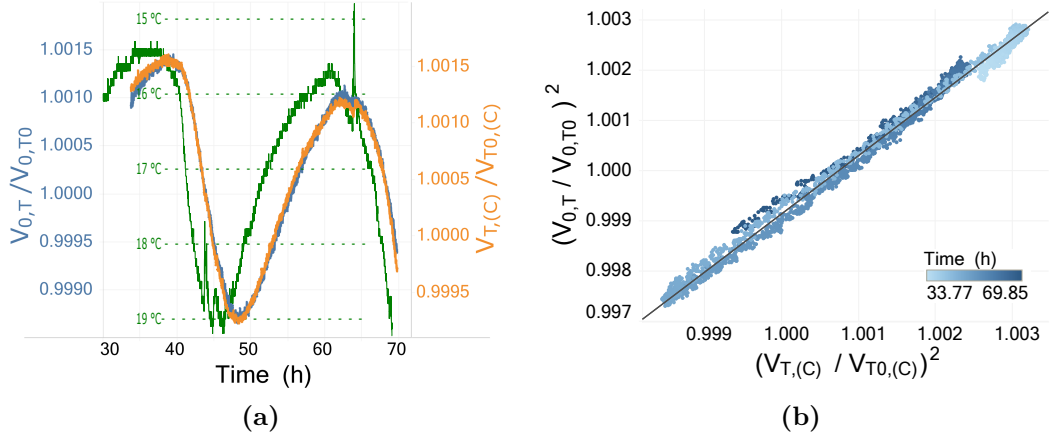
Figure 5.6: Test 1 results. (a) S-wave speed increments on the testing specimen (plotted against left axis) and on the control specimen (plotted against right axis) with respect to time and the overlapped green graph indicates air temperature with respect to time. (b) Squared S-wave speed increments of: testing specimen with respect to control specimen, with time in color code. Continuous black line is the best-fit line.

corrected results. These are the S-wave speeds that would have been collected if air temperature had been kept constant at $T_0 = 17.6\ ^oC$. During Test 2, air temperature stayed between 16 ^oC and 20 ^oC, similarly as during the calibration Test 1.

In Figure 5.7, the first notable feature is the effect of temperature that makes wave speed vary with a period of approximately 24 hours. This effect is present in the top graph, and disappears in the bottom graph due to the successful application of the temperature correction procedure.

Moreover, S-wave speed has a steep spike of approximately 3 m/s increment (0.13 %) between hour 91 and 92, time in which the testing specimen was submitted to 4.5 MPa of uniaxial compression (this is observed in both uncorrected and corrected data). Note in the top graph, that wave speed variations due to temperature are of the same order of magnitude as those due to applied stress. This behavior is depicted in the zoomed graph, where it becomes evident that S-wave speed follows the same trend of increment as the applied compression. However, it can be observed that during the unloading, as stress goes back to zero, S-wave speed reaches a level approximately 2 m/s lower than the starting speed (note the difference of S-wave speed between times 91.6 h and 91.8 h).

As the specimen is left at rest, with 0 stress, S-wave speed starts to gradu-

94
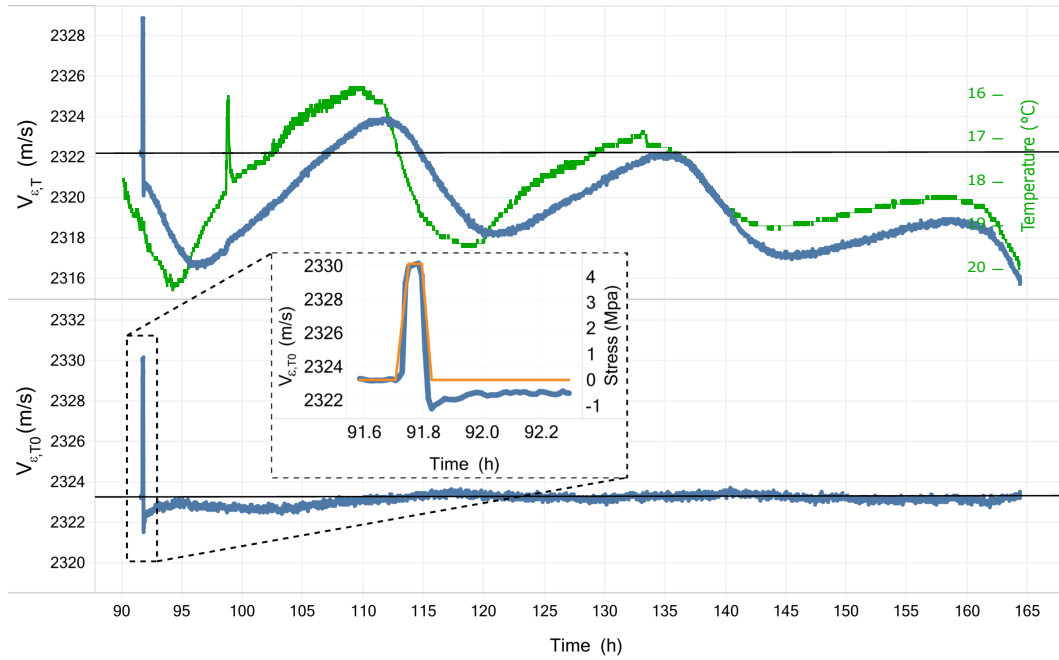
Figure 5.7: Top graphic shows results of S-wave speed $V_{\varepsilon,T}$ uncorrected for temperature (subindex 21 omitted even though it corresponds to mode 21) along time (blue curve), with air temperature superimposed (green curve). Bottom graphic shows results of S-wave speed $V_{\varepsilon,T0}$ corrected for temperature (subindex 21 omitted even though it corresponds to mode 21) along time. In both plots, continuous black horizontal line indicates the starting S-wave speed. Zoomed plot details the loading stage of Test 2, where the level of compression has been incorporated in orange.

ally recover, reaching its initial level around time 110 h. This could be a slow dynamics softening/recovery effect, most likely activated by the quasistatic loading/unloading, which softens or "conditions" the material, and, from these observations, seems to take around 18 hours to fully "recover". Similar behavior has been observed in concrete materials submitted to high energy impacts [83, 84].

5.3.4. Results of Test 3: Acoustoelastic Test

Figure 5.8 contains the uniaxial compressive stresses and strains measured during the test expressed as a function of time. As compressive stresses increase, compressive strains increase too. As expected, the strain measurements follow a very similar trend as the applied uniaxial stress. The same data is plotted in Figure 5.9 but depicting compressive stresses as a function of compressive strains, where the four loading cycles are identified with the color

code. There it can be seen, even though there is minor hysteresis, that all cycles overlap and at the end there is a remnant strain of 4×10^{-6}.
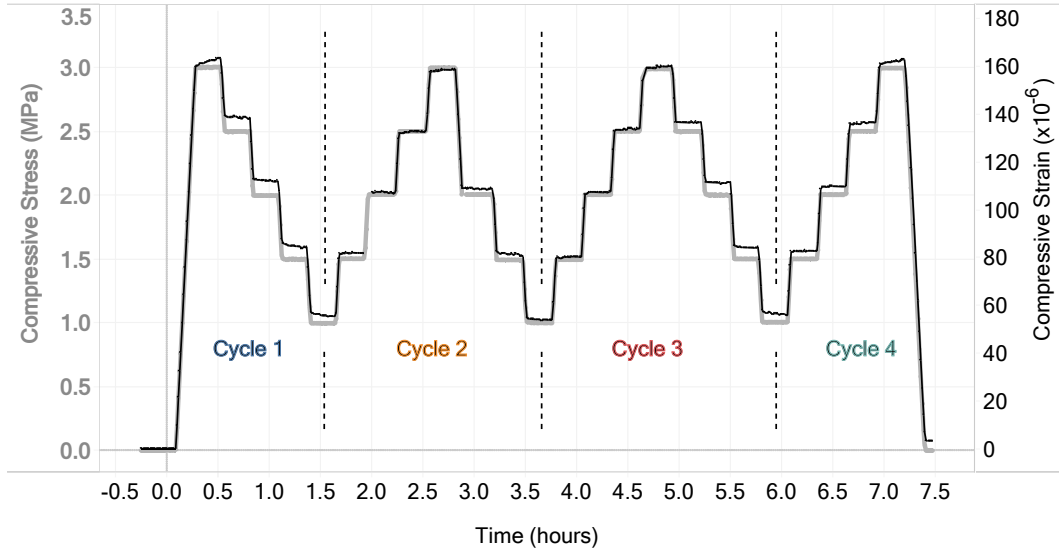
Figure 5.8: Results of compressive stresses, plotted against the left y-axis, and compressive strains, plotted against the right y-axis, expressed as a function of time. Loading cycles 1, 2, 3 and 4 are also identified.
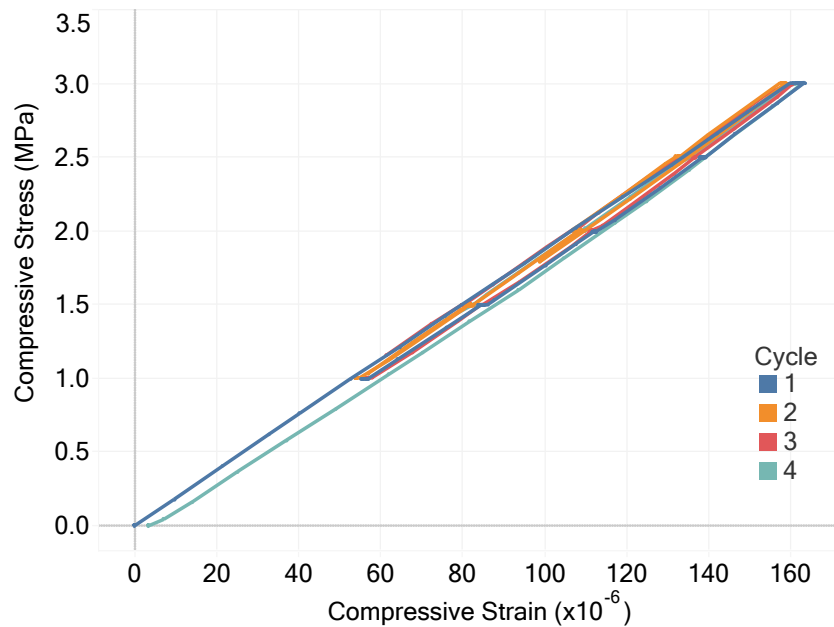
Figure 5.9: Compressive stress as a function of compressive strain during Test 3. Loading and unloading cycles in color code.

Figure 5.10 presents the results of squared S-wave speed with respect to the uniaxial compressive stress, and to the uniaxial strain, for the four loading

cycles. According to the proposed theory, this relationship should be linear, see equation (2.38). The focus was on the behavior between 1 to 3 MPa of compression from which to compute β_G. In this range of stresses, Figure 5.10 shows very good repeatability as all cycles overlap. As compressive stress (and strain) increases, squared S-wave speed increases too. This relationship is fairly linear during the first four load steps, between 1 to 2.5 MPa, and it flattens down at 3 MPa, meaning that if the behavior was purely acoustoelastic, S-wave speed at 3 MPa should have been higher.
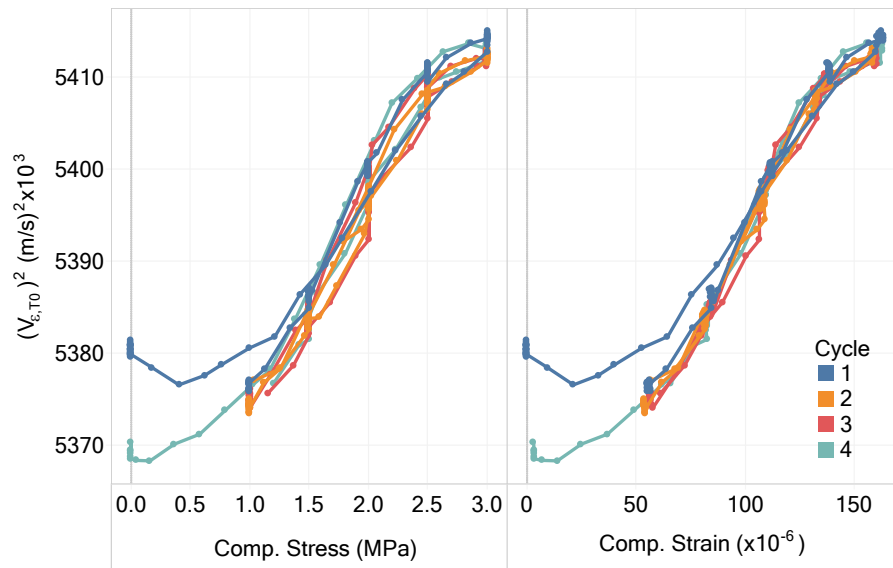
Figure 5.10: Square of temperature-corrected S-wave speed $V_{\varepsilon,T0}$ (subindex 21 omitted even though it corresponds to mode 21) with respect to uniaxial compressive stress at left plot and with respect to uniaxial compressive strain at right plot.

Moreover, in Figure 5.10 it is clear that during the loading stage of cycle 1, S-wave speed behaves in different manner than in the other cycles. During this cycle, as load is increasing, S-wave speed decreases between 0 to 1 MPa and then, after 1 MPa, starts to increase. Similar "erratic" behavior has been observed by some researchers when carrying out similar tests; in some cases the effect is more prominent and in some others very minor [56, 69, 70]; thus, it does not seem to exist a complete explanation for it yet. However, the S-wave speed at the end of cycle 4, with 0 stress, is 0.09 % lower than the initial stress at the beginning of the test, with 0 stress too. This is a similar behavior to the wave speed drop observed in Test 2, that occurred before and after the application of the load, which then took 18 hours to recover; thus, both drops are probably due to the conditioning effect of the quasistatic load

which softens the material. It is therefore likely that the "erratic" effect in cycle 1 could be due to the competing effects of acoustoelasticity, a stiffening effect which makes S-wave speed increase as compression increases, and the slow dynamics conditioning effect, which softens the material during that first load, and if the loading is maintained, the material continues to behave in a conditioned state.

Figure 5.11 presents the temperature-corrected S-wave speed results, and stresses, in terms of the measured compressive strains, but separated among the different loading and unloading cycles. In this figure it becomes clear that within each loading cycle, stress-strain curves show minor hysteresis. There are also some minor viscoelastic effects in which strains keep increasing during the load steps where stresses are kept constant. The stress-strain curves are almost linear, even though they display a slight positive curvature (stiffening effect).
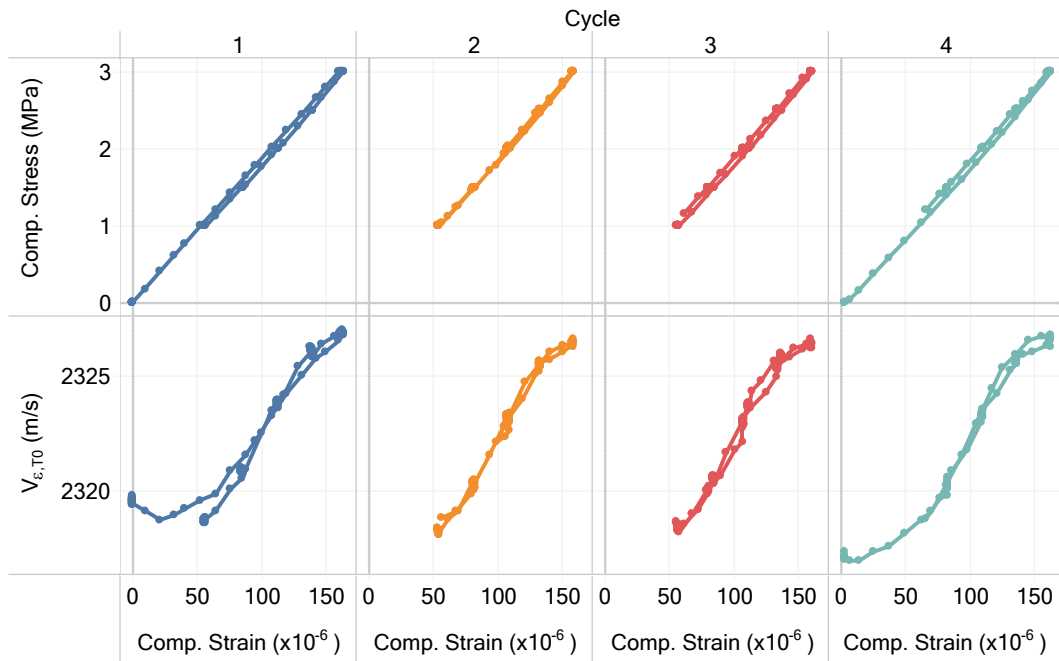
Figure 5.11: Top row plots: Compressive stress with respect to compressive strain, distinguished per cycle. Bottom row plots: temperature-corrected S-wave speed $V_{\varepsilon,T0}$ (subindex 21 omitted even though it corresponds to mode 21) with respect to uniaxial compressive strain, distinguished per cycle.

Figure 5.12 and Table 5.4 contain the results of β_G computed from the temperature-corrected S-wave speed measurements for each loading/unloading stage of each cycle. Results of β_G vary between -91.9 and -96.8 among cycles.

Their average β_G result equals -94.8 with a CV equal to 2.1 %. The fact of obtaining such a narrow range of β_G results confirms the good repeatability among cycles.

Table 5.4: Results of β_G computed from the temperature-corrected S-wave speed measurements for each loading/unloading stage of each cycle.

Cycle	Stage	β_G
1	Loading	N/A
1	Unloading	-95.6
2	Loading	-91.9
2	Unloading	-93.0
3	Loading	-96.4
3	Unloading	-95.1
4	Loading	-96.8
4	Unloading	N/A
Average		-94.8
CV (%)		-2.1
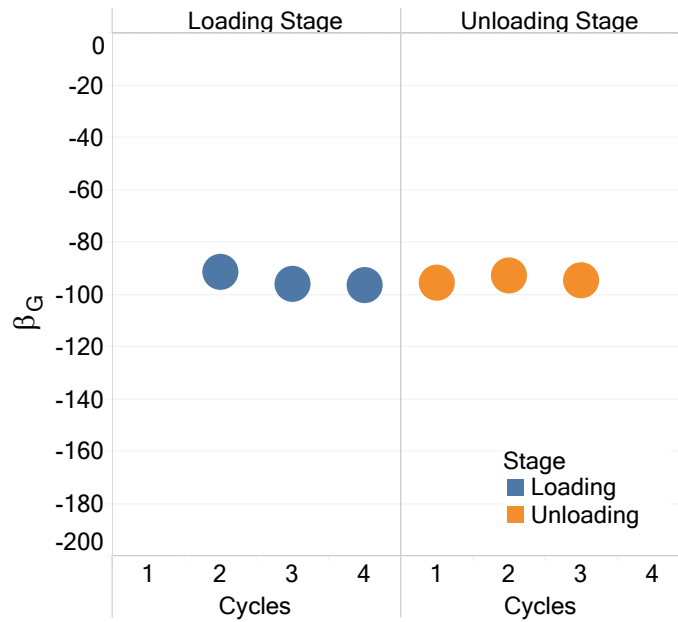
Figure 5.12: Results of β_G obtained from temperature-corrected S-wave speed measurements among loading/unloading stages of the four cycles of Test 3.

Figure 5.13 shows the results of squared fundamental torsional frequency of vibration with respect to compressive strain, measured during the four loading/unloading cycles of Test 3. In contrast to S-wave speed measurements,

which were collected continuously as load was increasing/decreasing, the frequency measurements were collected during the load steps, where stresses were set constant. Thus, the continuous lines connecting the markers are merely descriptive. The dashed lines indicate the loading-increasing stage of cycle 1 and the unloading stage of cycle 4 but do not represent the actual frequency vs. stress (and strain) trends.
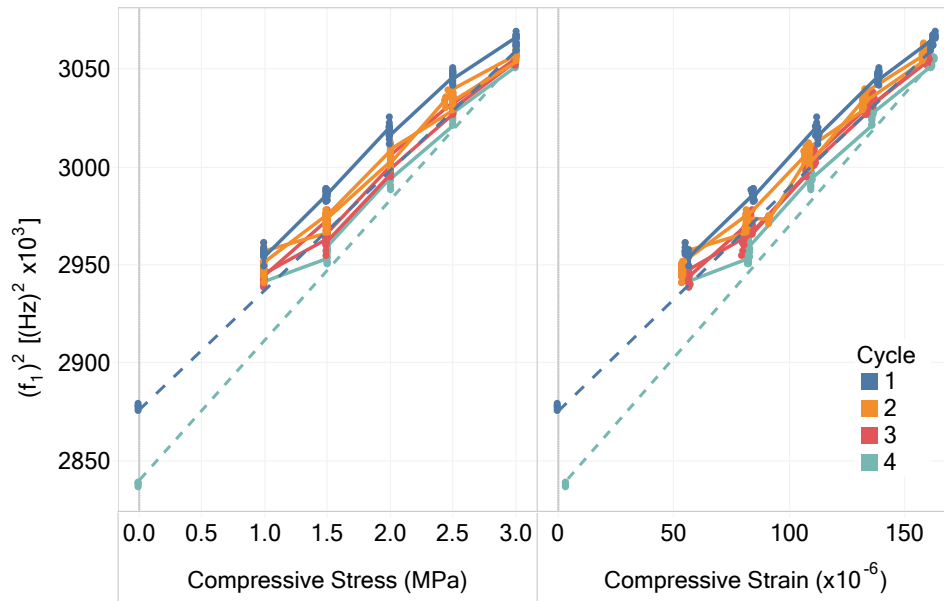
Figure 5.13: Results of the square of the fundamental torsional frequency of vibration, $(f_1)^2$, with respect to compressive strain during the four cycles of Test 3. Dashed lines indicate loading-increasing stage of cycle 1 and unloading of cycle 4.

Figure 5.13 shows that there is a clear positive correlation between the squared torsional frequency and compressive strain. The curves overlap, so there is good repeatability among cycles. In loading-increasing stage of cycle 1, the behavior does not show an initial frequency reduction between 0 to 1 MPa, as the S-wave speed did. However, the frequency obtained at the end of cycle 4, with 0 stress, was a 0.7 % lower than the staring frequency at the beginning of cycle 1 with 0 stress. This behavior, where frequency drops between the start and the end of Test 3, was also observed with the S-wave speed measurements. However, frequency dropped approximately ten times more than S-wave speed did, in terms of percent difference.

Figure 5.14 presents the fundamental torsional frequency of vibration measurements with respect to compressive strain, separated among cycles. It becomes clear that within each cycle, the loading and unloading stages match

very well. The frequency (and squared frequency) vs. strain behavior is linear, yielding best fit lines with coefficients of determination varying between 0.981 and 0.993 (frequency data at 0 stress not included for trendlines calculations)
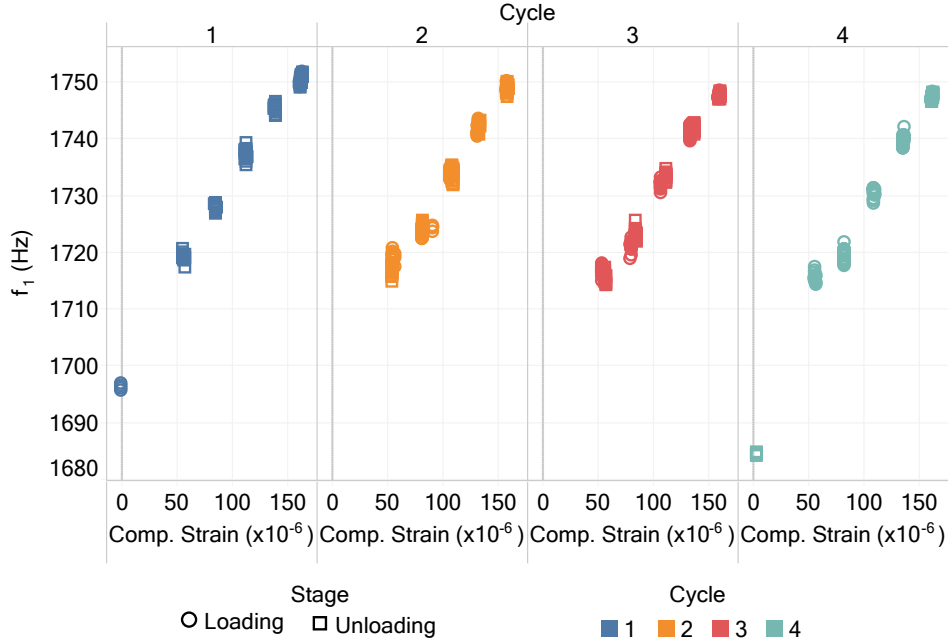
Figure 5.14: Results of fundamental torsional frequency of vibration, f_1, with respect to uniaxial compressive strain for each cycle.

One important difference between the S-wave speed vs. strain behavior and the frequency vs. strain behavior is the "S" shape displayed by the former, which is definitely not seen in the latter. In the latter case, the frequency data measured at the last step, at 3 MPa, align well with the frequency data obtained during steps 1 to 2.5 MPa, which is a result that adjusts well to the theory of acoustoelasticity.

Figure 5.15 and Table 5.5 presents the results of β_G obtained from the fundamental torsional frequency of vibration data for each loading/unloading stage and cycle. These are shown by the solid triangles. The unfilled circular markers correspond to the β_G results obtained using the S-wave technique, here shown again to ease comparison between both techniques.

The vibration β_G results, the triangles, vary between -345 and -387, their average is -363.8 and CV of 4.2 %. The data displays a slight increment of β_G (in absolute value) as loading/unloading cycles advance. The most remarkable observation from Figure 5.15 is the great difference of β_G results yielded between techniques. The vibration technique yielded a β_G almost four

Table 5.5: Results of β_G computed from the torsional resonance frequency measurements for each loading/unloading stage of each cycle.

Cycle	Stage	β_G
1	Loading	N/A
1	Unloading	-358.5
2	Loading	-344.8
2	Unloading	-372.2
3	Loading	-353.0
3	Unloading	-387.4
4	Loading	-367.2
4	Unloading	N/A
Average		-363.8
CV (%)		-4.2
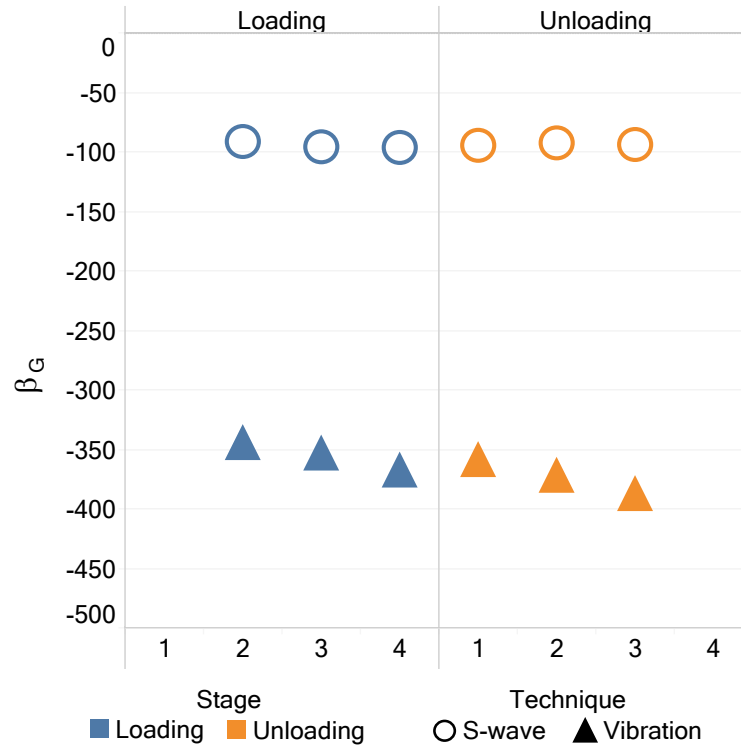
Figure 5.15: Triangular markers showing the results of β_G obtained from torsional vibration measurements among loading/unloading stages of the four cycles of Test 3. Circular markers are β_G data repeated as in Figure 5.12.

times higher than the S-wave technique. This is, of course not explained by the theory of acoustoelasticity, which in fact, predicts equal values of β_G, as demonstrated analytically and numerically in Chapter 3. Such a big difference cannot be justified by minor numerical approximations or minor experimental

deviations from theory. This means that the wave propagation technique is "seeing" the solid less nonlinear than the torsional vibration technique.

5.4. Posing a Nonlinear Viscoelastic Model

One important difference between these techniques is the frequency in which material particles vibrate. In this research's experiments, propagating S-waves make particles vibrate at a range of frequencies centered at 150 kHz, whereas in resonance (fundamental torsional vibration) particles vibrate at 1.6 kHz approximately. This is two orders of magnitude difference between the two dynamic phenomena. If the tested material had indeed a frequency-dependent response to dynamic events, this could be the factor causing the difference between β_G values of both techniques. The use of a nonlinear viscoelastic solid material, instead of a nonlinear elastic material, would be capable of explaining these findings.

Before continuing with the posed description, the reader should note that there exist other possible influencing factors that could affect or even fully explain the observed results. One of these, is the fact that for the NDE characterization, Poisson's ratio was considered constant in order to calculate dynamic G values from dynamic E values; this fact is discussed and can be reasonable neglected. Another influencing factor is the strain range dependence of the frequency of vibration of nonlinear materials [72, 83]; the observed frequency decreases as the dynamic strain range of vibration increases. The dynamic strain ranges of wave propagation are orders of magnitude lower than the vibration, so this fact is potentially an influencing factor. In these tests, vibration was carried out by applying low energy impacts to minimize this effect, but specific tests to actually prove this fact is not affecting were not carried out. With these considerations, the objective of this section is to pose a possible theoretical description which could potentially explain, either fully or partially, the experimental results. It follows a basic and heuristic analysis, which involves taking various hypotheses; thus, the following description does not provide definitive results or conclusions, but it rather opens a very interesting window for further and deeper research.

Figure 5.16 presents a possible viscoelastic model composed of a pair of nonlinear (strain-dependent) springs of elastic moduli $G_v(\varepsilon)$ and $G_a(\varepsilon)$, which model the solid's elasticity, and one damper of constant η_G which models the

103

solid's viscosity. A similar model was considered by Fan et al. [76] to propose a unified description capable of explaining the experimental differences between quasistatic and dynamic elastic moduli of hardened mortar specimens.
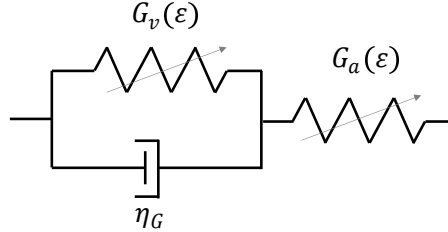
Figure 5.16: Diagram of the three-piece viscoelastic solid model with nonlinear springs.

To be in accordance with the theory developed in this Thesis, let us expand G_a and G_v only to the first power of ε. Thus,

$$G_a(\varepsilon) = G_{a0} + G_{a1}\varepsilon, \tag{5.7}$$

with G_{a0} and G_{a1} being the two strain-independent coefficients that control G_a, and

$$G_v(\varepsilon) = G_{v0} + G_{v1}\varepsilon. \tag{5.8}$$

with G_{v0} and G_{v1} being the two strain-independent coefficients that control G_v.

From the model, we see that for very high loading frequencies the "auxiliary" spring (G_a) will dominate because the damper will prevent the "Voigt" spring (G_v) from affecting. For very low loading frequencies the system will vibrate with an equivalent constant of the two springs in series, because the damper would not affect.

Let us also consider that the nonlinear behavior is activated only when a quasistatic load is applied. Note that we have already adopted this hypothesis in Chapter 3, and Fan et al. [76] also adopt it. Thus, the dynamic behavior is linear, and it is only affected by the quasistatic pre-load which modifies the effective elastic parameters of the springs. Therefore, the system has a different dynamic behavior depending on the pre-load.

Analogously as it occurs in a standard linear viscoelastic solid [85] (see Appendix 1), the constitutive equation of our nonlinear viscoelastic solid is [76]

$$(G_v + G_a)\sigma + \eta_G \frac{\partial \sigma}{\partial t} = \eta_G G_a \frac{\partial \varepsilon}{\partial t} G_v G_a \varepsilon. \tag{5.9}$$

Note that when the pre-load is null ($\varepsilon = 0$), we only need to substitute G_a and G_v by G_{a0} and G_{v0}, respectively, and the model exactly represents the standard linear viscoelastic solid.

In a standard linear viscoelastic solid, the material behaves partially elastic and partially viscous. This behavior is mathematically described by the solid's complex modulus G^*, which corresponds to the ratio of applied stress to observed strain. The existence of non-null viscosity generates a time-lag between stress and strain, which does not exist in a purely elastic solid. This behavior is described by considering

$$G^* = G' + iG'', \tag{5.10}$$

where i is the imaginary unit, G' is the storage modulus and G'' is the loss modulus. The storage modulus of a viscoelastic material can be interpreted as the "part" of the solid capable of allocating elastic energy, and therefore, behaving more elastically. Thus, when we carry out experiments on real material solid bodies, and we estimate the elastic moduli from these experiments, if the material has a slight viscosity, we are actually estimating the storage modulus G'. A deeper analysis of this assertion is given in Appendix 1. On the other hand, the loss modulus represents the viscosity of the material and it is associated to the energy loss during a stress-strain cycle.

For a particular pre-load level ε, the storage modulus G' of our solid is obtained by dividing the harmonic-time-dependent applied stress into the observed strain and taking the real part; thus

$$G' = \frac{G_a G_v (G_a + G_v) + G_a \eta_G^2 \omega^2}{(G_a + G_v)^2 + \eta_G^2 \omega^2}, \tag{5.11}$$

which is again analogous to the storage modulus of a standard linear viscoelastic solid. In equation (5.11), ω corresponds to the angular frequency of the acting stress that forces the material. Thus, we see that G' is frequency dependent, so we would expect to find different values of G' when estimating it from techniques that force the material particles at different frequencies.

When the pre-load is null ($\varepsilon = 0$), $G_a = G_{a0}$ and $G_v = G_{v0}$, thus, equation (5.11) becomes

$$G_0' = \frac{G_{a0}G_{v0}(G_{a0} + G_{v0}) + G_{a0}\eta_G^2\omega^2}{(G_{a0} + G_{v0})^2 + \eta_G^2\omega^2}, \qquad (5.12)$$

which again it becomes equivalent to the standard linear viscoelastic solid model.

We can now use the NDT experiments carried out before the acoustoelastic tests (P and S waves, torsional frequency) and also the quasistatic stress-strain measurements collected during Test 3, to find estimated G_0' values at different frequencies ω. These results are presented in Table 5.6.

Table 5.6: Results of storage moduli G_0' estimated from NDT and quasistatic stress-strain of Test 3 associated to the frequencies in which the material is being forced to vibrate for each testing technique.

	f (Hz)	ω (rad/s)	G_0' (GPa)
Quasistatic	0.0001	0.000628	8.12
Flexural free vibration	1214.2	7629.0	9.54
Torsional free vibration	1689.0	10612.3	9.79
Longitudinal free vibration	2852.2	17920.9	10.00
P-wave 54 kHz	54000	339292	11.81
P-wave 150 kHz	150000	942478	11.91

Note that some of these techniques yield the Young's modulus E, so G values were obtained by considering a Poisson's ratio of 0.18, but it was observed that using a range of potential Poisson's ratios, from 0.15 to 0.22, does not qualitatively change the results as the obtained G_0' stay close. We can now fit equation (5.12) to the experimental results of Table 5.6 and find the best-fit parameters presented in Table 5.7. The best-fit equation and the experimental data are presented in Figure 5.17.

Table 5.7: Parameters G_{a0}, G_{v0}, η_G, result from fitting equation (5.12) to experimental data of table 5.6.

G_{a0}	11.79 Gpa
G_{v0}	28.76 Gpa
η_G	2.87 MPa/(rad/s)

Figure 5.17 shows the behavior of the storage modulus G_0', which is the typical behavior of a standard linear viscoelastic solid. For low frequencies
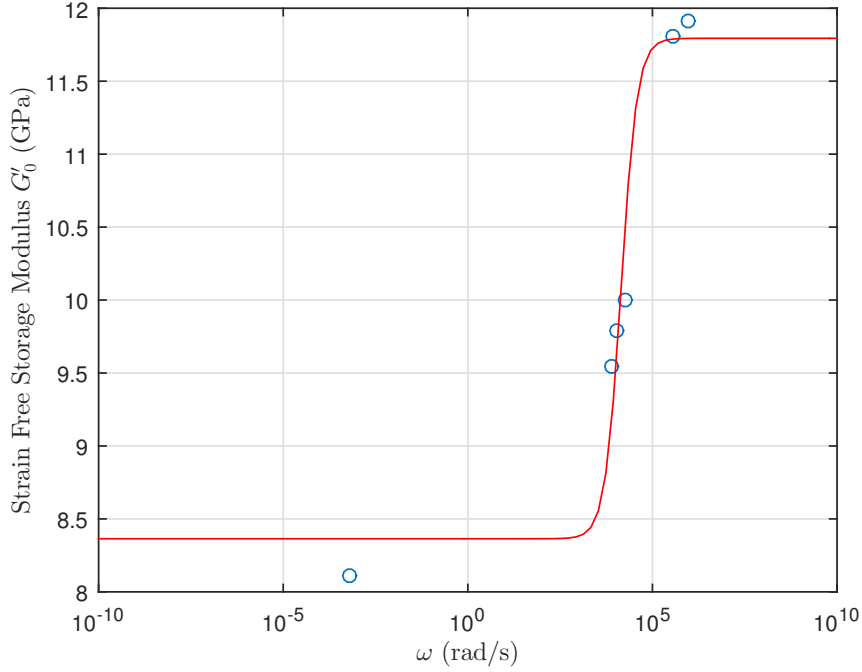
Figure 5.17: Analytical equation (5.12) of storage modulus G'_0 with respect to angular frequency ω, using the best-fit parameters $G_{a0} = 11.79$ GPa, $G_{v0} = 28.76$ GPa and $\eta_G = 2.87$ MPa/(rad/s). Circular markers indicate the experimental results.

it behaves with a certain storage modulus $\cong \frac{G_{a0}G_{v0}}{G_{a0}+G_{v0}}$, almost independent from frequency, but after a certain critical frequency, the system's behavior undergoes a sudden change, where the storage modulus has a high frequency dependency. For even higher frequencies, the system behaves with a high storage modulus $\cong G_{a0}$, and tends to become frequency independent. The critical frequency depends only on the value of η_G.

Consider again equation (5.11). Recall that this equation takes the viscoelastic parameters G_a, G_v and η_G, and the frequency ω in which the material particles are being forced to vibrate, and yields the value of the storage modulus G'. Therefore, because the parameters G_a and G_v depend on the solid's current quasistatic strain ε as per equations (5.7) and (5.8), then G' also depends on the solid's current quasistatic strain. We can easily find this dependency by introducing equations (5.7) and (5.8) into (5.11), which yields a rather complicated expression of strain dependent G' (expression not shown). We can now take that expression and carry out a Taylor expansion of first order, centered in $\varepsilon = 0$, to get an equation of the form

$$G'(\varepsilon) = G'_0 + G'_1 \varepsilon, \tag{5.13}$$

where G'_0 is given in equation (5.12) and G'_1 is an expression that depends on G_{a0}, G_{a1}, G_{v0}, G_{v1}, η_G, and ω (expression not shown). However, note that equation (5.13) has the same form as the definition of β_G in (3.6). Thus, we can actually define a frequency dependent "storage" nonlinear torsional parameter β'_G obtained by calculating

$$\beta'_G = \frac{G'_1}{G'_0}. \tag{5.14}$$

By carrying out the mentioned calculations we obtain

$$\beta'_G = \left(\frac{G_{a1}\eta_G^2\omega^2 + (G_{v0}G_{a1} + G_{v1}G_{a0})(G_{v0} + G_{a0}) + G_{v0}G_{a0}(G_{v1} + G_{a1})}{G_{a0}\eta_G^2\omega^2 + G_{v0}G_{a0}(G_{v0} + G_{a0})} - \frac{2\left[G_{a0}\eta_G^2\omega^2 + G_{v0}G_{a0}(G_{v0} + G_{a0})\right](G_{v0} + G_{a0})(G_{v1} + G_{a1})}{[\eta_G^2\omega^2 + (G_{v0} + G_{a0})^2][G_{a0}\eta_G^2\omega^2 + G_{v0}G_{a0}(G_{v0} + G_{a0})]} \right). \tag{5.15}$$

During Test 3, two very different β_G results were obtained. One of these results was based on S-wave propagation, β_G = -94.8, and another one based on torsional resonance vibration, β_G = -363.8. Moreover, it is possible to use the quasistatic stresses and strains collected during Test 3 to find the "quasistatic" β_E, by fitting a 2nd order polynomial to the experimental data. This calculation yielded β_E = -1687, associated to a very low frequency (quasistatic test tends to zero frequency). In general, the ratio of β_E to β_G is around 1.3 (based on the values of l, m and n obtained by Nogueira and Rens [64], for concrete and for mortar, and also based on Payan et al. [17]). Thus, assuming that relationship holds here too, the "quasi-static" β_G = -1288. These three β_G values are notoriously different, and if the mortar material was purely elastic, these three values should be equal. However, if we consider that the testing specimen was slightly viscous and behaves according to the model proposed in this section, then the β_G results previously obtained are actually β'_G results, which are frequency dependent. Table 5.8 presents the three β'_G at the associated testing frequencies.

Using the already calculated parameters G_{a0}, G_{v0}, and η_G given in Table 5.7, let us find the coefficients G_{v1} and G_{a1} that best-fit equation (5.15) to

Table 5.8: Results β'_G associated to each technique and testing frequency.

	f (Hz)	ω (rad/s)	β'_G
Quasistatic	0.0001	0.000628	-1288
Torsional free vibration	1689.0	10612.3	-364
S wave	150000	942478	-95

the β'_G results presented in Table 5.8. The best-fit analytical curve and the experimental β'_G results are presented in Figure 5.18. The best-fit parameters are

$$G_{v1} = 120 \times 10^3 \text{ GPa},$$

and
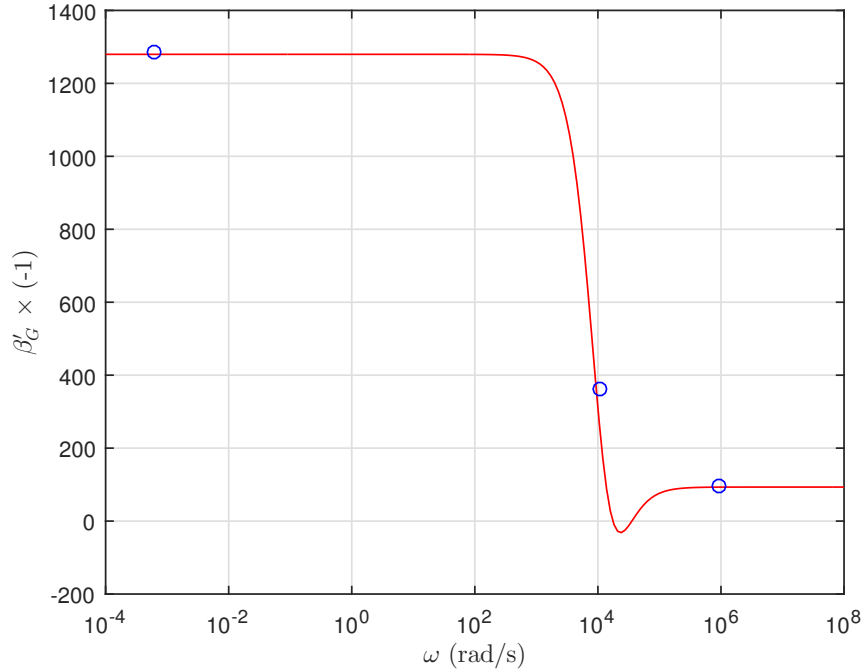
$$G_{a1} = 1100 \text{ GPa}.$$

Figure 5.18: Analytical equation (5.15) of storage nonlinear parameter β'_G with respect to angular frequency ω, using the best-fit parameters $G_{v1} = 120 \times 10^3$ GPa and $G_{a1} = 1100$ GPa. Circular markers indicate the experimental results.

As seen in Figure 5.18, the nonlinear viscoelastic model proposed in this

section predicts higher values of β'_G for low frequencies, such as in quasistatic tests, and lower values of β'_G for higher frequencies, such as in wave propagation tests. For these frequency regions, the model shows a very low frequency dependence of β'_G. For intermediate frequencies, there is high frequency dependence of β'_G. The parameter η_G has almost exclusive control on determining the critical frequency; in other words, different values of η_G produce horizontal shifts on the (red) analytical curve of Figure 5.18. The parameter G_{a1} produces an overall vertical shift of the analytical curve and G_{v1} mainly affects the left branch of the curve by producing vertical shifts.

It is interesting to see that the value η_G was computed during the first fit of G'_0 (equation (5.12)), and when β'_G equation was fit (equation (5.15)) only G_{a1} and G_{v1} were determined to fit the data. Therefore, even though G_{a1} and G_{v1} cannot shift the analytical curve horizontally, the value of β'_G for intermediate frequency falls exactly on the analytical curve. This fact strengthens the proposed model. Finally, it can be seen in Figure 5.18 a minor range of frequencies, around 2.5×10^4 rad/s, in which the analytical curve predicts positive values of β'_G. This would mean that for these frequencies the material would have a softening behavior under uniaxial compression. It is very likely that this finding is actually an artifact of the model and/or mathematical assumptions during the analysis instead of a real physical behavior; specialized tests are needed to confirm or refute this finding.

5.5.   Conclusions

In this chapter, a mortar specimen was tested under uniaxial compression and S-wave speed and torsional frequency of vibration were monitored during the loading test. The general objective was to study the stress (and strain) dependence of S-wave speed and torsional frequency of vibration, in order to advance into the ultimate goal of instrumenting a nondestructive testing technique capable of determining in-situ current stress level of concrete structures. This chapter describes the performance of two different experimental techniques, S-wave propagation and torsional vibration for the characterization of mortar (concrete) nonlinearity based on the theory of acoustoelasticity. The specific objective was to verify the consistency between techniques; in practice, to calculate the nonlinear torsional parameter β_G using each technique and analyze the results, expecting to find similar values of β_G from both techniques.

Based on the experimental data and analysis described in this chapter, the following conclusions can be drawn.

- Uniaxial compressive stresses (and strains) had a repetitive positive correlation with S-wave speed and with torsional frequency of vibration.

- Room temperature variations affected S-wave speed measurements in the same order of magnitude than the variations of S-wave speed due to stress (acoustoelastic). A theoretical and experimental tool was successfully applied to correct the effect of temperature from the S-wave speed measurements.

- When the specimen was submitted to one loading and unloading cycle, and then it was left at rest, the S-wave speed increased and decreased following the loading/unloading, respectively. However, after fully removing the load, the S-wave speed became slightly lower than the initial wave speed, about 0.09 %, which tended to recover in time. After certain period of rest (18 hours in this experiment), the S-wave speed recovered and stayed constant. This behavior is consistent with slow dynamics conditioning/recovery phenomena. In this case, the actuator would be conditioning the material when the quasistatic force was being introduced.

- The S-wave propagation and torsional vibration techniques were used to characterize the mortar's material nonlinearity by calculating the β_G parameter. The former yielded β_G = -94.8, and the latter β_G = -363.8. This high difference was not explained by the theory of acoustoelasticity, which predicted equal β_G values from both techniques. This was an important finding which suggests that, if the theory of acoustoelasticity is used, the material nonlinear parameters are method dependent (possibly due to the frequency difference and/or dynamic strain range difference among methods).

- A simple and heuristic analysis was posed to try to explain the β_G experimental results. The analysis consisted of using a viscoelastic solid material composed of two nonlinear (strain dependent) springs, representing the material's elasticity, and a damper to represent its viscosity. This model allows explaining the slight differences of the dynamic shear moduli (from different nondestructive testing techniques), and it also explains the frequency dependence of the β_G values. Further research is

needed to confirm or refute this last finding.

- Future work involves carrying out specialized tests to confirm or refute the possible frequency dependence of the nonlinear parameters, as well as introducing into the model and tests the effect of the dynamic strain range on the frequencies of vibration.

Chapter 6

Case of Study: Internal pressure monitoring in a post-tensioned containment building using operational vibration

6.1. Introduction

Nuclear power generation requires much attention to safety measurements to contain the nuclear material during service and to finally dispose of its residues. Reinforced and prestressed concrete structures, complemented with other barrier materials, have been the traditional solution to safely contain nuclear material. These critical structures need to follow strict building, testing, and monitoring codes to ensure their correct behavior without imposing a hazard to society and environment. Typical tests required by government regulations and technical codes are based on internal pressure tests, where structural integrity and fluid-tightness are assessed [86–88]. These quality assurance tests take several days, time in which the structure is not operational; thus, planned and unplanned maintenance/testing stops are avoided as much

as possible [89].

In addition to the regular need for monitoring nuclear concrete structures, there is an increasing concern due to the natural aging of concrete material and the fact that plants are reaching the end of their service lives [89–92]. These have prompted several research projects focused on studying many aspects of structural condition assessment and monitoring in order to extend power plants' service life [93–97]. The goals are to assess the current state of materials and structures, and to anticipate future issues by developing new monitoring techniques, as robust, efficient, and economical as possible.

Nondestructive testing (NDT) and structural health monitoring (SHM) are testing techniques where the structure under study remains fully unaffected. The collected data can then be used to assess the structure's intrinsic properties, for example, to back-calculate material elastic properties, detect deterioration onset or mechanical stress variations [57, 98–100]. This is a key condition, highly valued to assess nuclear concrete structures.

Most of the existing research on NDT and SHM applied to nuclear power plant concrete structures focus on assessing concrete's quality, damage detection, and durability [101–104]. There are also multiple reports focusing on general monitoring for long-term mechanical properties characterization, creep, stress determination, and prestressing tendon losses [89, 105–110].

The specific objective of this research is to develop an NDT/SHM technique capable of monitoring internal pressure changes and pressure leakage of nuclear concrete containments, externally (no need of accessing into the structure's interior), and without affecting the regular structure's service. Such a technique would be useful as a complementary measurement during regularly planned tightness tests. Moreover, it can become fundamental in case of an accident or for long-term structural monitoring, for example for nuclear waste containment, where no other equipment might be available and the access to the interior is impeded or highly unsafe. Another important application is when the pre-installed (embedded) sensors, such as strain gauges, thermocouples, etc. have malfunctioned [111]. There are several studies where nuclear concrete structures are subjected to internal pressure and various monitoring techniques are analyzed [107, 111–113] but none of them purse directly our goal. In particular, Hu et al. [114] studied the mechanical and material behavior of a post-tensioned nuclear power concrete container under internal pressure using a finite element method (FEM) model. They considered similar

affecting factors as ours but their goal, to estimate the structure's ultimate pressure capacity, was different from ours.

To pursue our goal, we have carried out experiments on a mock-up structure: a post-tensioned concrete double-walled-cylindrical nuclear containment. The structure was gradually subjected to internal pressure during the experiment in several steps which took 75 hours. Throughout that time, we collected acceleration signals with two sensors attached to the outer side of the inner structure. With these, we measured the dynamic response of the structure under different pressure levels. This type of testing technique falls within the field of "output-only dynamic analysis" or "operational modal analysis", where the structure's dynamic features are computed from the natural vibrations occurring while the structure is operational; i.e. there is no specific dynamic input prompting the vibration phenomena. Output-only dynamic analysis is a growing field of study [115–118] whose main advantage is its simpler experimental implementation, which does not require the use of bulky vibrational apparatus, it is more economical and does not affect the structure's regular operations. Choi et al. [118] carried out experiments in an operating nuclear containment structure based on operational modal analysis techniques. They were able to identify frequencies of vibration and extract material/structural properties, but they did not focus on monitoring pressure or mechanical stresses variations.

This research's main originality is the monitoring of a nuclear containment decennial test and not the method per se. An easy testing setup is successfully employed, based on an output-only experimental system, which does not require bulky instruments nor to embed sensors within the structure. This is the first study focused on studying the relationship between modal frequencies of vibration and internal pressure of a large-size nuclear-containing structure, using output-only methods. This research demonstrates the existence of clear positive correlations between the structure's natural frequencies of vibration and internal pressure. These are promising findings towards developing a robust NDE/SHM technique capable of monitoring internal pressure variation in complex nuclear concrete containments.

6.2.   Materials and Methods

6.2.1.   Vercors: The Reinforced Concrete Container

Vercors inner structure consists of a post-tensioned reinforced concrete cylindrical structure of 15 m diameter, capped with a dome-shaped lid. Walls are 0.40 m thick, and 30 m tall. The structure is founded on a concrete floor 0.70 m thick. Vercors mock-up is a physical model at 1/3 scale of a real nuclear confinement building. An outer independent structure protects Vercors mock-up from external effects, such as wind and drastic temperature variations. Figure 6.1 presents a photograph of Vercors mock-up from the outside.

Figure 6.1: Photograph of Vercors building mock-up.

Concrete quality control was carried out during its construction using standard cured companion cylinders. These were tested on day 28 after casting and provided results of density, compressive strength [119] and modulus of elasticity [120]. Table 6.1 contains the material characterization results, corresponding to the average properties of each concrete batch.

Vercors mock-up comprised a total of 250 t of reinforcing steel, 50 t of post-tensioning steel and 2500 m^3 of concrete.

6.2.2.   Experiment Procedure

The experiment consisted of gradually injecting/releasing air into the containment to increase/decrease its internal pressure. Air pressure and temperature were measured inside the container. The protocol involved six stages,

Table 6.1: Characterization of concrete using standard cured concrete cylinders at day 28 after casting.

Average compressive strength	$f_{cm,28}$	48 MPa
Characteristic compressive strength[1]	$f_{ck,28}$	42 MPa
Average static Young's modulus	$E_{cm,28}$	37 GPa
Average density	ρ	2201 kg/m3

(1) $f_{ck,28}$ is the "characteristic" strength which corresponds to the 5th percentile of the strength data.

starting at stage 1 at ambient pressure (0 bar). The internal pressure was increased during stages 2 and 4, and decreased during stage 6, at a rate of approximately 0.2 bar/hour. Stage 3 began when pressure reached 2 bar; at this point, the pump was turned off for 5 hours approximately, until resuming pressure-increase of stage 4. Upon reaching approximately 4 bar, the pump was turned off for 12 hours, until starting the pressure-decrease of stage 6, in which the valve was opened Figure 6.2 contains the pressure data measured during the entire experiment.
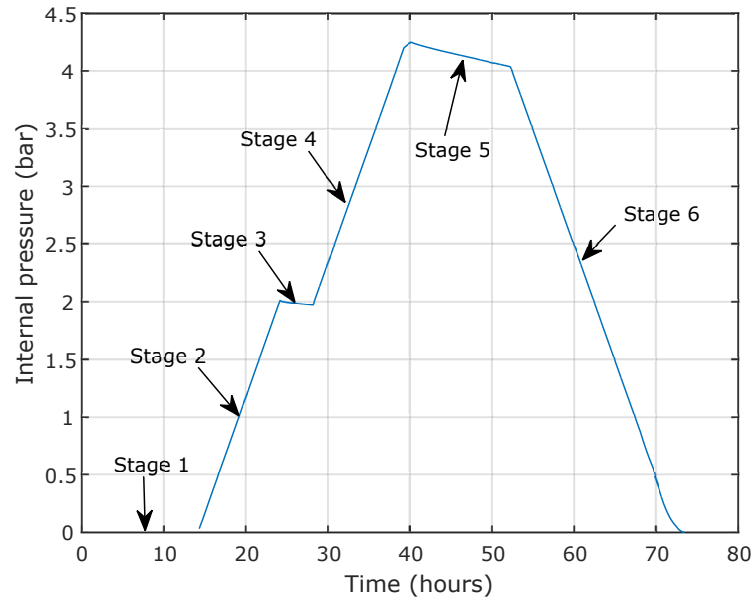
Figure 6.2: Internal pressure over time during the experiment.

Two accelerometers model PCB 352A24, with nominal sensitivity of 100 mV/g, were utilized during the experiment. Defining the most appropriate number of sensors is a trade-off situation. While using more sensors would improve results, particularly to determine the modal shapes, more costly and

117

cumbersome experimental setups would be required. Because the goal of this research was to focus on the frequencies of vibration and not the shapes, it was decided to maximize the experimental robustness and easiness, so only two sensors were employed. These two accelerometers were attached to the outer face of the structure, both at level 7.5 m and at angles 0 and 36° from the structure's angular reference (the bigger circular through-wall hole -hatch area- is centered at $\sim 265^o$). Acceleration signals were acquired every 5 minutes. Each of these time-domain signals consisted of 100.002 amplitude data points sampled at 20 kHz. Thus, every collected time-domain signal lasted approximately 5 seconds. This signal duration time was selected to guarantee stationarity and to allow obtaining good quality frequency-domain signals.

6.2.3. Signal Processing

Signal processing was carried out in four steps, signal validation, pre-processing, processing, and post-processing.

Signal validation

Signal validation consisted of inspecting every raw signal in time and frequency domains, to keep only the signals with useful information. As explained below, some stages of the experiment did not yield vibrational responses that could be distinguished from noise. To this end, the total energy of each signal was calculated by numerically integrating the squared signals in time. An "energy threshold" of 8×10^{-6} V^2.s was selected for accelerometer 1 and 11×10^{-6} V^2.s for accelerometer 2. Signals with lower energy than the threshold were discarded during this step. Other signals that exceeded the threshold but had sudden spikes in time-domain, and showed no clear vibrational behavior in frequency domain, were also discarded during this step, as recommended by Brincker and Ventura [115].

Pre-processing

Pre-processing consisted of filtering time-domain signals using a Butterworth bandpass filter of 4th order with cutoff frequencies of 3 Hz and 2000 Hz.

Processing

The "processing" step consisted of computing the frequency spectra. The following processing was applied to each time-domain signal obtained with each sensor. First, a 2-seconds-long, Blackman moving window was applied, with

75% overlap. Thus, each 5-seconds-long time domain signal produced seven 2-second-long time domain windowed signals. The election of the type and length of window was done based on preliminary analyses which supported those features. Each of the windowed signals were padded with 300000 zeros at their tails. The amplitude-frequency spectrum of each of these seven windowed-padded signals was computed using the FFT algorithm. Then, the seven frequency spectra were averaged, obtaining one frequency spectrum per time domain signal, for each sensor. The corresponding pairs of frequency spectra, associated to each accelerometer were averaged, obtaining one single frequency spectra associated to every time of signal collection. Finally, pressure measurements and collected amplitude-frequency spectra were synchronized.

Postprocessing

The "post-processing" consisted of finding the frequencies of vibration of the modes of interest. This task was carried out selecting the peaks within the frequency spectra. The reader should note that there exist more sophisticated methods for frequency tracking [121, 122]. Nevertheless, given the short duration of the signals (5 seconds) with respect to the rate of pressure change (0.2 bar/hour), the pressure can be considered constant during the signal, so it sufficed using the traditional peak picking from the frequency spectra.

6.2.4. Computation of Frequency vs. Pressure Correlation

Prior to computing the correlations of frequency vs. pressure it was necessary to define which frequencies of vibration should be used. Preliminary analyses detected frequency peaks recurrently observed during the entire test, while some others, were clearly observed in some signals but disappeared in many others. Therefore, we selected frequency peaks at around 30 Hz, 68 Hz, 93 Hz, 105 Hz, 142 Hz, and 192 Hz, to compute the regression, which appear recurrently in most of the signals. Figure 6.3 shows the frequency spectrum computed for one of the signals collected during stage 6.

In Figure 6.3 we see that there are other peaks besides the ones selected for the analysis. These were either not recurring throughout the experiment, meaning that they did not appear in many signals, or it could be the case of two peaks being very close so their trends could not be successfully distinguished independently, so these were not included to compute the frequency
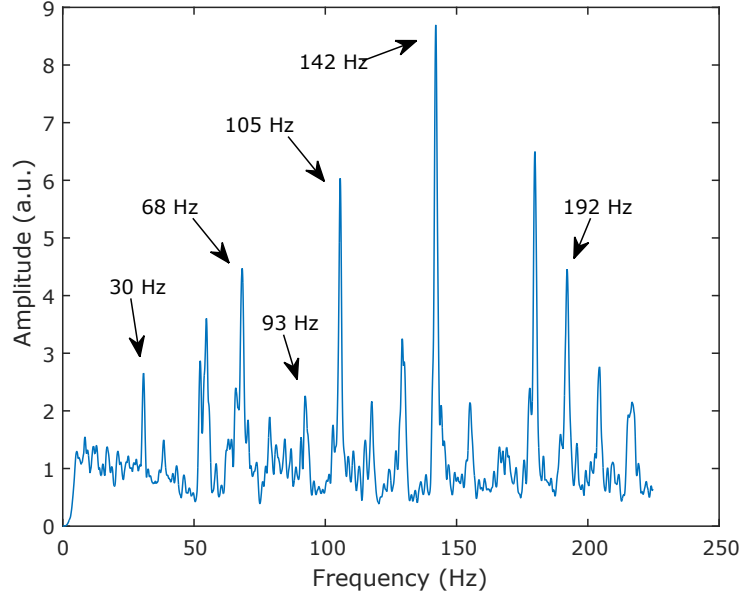
Figure 6.3: Frequency spectrum of signal collected during stage 6. Arrows indicate the frequency peaks used for the analysis.

vs. pressure correlations.

Frequency vs. pressure correlations were carried out using the modes corresponding to the mentioned frequency peaks. The final step consisted of computing the correlations between measured frequency peaks and measured pressure. The procedure for correlation calculation consisted of fitting the data using a multi-variable linear regression, where each nominal frequency mode $(f_{30}, f_{68}, f_{93}, f_{105}, f_{142}, f_{192})$ corresponded to each independent variable. An inconvenient of using multi-variable correlation is that the size of the dataset tends to decrease as more independent variables (frequency peaks) are considered in the model, so there are less signals where all six peaks have been identified. This issue was overcome by implementing a variant, as explained below. The multi-variable mathematical model is

$$P = a_0 + a_{1,30}f_{30} + a_{1,68}f_{68} + a_{1,93}f_{93} + a_{1,105}f_{105} + a_{1,142}f_{142} + a_{1,192}f_{192}. \quad (6.1)$$

This mathematical model would require that in order to fit the data, the six peaks must have been identified. Those signals where one or more peaks had not been identified would not be considered in the model. Thus, the data size used for the fit would become drastically reduced -due to the randomness

120

of the experimental procedure, many of the signals lack of clear identification of one frequency peak-. To overcome this inconvenient, a variant was implemented, where every possible multi-variable linear regression between pressure and any number of existing frequency peaks were computed. Thus, if a certain signal contains all frequency peaks except for one frequency peak, the pressure prediction would be obtained using the multi-variable model that does not include that missing frequency-peak value. To limit the extent of possible results, the developed algorithm was set so that only one or two of the six frequency peaks could be missing. The correlations procedures were all carried out using the frequency-peaks and pressure data obtained during stage 6 (pressure descending).

Once the pressure vs. frequency-peaks correlation was computed, i.e. the regression coefficients of equation (6.1) were calculated, we can then use that correlation to find the "predicted pressure" based on the frequency data. The goodness of the correlation was evaluated by calculating the adjusted coefficient of determination R^2, and the standard error of the regression, S, defined as the average of the distances between the regression's predictions and the actual observations [123]. The value S is useful because it has the same units as the predicted magnitude, in this case, bar, and approximately 95 % of the predictions are within $+/-1.96 \times S$ from the observed magnitude.

6.3. Experimental Results and Discussion

During signal validation, it was observed that signals corresponding to stages 1, 3, and 5 contained no useful information and their total energy was lower than the energy threshold. These stages corresponded to time periods where the pump was off (and the valve was closed), where any oscillatory behavior could not be distinguished from noise. Using operational vibrations, the vertical resolution of the acquisition device is set to warrant a good SNR in such a configuration. So outside operational conditions, i.e. during the time periods where the pump was off (and the valve was closed), without the possibility to remotely change the vertical resolution, there was no sufficient vibration amplitude to perform our analyses. From the 1093 acquired signals with each sensor, only around 520 of them (of each sensor) were validated. Those signals not validated were excluded from further analyses.

6.3.1. Frequency-peak Results with Respect to Internal Pressure

Figure 6.4 contains the obtained frequencies with respect to measured internal pressures during stages 2, 4 and 6.
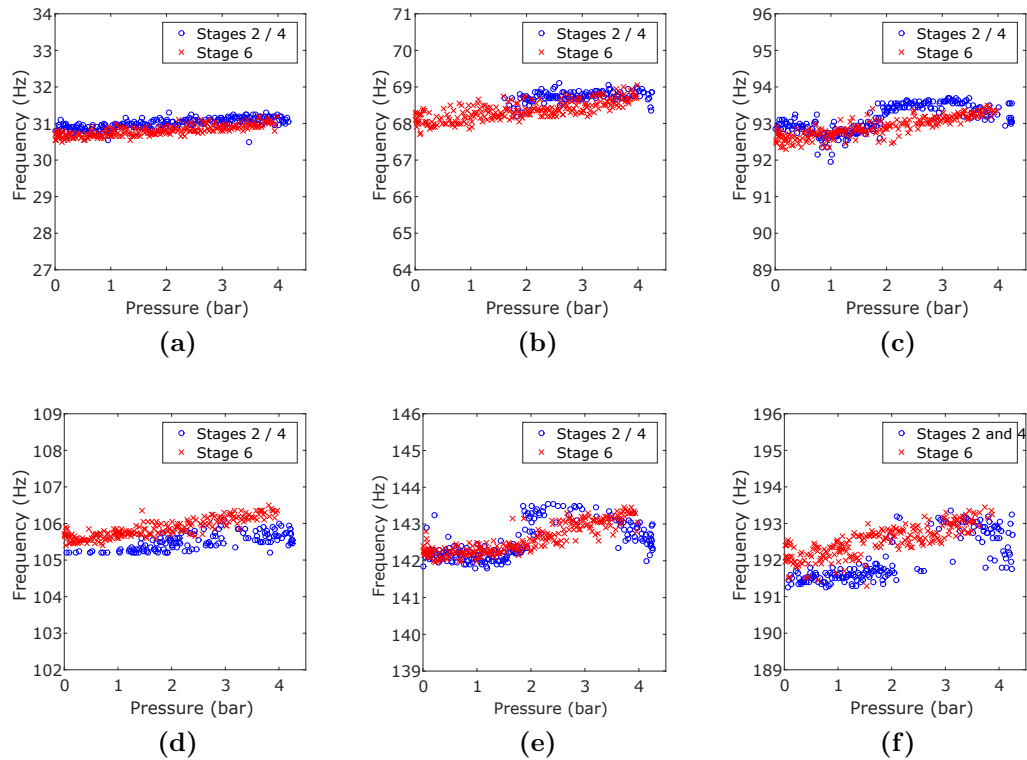
Figure 6.4: Frequency-peak results vs. internal pressure results during stages 2 and 4 (blue circles) and stage 6 (red crosses), for nominal frequency peaks (a) f_{30}, (b) f_{68}, (c) f_{93}, (d) f_{105}, (e) f_{142}, (f) f_{192}.

The frequency peak results presented in Figure 6.4 show consistent behavior during stage 6, depicting a positive correlation between frequency and internal pressure. This trend has been previously observed by Piacsek et al. [124] in aluminum spherical containers. It should be noted that the total frequency change, between pressure 0 to 4 bar, is very small, in the order of 0.5 to 1 Hz, depending on the mode. The spectral frequency resolution of 0.05 Hz (see subsection 2.3) allows observation of meaningful trends between internal pressure and frequency for such frequency variations. Results of stages 2 and 4 are not as consistent as in stage 6; some of the frequency peaks show odd behavior, without a clear trend, for example for the modes at ∼142 Hz and

~192 Hz (Figures 6.4e and 6.4f). However, a hysteretic behavior becomes apparent. We do not know the precise causes leading to such behavior. While this hysteretic behavior could be the result of impaired damage to the structure upon the pressurization, it can be also attributed (in some cases) to the difficulty of tracking the frequency modes during the experiment which frequently appear coupled. Further tests are needed to elucidate the nature of these apparently odd observations. Also, there are several pressure levels in which frequency peaks could not be detected, for example, the frequency peak f_{68} (Fig. 6.4b) was not detected at pressures from 0 to 2 bar, i.e. during stage 2. However, f_{30} (Fig. 6.4a) shows consistent results for all stages 2, 4 and 6. For these reasons, correlation curves were derived from data of stage 6, and specific physical behavior hypotheses are discussed based on peak f_{30} results.

6.3.2. Frequency vs. Pressure Correlation Curves

The multi-variable linear regression coefficients associated to equation (6.1), with all six frequency peaks being identified, one frequency peak missing, and two frequency peaks missing, are presented in Tables 6.2, 6.3 and 6.4, respectively.

Table 6.2: Multi-variable linear regression coefficients between frequency and pressure when all six frequency peaks are clearly distinguished.

missing f_{Nom}	a_0	$a_{1,30}$	$a_{1,68}$	$a_{1,93}$	$a_{1,105}$	$a_{1,142}$	$a_{1,192}$
none	-451.8	1.05	0.515	1.088	1.078	0.437	0.564

Table 6.3: Multi-variable linear regression coefficients between frequency and pressure when one of the six frequency peaks has not been identified.

missing f_{Nom}	a_0	$a_{1,30}$	$a_{1,68}$	$a_{1,93}$	$a_{1,105}$	$a_{1,142}$	$a_{1,192}$
30	-458.2	-	0.614	1.104	1.183	0.604	0.541
68	-451.6	1.175	-	1.133	1.178	0.54	0.573
93	-449.7	1.024	0.543	-	1.334	0.753	0.697
105	-426.4	1.414	0.701	1.268	-	0.61	0.686
142	-452	1.224	0.612	1.226	1.243	-	0.669
192	-422.6	1.351	0.59	1.148	1.202	0.761	-

Figure 6.5 presents the graph of predicted pressure with respect to measured pressure, where the unity line is superimposed. There it is observed that the scattered data is close to the unity line, which indicates qualitatively that

Table 6.4: Multi-variable linear regression coefficients between frequency and pressure when two of the six frequency peaks have not been identified.

1st missing f_{Nom}	2nd missing f_{Nom}	a_0	$a_{1,30}$	$a_{1,68}$	$a_{1,93}$	$a_{1,105}$	$a_{1,142}$	$a_{1,192}$
30	68	-460.2	-	-	1.174	1.298	0.787	0.537
30	93	-454.1	-	0.672		1.434	0.935	0.649
30	105	-436.2	-	0.866	1.311	-	0.823	0.726
30	142	-463.9	-	0.754	1.339	1.459	-	0.703
30	192	-434.5	-	0.678	1.13	1.424	0.941	-
68	93	-449.3	1.185	-	-	1.482	0.849	0.71
68	105	-422.7	1.69	-	1.384	-	-	0.715
68	142	-450.9	1.394	-	1.326	1.424	0.745	0.706
68	192	-420	1.464	-	1.2	1.308	0.889	-
93	105	-419.9	1.465	0.818	-	-	1.012	0.916
93	142	-449.3	1.274	0.729	-	1.784	-	0.899
93	192	-414	1.571	0.648	-	1.544	1.127	-
105	142	-420	1.73	0.868	1.557	-	-	0.855
105	192	-386.6	1.795	0.777	1.52	-	0.974	-
142	192	-411.2	1.786	0.789	1.466	1.585	-	-

the prediction is good. The residual analysis is graphically presented in Figure 6.5b, which shows no clear trend, depicting another good feature of the correlation. The adjusted coefficient of determination was equal to 0.90. Figure 6.5c is another representation of the residuals (errors between the predicted pressure and measured pressure) expressed as a histogram.

In the histogram of Figure 6.5c, we observe that almost all pressure errors are within -1 to 1 bar. The histogram is Gaussian-shaped, with approximately null mean error and a standard deviation of 0.37 bar; around 67 % of the predicted pressures have an error between -0.37 and 0.37 bar. The standard error of the regression (S) is another parameter helpful to characterize the goodness of the regression; it tells how "wrong" the model is on average, in units of pressure. This regression has an S value of 0.29 bar. Thus, approximately 95 % of the measured pressures fall within $+/-$ 0.57 bar ($1.96 \times S$) from the regression line [123].
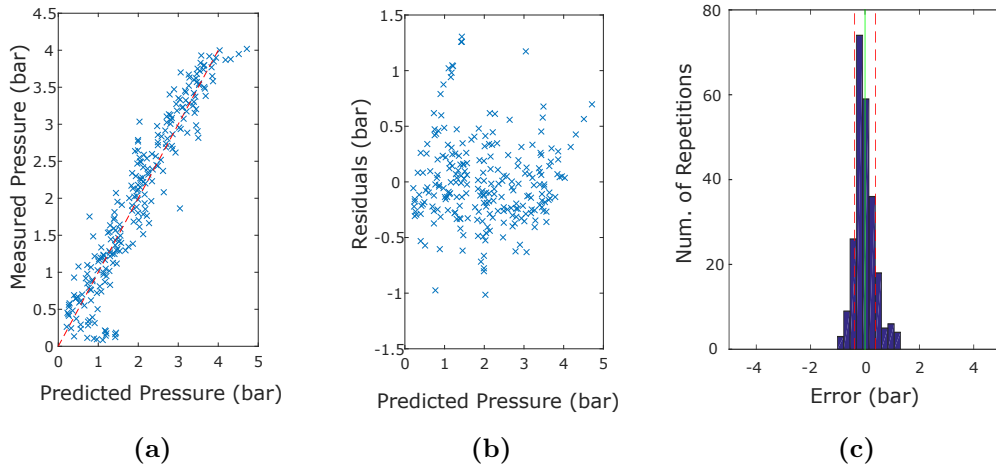
Figure 6.5: (a) Predicted pressure (P_{pred}) vs. experimentally measured pressure (P_{exp}) superimposed with the red dashed unity line, (b) residuals analysis, and (c) error (residuals) histogram with continuous green line and red dashed lines indicating mean error and standard deviation.

6.3.3. Pressure Leakage Estimation

Experimental results presented in the previous section show a clear correlation between internal pressure and frequency, where frequency increases with increasing internal pressure. This trend is very clear during stage 6 (pressure decreasing) for all six frequencies of vibration (modes) analyzed here, but not as clear during stages 2 and 4 (pressure increasing). Theoretically, we could use this correlation to identify pressure drops due to leakages off the container. In Figure 6.2, we see a clear pressure drop due to leakage during stage 5 when the pump is off. There, pressure drops from approximately 4.25 bar (last pressure reading of stage 4) to 4.05 bar (first pressure reading of stage 6). This 0.20 bar drop is within the variability (0.37 bar of standard deviation) of our correlation computed using all six frequency modes so we may not expect to obtain an accurate predicted pressure drop estimation. We note that correlation was intended to represent the global frequency vs. pressure relationship throughout the full range of internal pressures. On the other hand, we do see in Figure 6.4a that the mode f_{30} is particularly interesting because it showed higher consistency than the other modes when comparing behaviors of the stages 2/4 and 6. For these reasons we study the possibility of using the mode f_{30} to identify internal pressure leakage. Thus, here we focus the analysis on the leakage by comparing the f_{30} results at the end of stage 4 against those at

125

the beginning of stage 6.

First, we use the pressure and f_{30} frequency data collected during stage 6 to compute a linear correlation expressed by the equation

$$P_{pred} = (f_{30} - 30.50 \text{ Hz}) \times 6.236 \frac{\text{bar}}{\text{Hz}}. \tag{6.2}$$

Equation (6.2) can be used to calculate the "predicted pressure" P_{pred} from a measured frequency peak f_{30}. Because of the intrinsic variability of the method, we ought to select a set of signals and work with the set's mean value. Now we select a set of nine signals collected during the end of stage 4, associated to pressures higher than 4 bar, and a set of five signals collected at the beginning of stage 6 associated to pressures between 3.90 and 4.00 bar.

Figure 6.6a shows the measured internal pressure during time, where the superimposed red circles indicate the times in which time-domain signals were acquired. The end of stage 4 and beginning of stage 6 are indicated with the names: zone S4 and zone S6, respectively. The very end of stage 4, indicated as zone S4-tip, corresponds to a small period of time where the pump starts to turn off; it provided poor results, so those signals were discarded. The mean values of measured pressures in zones S4 and S6 are 4.10 and 4.01 bar, respectively, indicated with green bars in Figure 6.6c.

In Figure 6.6b we show the groups of frequency peaks that characterize S4 and S6, respectively. We see that the frequency population of S4 is slightly higher than the frequency population of S6, which is consistent with having a higher pressure in zone S4 than in S6. In Figure 6.6c we present the results of predicted pressure P_{pred} obtained by applying equation (6.2) to the mentioned frequency data sets. Again, we see an analogous difference between populations as in Figure 6.6b. The mean values of the predicted pressures in zones S4 and S6 are 3.91 and 2.87 bar, respectively. These are shown with black bars in Figure 6.6c. A t-test of hypothesis on the means of the two predicted pressure distributions was carried out to prove that these mean values are different with a 95 % confidence. However, the predicted pressure difference, 1.04 bar, is ten times higher than the actual difference of pressure means, 0.1 bar. It is highly likely that the structural behavior during stage 6, where pressure is decreasing, is different than during stage 4, where pressure is increasing. However, this effect is in fact an indication of pressure leakage so it could actually be used for this purpose.
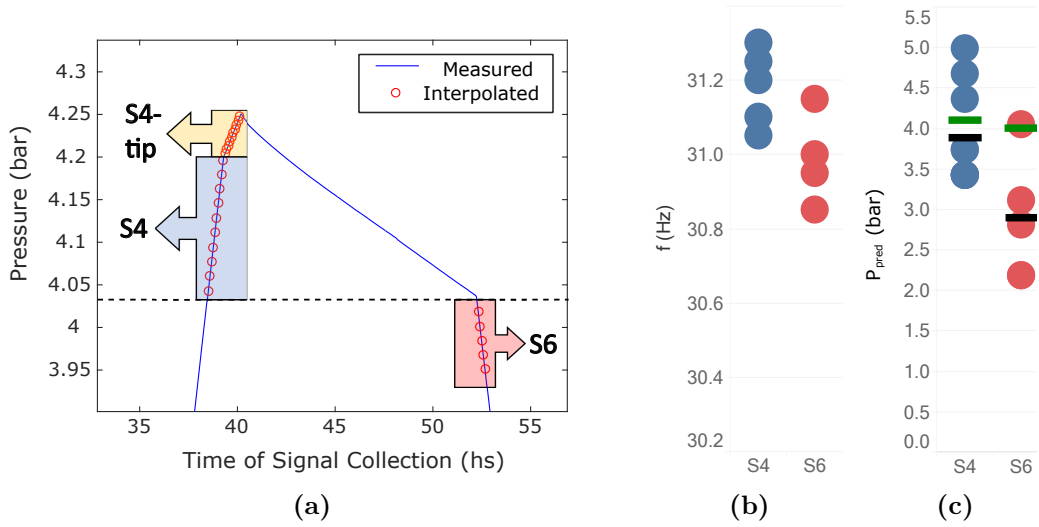
Figure 6.6: (a) Pressure measurements in time. Blue line corresponds to the pressure data measured with a manometer, red circles are the interpolated pressures vs. time in which signals were collected, zones S4, S4-tip and S6 indicate the three groups of signals. (b) Frequency values of mode f_{30} of zones S4 and S6, respectively. (c) Blue and red circles are the predicted pressures at zones S4 and S6, respectively; green bars are the mean values of the pressure readings at zones S4 and S6, and black bars are the mean values of the predicted pressures at zones S4 and S6.

From this analysis we conclude that the regression made to match the frequency data over a large range of pressures, from 0 to 4 bar, does not have enough resolution to accurately quantify the amount of pressure leakage during stage 5 (with the pump off). To assess the problem of pressure leakage, we should monitor the frequency variations during the leakage per se. However, this was not possible during our experiment because no useful data was acquired during stage 5, while the pump was off. To overcome this problem, we should employ sensors with higher sensitivity or rely on a different dynamic input, so we could follow the frequencies of vibration while leakage is occurring.

6.4.   Physical Behavior Discussion

In this section we use the f_{30} mode to investigate and discuss possible underlying physical behaviors that may explain the experimental results. The reader should note that this section is a shallow discussion of potential causes explaining our experimental findings, and we do not draw definitive conclusions. For instance, we note that material-parameter or modal-shapes could

127

no be extracted by fitting our data into a numerical model. The goal of this section is therefore to aid other engineers, other researchers, and even to ourselves, from a "lesson learned" standpoint, to face new problems of structural health monitoring of complex civil infrastructure.

6.4.1. Estimation of Basic Material Parameters

To investigate the experimental findings from a physical standpoint we used a finite element method (FEM) model using the software COMSOL Multiphysics. The first step required defining the basic material parameters, density, Young's modulus and Poisson's ratio to feed the model. Because the collected data was not enough to invert the elastic problem to allow finding all three basic material parameters, we decided to estimate density and Poisson's ratio using engineering criteria and only invert the problem to find Young's modulus.

The structure's mean density was estimated from applying a weighted average of the concrete's density and steel's density, where the amounts of these were known, as mentioned previously in the Materials and Methods section. The Poisson's ratio was 0.20 [23]. Young's modulus was found by matching the FEM model frequency of vibration of mode f_{30} to the experimental frequency with null internal pressure; in other words, the structure's concrete's Young's modulus was that one in which the FEM model produced a frequency of vibration of the f_{30} mode at 30.50 Hz.

Table 6.5 presents the basic material parameters utilized for the FEM model analysis.

Table 6.5: Density (ρ_{RC}), Young's modulus (E_{RC}) and Poisson's ratio (ν_{RC}) of the reinforced concrete material used for the FEM model.

ρ_{RC} kg/m^3	E_{RC} GPa	ν_{RC}
2287.5	49.8	0.2

With the available data we cannot be fully certain that we have selected the correct mode of vibration to match the FEM model and experimental frequencies. However, Lott [125] studied this same structure using a different technique based on wave propagation phenomena, two years before our experiments, and determined this same modal shape vibrating at 27 Hz, very close to the frequency of vibration result we observed; moreover, the obtained struc-

ture's Young's modulus E_{RC} is consistent with the amounts of the constituent materials (steel, concrete and post-tensioning steel), their elastic characteristics and the structure's age.

6.4.2.   Linear and Nonlinear Effects

In the FEM model the lower face of the concrete floor was restrained from displacing and rotating. The internal pressure was applied onto the inner faces of walls, ceiling and floor. A linear-elastic material was considered, using the parameters presented in Table 6.5, and geometric nonlinearity was enabled. Figure 6.7 contains an image of the FEM model geometry and the resulting mode-shape associated to f_{30} at null internal pressure.

The internal pressure was increased between 0 and 4 bar in steps of 1 bar by doing a parametric study in COMSOL. The FEM model and experimental results of f_{30} frequency variation with respect to internal pressure are presented in Figure 6.8.

In Figure 6.8a we see that even though the experiment yielded only one distinct frequency mode near 30 Hz, the FEM model produced three modes around that frequency. The frequencies of vibration of these three modes, as well as the experimental frequency, increase with increasing internal pressure. This frequency vs. pressure relationship was previously seen by Piacsek et al. [124] in a thin-wall aluminum container; they founded their results based on the effect of geometric nonlinearity: the increase of walls' in-plane tension affects the vibration phenomena by increasing the frequency of vibration, such as it occurs in strings under tension. In Figure 6.8, the FEM model mode with the highest frequency is associated to a torsional vibration mode, and the other two with a flexural-type mode as depicted in Figures 6.7b and Fig. 6.7c. These latter modes do not yield the same frequency because of the small non-symmetric structure's geometric features. It is noted that as pressure increases the three modes tend to couple, producing a more complex problem in which frequency vs. pressure relationship becomes highly nonlinear during a limited range of pressures. This phenomenon occurs because not all modes are equally affected by pressure increments.

For the inversion problem of the Young's modulus explained in Section 4, we decided to match the average of the two flexural modes to the experimental frequency; thus, at zero pressure we see in Figure 6.8a the two frequencies of
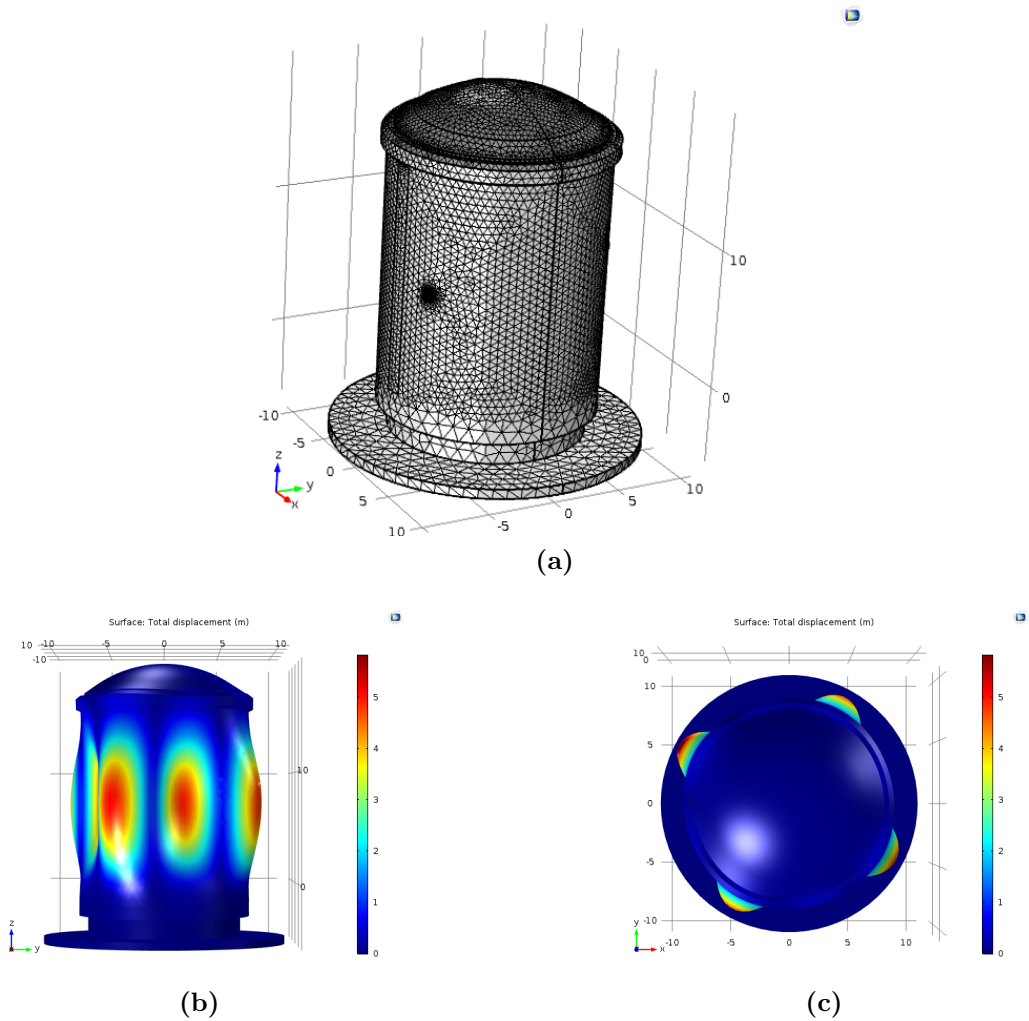
Figure 6.7: Image of the FEM model of Vercors (a) geometry and f_{30} mode of vibration shape at null internal pressure observed from (b) front view and (c) top view.

each flexural mode, starting at 30.47 Hz and 30.54 Hz, where the experimental frequency, 30.50 Hz, is their median value. Still analyzing Figure 6.8a, as pressure increases both the experimental frequency and the FEM model frequency results increase. The frequency increments in the FEM model, where the material has a linear constitutive relationship, could be associated with the geometric nonlinearity activated by the applied pressure. However, we see that the experimental frequency increases twice as much as the FEM model flexural frequencies. This additional frequency increment cannot be explained, not even by accepting that our assumed linear-elastic material parameters of Table 6.5 are not perfectly correct. Some physical causes that could explain
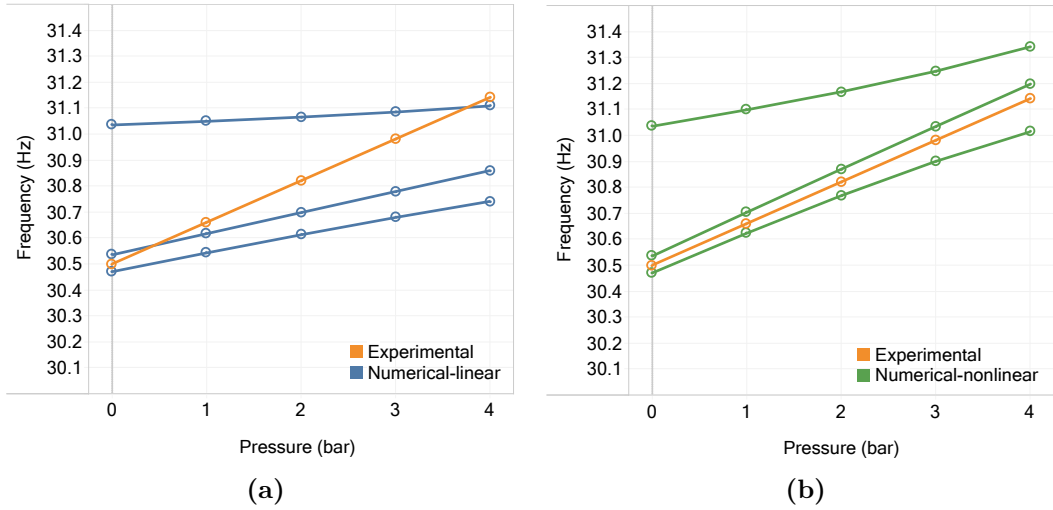
Figure 6.8: Experimental and FEM model (numerical) results of f_{30} frequency variation with respect to internal pressure P. The numerical results include three modes around 30 Hz. Subfigure (a) corresponds to a linear-elastic material and (b) for a elastic slightly nonlinear material with softening.

this discrepancy are: (1) the existence of undetected modes coupled with the experimental f_{30} mode, (2) concrete material behaving elastically but with softening nonlinearity as internal pressure increases, (3) pressure-dependent boundary conditions, or (4) structural stiffening effect due to the compressed air.

Even though we do not have enough information to elucidate which ones of these four hypotheses are actually affecting the results and how much is their influence, we do show that a slight material softening nonlinearity (in addition to the geometric nonlinearity) yields results compatible with the experimental f_{30} behavior. Note that this effect opposes the typical material stiffening observed in plain concrete (not post-tensioned) under compression -acoustoelastic effect [16, 17, 64, 70] and findings presented in Chapters 3, 4 and 5 of this Thesis- which could be explained by stating that microcracks get closed as compression increases, so the material behaves stiffer at higher compression levels (as long as compression remains below ∼30 % of concrete compressive strength [17]). If this was the dominant mechanism, increasing internal pressure should decompress concrete and open the microcracks, and therefore reduce its stiffness and its frequency of vibration. But results show the opposite trend: frequency increases as internal pressure increases, implying therefore a softening behavior. The existence of this softening behavior

could be justified because of the post-tensioning force, which is compressing the concrete material to stress levels in which slight softening nonlinearity is likely to occur [23, 27]. Thus, we ran the same FEM model but considering a Murnaghan material with third-order elastic constants $l = +3000$ GPa, $m = +2000$ GPa and $n = +1000$ GPa. The f_{30} frequency vs. pressure results are presented in Figure 6.8b. In that figure, we see that the FEM model flexural frequency curves and the experimental curve have a very similar behavior. It should be noted that this apparent consistency does not prove that this is the actual physical cause governing the problem, but it is useful to guide further research. In any event, these results confirm that the geometric nonlinearity alone does not render a full explanation for the observed behavior; nonlinear elastic behavior should also be considered.

6.5.   Conclusions

This study shows the feasibility to monitor the internal pressure of a post-tensioned concrete containment mock-up (1/3 scale) during a decennial safety review simulation using operational ambient vibrations. It was possible to monitor pressure changes by monitoring the structure's vibration frequency shifts using a reduced number of accelerometers (two) attached to the outer side of the inner wall of the structure and without measuring the dynamic input. This technique falls in the field of the "output-only dynamic analysis" or "operational modal analysis" which is gaining importance for characterization and structural health monitoring of large structures. The frequency peaks associated to different modes of vibration tend to increase as pressure increases and vice versa. A new variant of a multi-variable correlation was computed to fit the frequencies vs. pressure data. This correlation, which had an adjusted coefficient of determination R^2 equal to 0.9 and a standard error S of 0.29 bar, allows to robustly predict the internal pressure. A pressure leakage was clearly identified during pressure bearings. However, the correlation computed over a large pressure range (4 bar) was not capable of successfully predicting the absolute pressure leakage (0.1 bar). An FEM model of the structure was built and the frequency vs. pressure was studied focusing on the mode around 30 Hz. The FEM model frequency increased with increasing pressure, probably due to the geometric nonlinearity induced by the internal pressure. However, the experimental frequency results of the mode around 30 Hz increased twice

as much as the results yielded by the FEM model with a linear-elastic material. An FEM model including nonlinear material with softening yielded results that are in good agreement with the experimental data, but this may not be the only cause. Other possible causes which may explain this discrepancy include mode coupling, variable boundary conditions, and/or effect of compressed air. Further research is needed to elucidate which ones of these are significant. For future work, we will test higher sensitivity sensors in order to detect structural vibration during pressure bearing stages, we will use special sensors to measure the lower frequency modes and an increased number of sensors to improve identification of the modal shapes.

Chapter 7

Conclusions

Previous research has proved the existence of minor stiffening in concrete elements under uniaxial compression, quantified by a 1 to 2 % increment of the dynamic Young's modulus of a specimen uniaxially compressed from 0 strain to 100×10^{-6}. This behavior makes mechanical wave speed increase with increasing compressions. This is the acoustoelastic effect, and has been investigated for stress determination in concrete specimens, so far, with limited success. The use of resonance vibration techniques for acoustoelastic characterization of concrete has been recently studied by other researchers and showed promising results.

This research's main objective was to study the use of resonance vibration for acoustoelastic characterization of concrete materials. This represented the first step to fulfill the challenging goal of developing a nondestructive testing method capable of accurately estimating the current stress present in concrete structural members. The development of such a technique would benefit the field of civil engineering in many aspects, such as to monitor prestress and post-tension losses, for structural condition assessment and as a quality control method.

To pursue these goals, this research included theoretical analytical and numerical studies developed specifically to assess the problem in question, which included the use of the Theory of Finite Elasticity applied to nonlinear materials, wave propagation and vibration phenomena. An experimental procedure based on torsional vibration was developed and tested in order to characterize concrete nonlinearity, which constitutes the key parameter potentially capable of being used for current stress determination in structural concrete mem-

bers. This is the first study to deeply analyze analytically, numerically and experimentally, the use of a torsional vibration technique for acoustoelastic characterization of concrete elements. The proposed technique was compared against the traditional technique for acoustoelastic characterization, based on wave propagation. Experimental results yielded by both techniques did not perfectly match, as they should if the theory of acoustoelasticity was fully applicable; thus, a viscoelastic model was posed which showed good fit with the experimental results. Finally, a case study was presented, where frequency-of-vibration tracking was used to monitor the internal pressure in a real size nuclear containment concrete structure.

Based on the developments and analyses carried out throughout this research, the following specific conclusions can be drawn.

- Material nonlinear parameters β_E and β_G were defined based on 1-dimensional constitutive equations of elongated prisms (bars). These nonlinear material parameters are capable of modeling concrete's acoustoelastic effect, i.e. the frequency of vibration increments observed when elongated prisms are uniaxially compressed. The nonlinear parameter β_G corresponds to the rate of change of the shear modulus G_ε with respect to uniaxial strain, and it can be characterized using torsional vibration nondestructive testing techniques.

- The problem of a nonlinear solid elongated prism under quasistatic compression was studied using finite elasticity, and the expressions of β_G and β_E were analytically calculated in terms of the third order elastic constants l, m and n. These expressions were successfully verified numerically by building an FEM model in COMSOL using a nonlinear Murnaghan solid (nonlinear hyperelastic material).

- It was demonstrated analytically that monitoring the variation of the wave speed mode 21 (V_{21}) with respect to stress should be sufficient to calculate the nonlinear parameter β_G, which would simplify the experimental setup as measuring l, m and n requires monitoring three distinct modes. Also, this provided a readily method to compare the use of a torsional technique for acoustoelastic characterization, which yields β_G experimentally, to the traditional acoustoelastic techniques based on wave propagation, which experimentally yield wave speed increments.

- A virtual test was run using MATLAB, involving a column of known

135

properties and "unknown" applied quasistatic uniaxial stress (and strain). Measurements were simulated by considering typical variability, and equations were applied to "estimate" (calculate) the "current applied strain". A Monte Carlo analysis showed that the resulted "current applied strain" was very sensitive to the rest of the involved material properties and measurements, implying that small measurement deviations may yield large deviations of estimated current strain and stress. In the proposed virtual test, the assumed standard deviations of the virtual measurements were 0.1, 0.1 Hz and 0.1×10^{-6} for β_G, frequency and strain, respectively. With these assumed uncertainties, the standard error of the estimated applied strain was 10%, meaning that approximately 68% of the obtained applied strains from the Monte Carlo analysis had errors of 10% or less. Such a good accomplishment can be truly expected only if the experimental measurements are sufficiently accurate, or their associated errors otherwise reduced, for example by increasing the number of measurements and tests.

■ In general terms, in order to use torsional vibration for acoustoelastic characterization, the effect of non-uniform torsion and geometric nonlinearity should be considered as they are coupled with the acoustoelastic effect. However, they can be neglected for any structural member of solid-section sufficiently elongated, which are essentially all typical beam-or-column-like concrete elements. In these cases, the Saint-Venant torsion term dominates, so the problem can be successfully modeled using the strain-dependent shear modulus G_ε. This fact was verified numerically using an FEM model in COMSOL. The torsional frequency of vibration of the tested concrete and mortar prisms (Chapter 4 and 5, respectively) showed a positive correlation with the applied uniaxial quasi-static compression strain and stress level, as predicted by the theory of acoustoelasticity. The influence of the nonlinear material stiffening dominated over that of geometric nonlinearity (P-δ effect) and possible material softening.

■ Boundary conditions could be affected by the applied external load, which influence the system's dynamic behavior, yielding results where this effect is coupled to the acoustoelastic effect. Therefore, the effect of load-dependent boundary conditions must be somehow characterized and decoupled from the results in order to characterize material nonlin-

ear parameters. This was successfully carried out by considering load-dependent springs (neoprene pads) attached to both ends of the concrete elements, and carrying out specific tests to characterize these springs. In this Thesis' experiments, if the effect of boundary conditions had not been considered, the nonlinear material parameter β_G would have been overestimated by approximately 20 %. Other experimental configurations or field characteristics may increase or reduce the effect of changing boundary conditions on the acoustoelastic effect; this characteristic must be assessed for each situation.

- In the first experimental campaign (Chapter 4), the initial loading cycle of all concrete prisms yielded β_G values around -95, that were clearly lower (in absolute value) than those obtained from subsequent loading/unloading cycles on the same sample, which averaged -125. Thus, competing stiffening (acoustoelastic) and softening (damage, material slow dynamics conditioning or other) effects occurred during the first loading cycle. The obtained values of β_G neglecting the first load cycle were consistent among the range of concrete mixtures considered, even though other mixture parameters such as Young's modulus and compressive strength varied significantly. The values of β_G obtained numerically from previously published results, which used vibration-based techniques, are of the same order of magnitude as the ones computed in Chapter 4. Results of β_G computed from previous studies based on wave propagation techniques yielded values of β_G lower than those computed here, which motivated the studies presented in Chapter 5.

- Experiments presented in Chapter 5 involved monitoring both torsional frequency of vibration and S-wave speed (V_{21}) in mortar prisms, during several loading/unloading cycles. Room temperature variations affected S-wave speed measurements in the same order of magnitude than the variations of S-wave speed due to stress (acoustoelastic). A theoretical and experimental tool was successfully applied to correct the effect of temperature from the S-wave speed measurements.

- Experiments presented in Chapter 5 showed that when the mortar specimen was submitted to one loading and unloading cycle, and then it was left at rest, the S-wave speed increased and decreased following the loading/unloading, respectively, with a positive correlation, as per the acoustoelastic effect. However, after fully removing the load, the S-wave speed

became slightly lower than the initial wave speed, about 0.09 %, which then tended to recover in time. After a certain period of rest (18 hours in this experiment), the S-wave speed recovered and stayed constant. This behavior is consistent with slow dynamics conditioning/recovery phenomena. In this case, the actuator could have been conditioning the material when the quasistatic force was being introduced. It is therefore presumed that this effect, and not damaging, occasioned the softening behavior detected in the first loading cycles of the experimental campaign presented in chapter 4 (which yielded lower β_G results than subsequent loading/unloading cycles).

- In Chapter 5, the S-wave propagation and torsional vibration techniques were used simultaneously to characterize the mortar's material nonlinearity by calculating the β_G parameter, individually with each technique. The former yielded an average β_G = -94.8, and the latter β_G = -363.8. This significant difference is not explained by the theory of acoustoelasticity, which predicts equal β_G values from both techniques. This is an important finding which suggests that, if the theory of acoustoelasticty is used, the material nonlinear parameters may be considered to be method-dependent (possibly frequency-dependent and/or dynamic strain range-dependent).

- A simple and heuristic analysis was posed in Chapter 5 to try to explain the difference in the β_G experimental results. The analysis consisted of using a viscoelastic solid material composed of two nonlinear (strain dependent) springs, representing the material's elasticity, and a damper to represent its viscosity. This model allowed explaining the slight differences of the dynamic shear moduli (from different nondestructive testing techniques), and it also explained the frequency dependence of the β_G values. Further research is needed to confirm or refute this finding, as well as the study of other potential influencing factors, as the dynamic strain range (amplitudes) of the testing method.

- The case study presented in Chapter 6 showed the feasibility to monitor the internal pressure of a post-tensioned concrete containment mockup (1/3 scale) during a decennial safety review simulation using operational ambient vibrations. It was possible to monitor pressure changes by monitoring the structure's vibration frequency shifts using a reduced number of accelerometers (two) without measuring the dynamic input. The

frequency peaks associated to different modes of vibration tended to increase as pressure increased and vice versa. An FEM model of the structure was built and the frequency vs. pressure was studied focusing on the mode around 30 Hz. In the FEM model, frequency increased with increasing pressure due to the geometric nonlinearity induced by the internal pressure. However, the experimental frequency results of the mode around 30 Hz increased twice as much as the results yielded by the FEM model with a linear-elastic material. An FEM model including nonlinear material with softening yielded results that were in good agreement with the experimental data, but this may not be the only cause. Other possible causes which may explain this discrepancy include mode coupling, variable boundary conditions, and/or effect of compressed air. Further research is needed to elucidate which ones of these are significant.

The following topics remain open to investigate in the future.

- In this investigation, experimental frequency-of-vibration shifts of the first fundamental torsional mode were fit into analytical equations to characterize material nonlinear parameter β_G. In a hypothetical test, if β_G is already known, the same procedure could be used for current stress estimation, but large errors are expected if measurements are not sufficiently accurate. To improve the estimation's accuracy, the use of many modes of vibration could be employed. Experimental results of frequency and modal shape shifts could be fed into an FEM model in order to back calculate elastic properties and currently applied stress.
- A blind test using an already characterized concrete sample should be run in order to assess the accuracy of the theoretical and experimental procedures for current stress determination developed in this Thesis.
- This Thesis showed the existence of a frequency-dependence of the nonlinear elastic material parameters. This fact could be explained by considering the material slightly viscoelastic, but other influencing factors could partially or fully control this effect. Specialized tests should be carried out to prove this hypothesis. Until this fact is elucidated, we would not be fully certain of the nature controlling concrete material nonlinearity and care should be taken if different nondestructive testing techniques are mixed for acoustoelastic characterization or stress estimation.

139

- Once the experimental observations carried out in mortar and plain concrete are in agreement with the posed theory, and current stress can be successfully determined using a nondestructive testing method, the behavior of reinforced concrete should be investigated.

- Perfect uniaxial stressed elements are scarcely encountered. Structural members are frequently submitted to at least slight bending moments. The effect of bending on acoustoelastic measurements should be therefore investigated.

Bibliography

[1] BBC News. *Brazil dam: Startling pictures of Brumadinho collapse.* 2019. URL: https://www.bbc.com/news/world-latin-america-47096011.

[2] Souza Jr. PA de. "Open data could have helped us learn from another mining dam disaster". In: *Science Data* 6.54 (2019).

[3] BBC News. *Italy bridge collapse: What we know so far.* 2018. URL: https://www.bbc.com/news/world-europe-45193452.

[4] NPR. *10 Years After Bridge Collpase, America Is Still Crumbling.* 2017. URL: https://www.npr.org/2017/08/01/540669701/10-years-after-bridge-collapse-america-is-still-crumbling.

[5] 228 AC. *ACI 228.2R-13: Report on Nondestructive Test Methods for Evaluation of Concrete in Structures.* Farmington Hills: ACI, 2013.

[6] 201 AC. *ACI 201.1R-08: Guide for Conducting Visual Inspection of Concrete in Service.* Farmington Hills: ACI, 2008.

[7] Naik TR, Malhotra VM, and Popovics JS. "The Ultrasonic Pulse Velocity Method". In: *Handbook on Nondestructive Testing of Concrete.* Ed. by Malhotra VM and Carino NJ. New York: CRC Press LLC, 2004.

[8] ASTM C597. "Standard Test Method for Pulse Velocity Through Concrete - 16". In: *ASTM Standard* (2016).

[9] ASTM C215. "Standard Test Method for Fundamental Transverse , Longitudinal , and Torsional Resonant Frequencies of Concrete Specimens". In: *ASTM Standard* (2008), pp. 1–7.

[10] ASTM E837. "Standard Test Method For Determining Residual Stresses By The Hole-Drilling Strain-Gage Method". In: *ASTM Standard* (2013). URL: www.astm.org,.

[11] James M and Lu J. *Handbook of measurement of residual stresses*. Lilburn: The Fairmont Press, 1996.

[12] Mehrkar-Asl S. "Direct Measurement of Stresses in Concrete Structures". PhD thesis. University of Surrey, 1988.

[13] Owens A. "In-situ stress determination used in structural assessment of concrete structures". In: *Strain* 29.4 (1993), pp. 115–124. ISSN: 14751305. DOI: 10.1111/j.1475-1305.1993.tb00848.x.

[14] Hughes D and Kelly J. "Second-order elastic deformations of solids". In: *Physical Review* 92.5 (1953).

[15] Kandil FA, Lord JD, Fry A, and Grant PV. "A review of residual stress measurement methods - A guide to technical selection". In: *NPL Materials Centre* Report MATC(A)04 (2001), pp. 1–42.

[16] Chaix JF, Lillamand I, Ploix MA, Garnier V, and Corneloup G. "Study of acoustoelasticity behavior of concrete material under uniaxial compression". In: *Journal of the Acoustical Society of America* June (2008). DOI: 10.1121/1.2935671.

[17] Payan C, Garnier V, Moysan J, and Johnson PA. "Determination of third order elastic constants in a complex solid applying coda wave interferometry". In: *Applied Physics Letters* 94.011904 (2009). DOI: 10.1063/1.3064129.

[18] Shokouhi P, Zoëga A, Wiggenhauser H, and Fischer G. "Surface Wave Velocity-Stress Relationship in Uniaxially Loaded Concrete". In: *ACI Materials Journal* (2012), pp. 141–148.

[19] Virgin N. L. *Vibration of Axially Loaded Structures*. Cambdridge: Cambridge University Press, 2007.

[20] Lundqvist P and Ryden N. "International Acoustoelastic effects on the resonance frequencies of prestressed concrete beams — Short-term measurements". In: *NDT and E International* 50 (2012), pp. 36–41.

[21] Cetrangolo G. "Ensayos no destructivos aplicados a la caracterización de estructuras y materiales de construcción". PhD thesis. Tesis Doctoral, Facultad de Ingeniería Udelar, Uruguay, 2017.

[22] Mindess S, Young JF, and Darwin D. *Concrete*. 2nd. Pearson Education, Inc., 2003.

[23] Garcia Meseguer A, Arroyo Portero JC, and Moran Cabrera F. *Jimenez Montoya hormigon armado*. 15th ed. Barcelona: Gustavo Gill, SL, 2009, p. 679. ISBN: 9788425225222.

[24] ASTM C469. "Standard Test Method for Static Modulus of Elasticity and Poisson's Ratio of Concrete in Compression". In: *ASTM Standard* (2014), pp. 1–5. DOI: 10.1520/C0469. URL: www.astm.org,.

[25] ASTM C39. "Standard Test Method for Compressive Strength of Cylindrical Concrete Specimens". In: *ASTM Standard* (2012), pp. 1–7.

[26] 318 AC. *ACI 318-14: Building Code Requirements for Structural Concrete*. Farmington Hills: ACI, 2014.

[27] British Standards Institute. *BS EN 1992-1-1:2004: Eurocode 2: Design of Concrete Structures - Part 1-1: General rules and rules for buildings*. London: British Standards Institute, 1992.

[28] Shokouhi P, Zoega A, and Wiggenhauser H. "Nondestructive Investigation of Stress-Induced Damage in Concrete". In: *Advances in Civil Engineering* 2010 (2010). DOI: 10.1155/2010/740189.

[29] Guz AN and Makhort FG. "The physical fundamentals of the ultrasonic nondestructive stress analysis of solids". In: *International Applied Mechanics* 36.9 (2000), pp. 1119–1149.

[30] Delsanto P. "Acoustoelasticity and Applications". In: *Evaluation of Materials and Structures by Quantitative Ultrasonics*. Springer-Verlag Wien, 1993, pp. 301–315.

[31] Bergman RH and Shahbender RA. "Effect of statically applied stresses on the velocity of propagation of ultrasonic waves". In: *Journal of Applied Physics* 29.12 (1958). DOI: 10.1063/1.1723035.

[32] Cantrell JH and Salama K. "Acoustoelastic characterisation of materials". In: *International Materials Reviews* 36.4 (1991).

[33] Rivière J et al. "Frequency, pressure, and strain dependence of nonlinear elasticity in Berea Sandstone". In: *Geophysical Research Letters* 43.7 (2016), pp. 3226–3236. ISSN: 19448007.

[34] Rose JL. *Ultrasonic Waves in Solid Media*. Cambridge University Press, 2004.

[35] Graff KF. *Wave Motion in Elastic Solids*. Dover Publications, 1991.

[36] Castaneda DI. "New Field Testing Procedure for Measuring Residual Stress". Master's Thesis. University of Illinois at Urbana-Champaign, 2010.

[37] Mehrkar-Asl S. "Concrete Stress-relief Coring: Theory and Application". In: *Proceeding of FIP Symposium 1996*. London: Post-tensioned Concrete Structures, 1996, pp. 569–576.

[38] Dabli A, Bambole A, and Bajoria K. "Evaluation of In-Place Stress in Concrete by Incremental Hole Drilling". In: *ACI Materials Journal* 117 (2020), pp. 27–36.

[39] Parivallal S, Ravisankar K, Nagamani K, and Kesavan K. "Core-drilling technique for in-situ stress evaluation in concrete structures". In: *Experimental Techniques* 35.4 (2011), pp. 29–34. ISSN: 07328818. DOI: 10.1111/j.1747-1567.2010.00622.x.

[40] Castaneda DI, Henschen JD, and Lange DA. "Field test method for residual stress in plain concrete pavements and structures". In: *Journal of Testing and Evaluation* 42.3 (2013). ISSN: 00903973. DOI: 10.1520/JTE20130108.

[41] Lee J, Kim EJ, Gwon S, Cho S, and Sim SH. "Uniaxial static stress estimation for concrete structures using digital image correlation". In: *Sensors (Switzerland)* 19.2 (2019), pp. 1–10. ISSN: 14248220. DOI: 10.3390/s19020319.

[42] Krautkramer J and Krautkramer H. *Ultrasonic Testing of Materials*. 4th. Springer-Verlag Berlin Heidelberg GmbH, 1990, pp. 1–224.

[43] Ewins D. *Modal Testing: Theory and Practice*. Letchworth, Herts. SG6 3BE, England: Research Studies Press LTD, 1986.

[44] Meirovitch L. *Fundamentals of Vibration*. Thomas Casson, 2001.

[45] Hesameddin K, Ifranoglu A, and Hacker T. "Effective Viscous Damping Ratio in Seismic Response of Reinforced Concrete Structures". In: *6th International Conference on Advances in Experimental Structural Engineering*. Urbana-Champaign, 2015.

[46] Gere JM and Goodno BJ. *Mechanics of Materials*. 7th. Cengage Learning, 2009.

[47]   Meirovitch L. *Principles and Techniques of Vibrations*. Englewood Cliffs, New York: Prentice Hall, 1997.

[48]   Majkut L. "Free and forced vibrations of timoshenko beams described by single difference equation". In: *Journal of Theoretical and Applied Mechanics* 47.1 (2009), pp. 193–210.

[49]   Murnaghan T. *Finite Deformation of an Elastc Solid*. New York, USA: John Wiley and Sons, Inc., 1951.

[50]   Bray DE. "Ultrasonics". In: *Practical Residual Stress Measurement Methods*. John Wiley and Sons, Ltd., 2013. Chap. 10.

[51]   Bach F and Askegaard V. "General stress-velocity expressions in acoustoelasticity". In: *Experimental Mechanics* 19.2 (1979), pp. 69–75.

[52]   Bittner J. "The Stress State Identification of Critical Steel Bridge Components using Nonlinear Acoustics". PhD thesis. University of Illinnois at Chicago, 2012.

[53]   Crecraft D. "The measurement of applied and residual stresses in metals using US waves.pdf". In: *Journal of Sound and Vibration* 5.1 (1967), pp. 173–192.

[54]   Castellano A, Fraddosio A, Marzano S, and Daniele Piccioni M. "Some advancements in the ultrasonic evaluation of initial stress states by the analysis of the acoustoelastic effect". In: *Procedia Engineering* 199 (2017), pp. 1519–1526.

[55]   Ankay B and Zhang C. "Acoustoelastic evaluation of ultra-high performance concretes". In: *AIP Conference Proceedings* 2102.May (2019).

[56]   Bompan KF and Haach VG. "Ultrasonic tests in the evaluation of the stress level in concrete prisms based on the acoustoelasticity". In: *Construction and Building Materials* 162 (2018), pp. 740–750.

[57]   Hafiz A and Schumacher T. "Monitoring of Stresses in Concrete Using Ultrasonic Coda Wave Comparison Technique". In: *Journal of Nondestructive Evaluation* 37.4 (2018), pp. 1–13.

[58]   Jiang H, Zhang J, and Jiang R. "Stress Evaluation for Rocks and Structural Concrete Members through Ultrasonic Wave Analysis : Review". In: *Journal of Materials in Civil Engineering* 29.10 (2017), pp. 1–10.

[59] Larose E and Hall S. "Monitoring stress related velocity variation in concrete with a 2x10-5 relative resolution using diffuse ultrasound (L)". In: *Journal of the Acoustical Society of America* 125.4 (2009), pp. 1853–1856.

[60] Lillamand I, Chaix JF, Ploix MA, and Garnier V. "Acoustoelastic effect in concrete material under uni-axial compressive loading". In: *NDT and E International* 43 (2010), pp. 655–660.

[61] Lin J, Zhang C, and Liu X. "Theoretical and experimental study on measurement technology for acousto-elastic stress in concrete". In: *Electronic Journal of Geotechnical Engineering* 19 E (2014), pp. 1135–1155.

[62] Lin J, Zhao MJ, and Wu D. "Method for non-destructively measuring working stress of concrete". In: *Electronic Journal of Geotechnical Engineering* 19 C (2014), pp. 657–666.

[63] Nogueira CL and Rens KL. "Effect of Acoustoelasticity on Ultrasonic Pulses and Damage of Concrete under Tensile Stresses". In: *ACI Materials Journal* 115.3 (2018), pp. 381–392.

[64] Nogueira CL and Rens KL. "Acoustoelastic Response of Concrete Under Uniaxial Compression". In: *ACI Materials Journal* 116.3 (2019), pp. 21–33.

[65] Chen A and Schumacher T. "Estimation of in-situ stresses in concrete members using polarized ultrasonic shear waves". In: *AIP Conference Proceedings* 1581 33 (2014), pp. 903–908.

[66] Winkler KW and McGowan L. "Nonlinear acoustoelastic constants of dry and saturated rocks". In: *Journal of Geophysical Research: Solid Earth* 109.10 (2004), pp. 1–9.

[67] Zhang Y et al. "Study of stress-induced velocity variation in concrete under direct tensile force and monitoring of the damage level by using thermally-compensated Coda Wave Interferometry". In: *Ultrasonics* 52.8 (2012), pp. 1038–1045.

[68] Zhang J, Han B, Xie HB, Zhu L, Zheng G, and Wang W. "Correlation between coda wave and stresses in uni-axial compression concrete". In: *Applied Sciences* 8.9 (2018), pp. 1–19.

[69] Spalvier A. "Acoustoelastic effects of surface waves in concrete subjectedd to compressive and bending stresses". Master's Thesis. University of Illinois at Urbana-Champaign, 2015.

[70] Spalvier A, Bittner J, Evani SK, and Popovics JS. "The stress-induced surface wave velocity variations in concrete". In: *QNDE 2016 - AIP Conference Proceedings*. Vol. 1806. American Institute of Physics, 2017, pp. 080010–1 – 080010–8.

[71] Otrovsky LA and Johnson PA. "Dynamic nonlinear elasticity in geomaterials". In: *Revista del Nuovo Cimento* 24.7 (2001), pp. 1–46.

[72] Guyer RA and Johnson PA. *Nonlinear mesoscopic elasticity: the complex behaviour of a granular media including rocks and soil*. Wiley-VCH Verlag GmbH & Co. KGaA, 2009.

[73] Jhang K. "Nonlinear ultrasonic techniques for nondestructive assessment of micro damage in material: a review". In: *Precision Engineering and Manufacturing* 10 (2009), pp. 123–135.

[74] Meo M, Polimeno U, and Zumpano G. "Detecting damage in composite material using nonlinear elastic wave spectroscopy method". In: *Applied Composite Materials* 15 (2008), pp. 115–126.

[75] Lima W de and Hamilton M. "Finite-amplitude waves in isotropic elastic plate". In: *Journal of Sound and Vibration* 265 (2003), pp. 819–839.

[76] Fan LF, Wong LN, and Ma GW. "Experimental investigation and modeling of viscoelastic behavior of concrete". In: *Construction and Building Materials* 48 (2013), pp. 814–821.

[77] Mashinsky EI. "Differences between static and dynamic elastic moduli of rocks: Physical causes". In: *Russian Geology and Geophysics* 44.9 (2003), pp. 953–959.

[78] Eiras JN, Vu QA, Lott M, Payá J, Garnier V, and Payan C. "Dynamic acousto-elastic test using continuous probe wave and transient vibration to investigate material nonlinearity". In: *Ultrasonics* 69 (2016), pp. 29–37.

[79] Bittner J. "Understanding and predicting transient material behaviors associated with mechanical resonance in cementitious composites". PhD Thesis. University of Illinois at Urbana-Champaign, 20019.

[80] Shokouhi P, Rivière J, Le Bas PY, and Ulrich TJ. "Nonlinear Acoustic Testing for Concrete Materials Evaluation". In: *Materials Evaluation* 75.1 (2017), pp. 84–93.

[81] Abeele KVD and Sutin A. "Nonlinear Elastic Wave Spectroscopy (NEWS) Techniques to Discern Material Damage , Part I : Nonlinear Wave ..." In: *Research in Nondestructive Evaluation* 12 (2000), pp. 17–30.

[82] 2013a AC. "Standard Practie for Making and Curing Concrete Test Specimens in the Laboratory". In: *ASTM Standard* (2013), pp. 1–9.

[83] Eiras JN, Monzó J, Payá J, Kundu T, and Popovics JS. "Non-classical nonlinear feature extraction from standard resonance vibration data for damage detection". In: *The Journal of the Acoustical Society of America* 135.2 (2014), EL82–EL87.

[84] Bittner JA and Popovics JS. "Direct imaging of moisture effects during slow dynamic nonlinearity". In: *Applied Physics Letters* 114.2 (2019).

[85] Kolsky H. *Stress Waves in Solids*. New York: Dover, 1963.

[86] AFCEN. *RCC-CW Recueil de Conception et de Construction – Civil Works*. Paris, France, 2015.

[87] ASME. *ASME Code for Concrete Containments - Section III - Division 2*. New York, USA, 2010.

[88] Courtois A and Clauzon T. "Tests and Monitoring for Pwr Containment : an Introduction To Afcen Rcc-Cw Code". In: *Structural Mechanics in Reactor Technology*. 2015.

[89] Lundqvist P. *Instrumentation and monitoring of concrete structures in nuclear power plants*. Tech. rep. Energiforsk, 2016, p. 26. URL: http://www.energiforsk.se.

[90] Naus DJ. *Concrete component aging and its significance relative to life extension of nuclear power plants*. Tech. rep. OAK Ridge National Laboratory, 1986. URL: http://www.osti.gov/energycitations/product.biblio.jsp?osti%7B%5C_%7Did=5124169.

[91] Stevens G and Long E. *Materials Reliability Program: Electric Power Research Institute (EPRI) Review of the Japanese Nuclear Operators' (JNOs') Aging Management Plan for Prolonged Shutdown Periods (MRP-435)*. Palo Alto, California: Electric Power Research Institute, 2018.

[92] Jean-Christophe Niel ea. "La poursuite de fonctionnement des centrales nucléaires au-delà de 40 ans." In: *Contrôle* 198 (2014), pp. 4–28.

[93] Garnier V et al. "Non Destructive Evaluation for containment monitoring". In: *TINCE 2018 – Technological Innovations in Nuclear Civil Engineering*. Paris-Saclay, France, 2018.

[94] Sbartaï M et al. "Non-destructive evaluation of concrete damages of containment walls in nuclear power plants". In: *Academic journal of civil engineering - Special Issue - RUGC 2018 St Etienne* 36.1 (2018).

[95] Garnier V et al. "Non-destructive evaluation of containment walls in nuclear power plants". In: *43rd Review of Progress in QNDE, AIP Conference Proceedings 1806 (1)*. Atlanta, Georgia, 2017.

[96] Clayton DA, Barker AM, Santos-Villalobos HJ, Albright AP, Hoegh K, and Khazanovich L. *Nondestructive Evaluation of Thick Concrete Using Advanced Signal Processing Techniques*. Tech. rep. USA: Oak Ridge National Lab. (ORNL), Oak Ridge, TN (United States), 2015. DOI: 10.2172/1221739.

[97] Scott DB. "Internal inspection of reinforced concrete for nuclear structures using shear wave tomography". In: *Energy Conversion and Management* 74 (2013), pp. 582–586.

[98] Okayasu M and Yamasaki T. "Structural Health Monitoring System for Remote Inspection of Material Failure". In: *Journal of Nondestructive Evaluation* 38.2 (2019), pp. 1–6.

[99] Bui D, Kodjo SA, Rivard P, and Fournier B. "Evaluation of concrete distributed cracks by ultrasonic travel time shift under an external mechanical perturbation: Study of indirect and semi-direct transmission configurations". In: *Journal of Nondestructive Evaluation* 32.1 (2013), pp. 25–36.

[100] Jin J, Xi W, Riviere J, and Shokouhi P. "Single-Impact Nonlinear Resonant Acoustic Spectroscopy for Monitoring the Progressive Alkali–Silica Reaction in Concrete". In: *Journal of Nondestructive Evaluation* 38.3 (2019). URL: https://doi.org/10.1007/s10921-019-0614-5.

[101] Kurtis K, Xi Y, Glinicki M, Provis J, Giannini E, and Fu T. "Can We Design Concrete to Survive Nuclear Environments?" In: *Concrete International* 39.11 (2017), pp. 29–35.

[102] Andrade C, Martínez I, Castellote M, and Zuloaga P. "Some principles of service life calculation of reinforcements and in situ corrosion monitoring by sensors in the radioactive waste containers of El Cabril disposal (Spain)". In: *Journal of Nuclear Materials* 358.2-3 (2006), pp. 82–95.

[103] Duffó GS, Arva EA, Schulz FM, and Vazquez DR. "Durability of a reinforced concrete designed for the construction of an intermediate-level radioactive waste disposal facility". In: *Materials Research Society Symposium Proceedings* 1475.December (2012), pp. 385–390.

[104] Iliopoulos S et al. "Detection and evaluation of cracks in the concrete buffer of the Belgian Nuclear Waste container using combined NDT techniques". In: *Construction and Building Materials* 78 (2015), pp. 369–378.

[105] Maruyama I, Sasano H, Nishioka Y, and Igarashi G. "Strength and Young's modulus change in concrete due to long-term drying and heating up to 90 °c". In: *Cement and Concrete Research* 66 (2014), pp. 48–63.

[106] Trivedi N and Singh RK. "Assessment of in-situ concrete creep: Cylindrical specimen and prototype nuclear containment structure". In: *Construction and Building Materials* 71 (2014), pp. 16–25.

[107] Li J et al. "Nuclear power plant prestressed concrete containment vessel structure monitoring during integrated leakage rate testing using fiber Bragg grating sensors". In: *Applied Sciences (Switzerland)* 7.4 (2017).

[108] Perry M, Yan Z, Sun Z, Zhang L, Niewczas P, and Johnston M. "High stress monitoring of prestressing tendons in nuclear concrete vessels using fibre-optic sensors". In: *Nuclear Engineering and Design* 268 (2014), pp. 35–40.

[109]   Henault JM et al. "Truly distributed optical fiber sensors for structural health monitoring: From the telecommunication optical fiber drawling tower to water leakage detection in dikes and concrete structure strain monitoring". In: *Advances in Civil Engineering* 2010 (2010).

[110]   Hermand G, Bethmont S, Landolt M, and Lesoille S. "Optical Fiber for 3D Imaging of Deformations in Concrete Containers Stacked". In: *Structural Health Monitoring*. Châtenay-Malabry, France, 2017.

[111]   Simon A, Oukhemanou E, and Courtois A. "Structural Monitoring of Prestressed Concrete Containments of Nuclear Power Plants for Ageing". In: *Technical Innovation in Nuclear Civil Engineering* (2013).

[112]   Praveechandra Y, Roy R, Rao NM, and Shrivastava A. "Structural monitoring and response analysis of prestressed concrete primary containment of a nuclear power plant". In: *Peocedia Engineering* 86 (2014), pp. 554–559.

[113]   Parmar RM, Singh T, Thangamani I, Trivedi N, and Singh RK. "Overpressure test on BARCOM pre-stressed concrete containment". In: *Nuclear Engineering and Design* 269 (2014), pp. 177–183.

[114]   Hu HT and Lin YH. "Ultimate analysis of PWR prestressed concrete containment subjected to internal pressure". In: *International Journal of Pressure Vessels and Piping* 83.3 (2006), pp. 161–167.

[115]   Brincker R and Ventura CE. *Introduction to Operational Modal Analysis*. John Wiley and Sons, Ltd., 2015. ISBN: 9781119963158.

[116]   Rainieri C and Fabbrocino G. *Operational Modal Analysis of Civil Engineering Structures*. Springer, 2014.

[117]   Schanke SA. "Operational Modal Analysis of Large Bridges". Master's Thesis. Norweigian Universityof Science and Technology, 2015.

[118]   Choi S, Park S, Hyun CH, Kim MS, and Choi KR. "Modal parameter identification of a containment using ambient vibration measurements". In: *Nuclear Engineering and Design* 240.3 (2010), pp. 453–460.

[119]   AFNOR. *NF EN 12390-3:2012 Testing hardened concrete - Part 3: Compressive strength of test specimens*. 2012.

[120]   AFNOR. *NF EN 12390-13:2014 Testing hardened concrete - Part 13: Determination of secant modulus of elasticity in compression*. 2014.

[121] "Time-frequency analysis of small frequency variations in civil engineering structures under weak and strong motions using a reassignment method". In: *Structural Health Monitoring* 9.2 (2010), pp. 159–171.

[122] Ditommaso R, Parolai S, Mucciarelli M, Eggert S, Sobiesiak M, and Zschau J. "Monitoring the response and the back-radiated energy of a building subjected to ambient vibration and impulsive action: The Falkenhof Tower (Potsdam, Germany)". In: *Bulletin of Earthquake Engineering* 8.3 (2010), pp. 705–722.

[123] Frost J. *Regression Analysis an Intuitive Guide for Using and Interpreting Linear Models*. 1st. Jim Frost, 2019. URL: statisticsbyjim.com.

[124] Piacsek AA, Abdul-Wahid S, and Taylor R. "Resonance frequencies of a spherical aluminum shell subject to static internal pressure". In: *The Journal of the Acoustical Society of America* 131.6 (2012), EL506–EL512.

[125] Lott M. "Three-dimensional approach of the elastic nonlinear behavior of rocks and concretes". PhD thesis. PhD Thesis, Aix-Marseille University, 2017.

[126] Hann Y de and Sluimer G. "Standard linear solid model for dynamic and time dependent behaviour of building material". In: *HERON* 46.1 (2001), pp. 49–76.

APPENDICES

Appendix 1

Analysis of a standard linear viscoelastic solid model

The linear viscoelastic solid model is composed of two springs (elastic element) and a damper (viscous element). These can be grouped into a Voigt description or into a Maxwell description. Both descriptions are depicted in figure A1.1 and provide equivalent results.
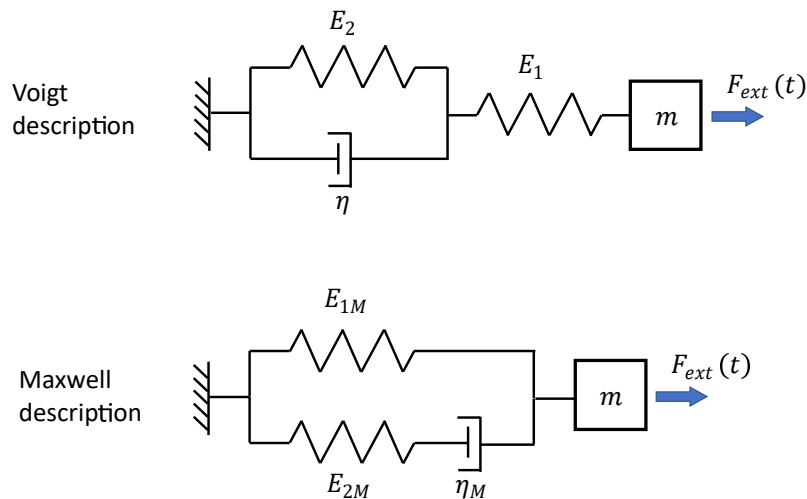

Figure A1.1: Standard linear viscoelastic solid equivalent models, including mass m and external force $F_{ext}(t)$.

The equivalence between both sets of parameters is given by

$$E_{1M} = \frac{E_1 E_2}{E_1 + E_2},$$

(A1.1)

$$E_{2M} = \frac{E_1^2}{E_1 + E_2}, \tag{A1.2}$$

$$\eta_M = \frac{E_1^2 \eta}{(E_1 + E_2)^2}. \tag{A1.3}$$

Using the Voigt description of the viscoelastic solid, its constitutive equation is

$$F_{int} + \frac{\eta}{E_1 + E_2}\dot{F}_{int} = \frac{E_1 E_2}{E_1 + E_2}x + \frac{\eta E_1}{E_1 + E_2}\dot{x}, \tag{A1.4}$$

where x is the displacement from resting position and F_{int} is the time-dependent "internal" force, which connects the springs-damper system to the mass. Thus by applying the 2nd Newton's Law

$$F_{ext} - F_{int} = m\ddot{x}. \tag{A1.5}$$

Thus, by combining equations (A1.4) and (A1.5) we obtain

$$F_{ext} + \frac{\eta}{E_1 + E_2}\dot{F}_{ext} = \frac{\eta m}{E_1 + E_2}\dddot{x} + m\ddot{x} + \frac{E_1 \eta}{E_1 + E_2}\dot{x} + \frac{E_1 E_2}{E_1 + E_2}x. \tag{A1.6}$$

If we force the system at a given amplitude F_0 and frequency Ω, that is

$$F_{ext}(t) = F_0 e^{i\Omega t}, \tag{A1.7}$$

then the steady-state solution would have the form

$$x(t) = B e^{i\Omega t}, \tag{A1.8}$$

where B is a complex constant, that can be obtained from trying the solution (equation (A1.8)) into equation (A1.6). Once B is calculated, we get x and its derivatives in terms of the viscoelastic material constants (E_1, E_2, and η), the forcing frequency Ω and time t; and we can also calculate F_{int} in terms of those parameters.

Once F_{int} and x are known, the complex modulus E^* of the viscoelastic solid can be computed by carrying out $E^* = F_{int}/x$, thus

$$E^* = \frac{E_1(E_2 + i\eta\Omega)(E_1 + E_2 - i\eta\Omega)}{(E_1 + E_2)^2 + \eta^2\Omega^2}. \tag{A1.9}$$

The complex modulus E^* is composed by its real part, named storage modulus E', which is related to the elasticity of the solid and its capacity to store elastic energy, and by its imaginary part, named loss modulus E'', which is related to the viscosity of the solid and its energy losses during the stress-strain process. Thus,

$$E^* = E' + iE''. \tag{A1.10}$$

Therefore, by taking the real part of equation (A1.9) we get

$$E' = \frac{E_1 E_2 (E_1 + E_2) + E_1 \eta^2 \Omega^2}{(E_1 + E_2)^2 + \eta^2 \Omega^2}. \tag{A1.11}$$

For the case of free vibration, in which $F_{ext}(t) = 0$, let us follow the derivation carried out by de Haan and Sluimer [126]. Their derivation uses the Maxwell description of the standard linear viscoelastic solid, as shown in Figure A1.1, so here let us use that one too. Thus, let us first define

$$K = \frac{E_{1M} m}{\eta_M^2}, \tag{A1.12}$$

$$M = \frac{\eta_M^2}{E_{2M} m}, \tag{A1.13}$$

and the dimensionless time variable

$$\tau = \frac{\eta_M}{m} t. \tag{A1.14}$$

With these definitions, equation (A1.6) becomes

$$M \frac{d^3 x}{d\tau^3} + \frac{d^2 x}{d\tau^2} + (1 + KM) \frac{dx}{d\tau} + Kx = 0. \tag{A1.15}$$

By substituting a solution of the form $x(\tau) = x_0 e^{\lambda \tau}$ into equation (A1.15) we obtain the characteristic polynomial

$$M\lambda^3 + \lambda^2 + (1 + KM)\lambda + K = 0. \tag{A1.16}$$

The set of solutions that corresponds to an oscillatory movement (because it is assumed the solid is slightly damped) is given by

$$\lambda_1 = -(a + ib),$$

156

$$\lambda_2 = -(a - ib),$$

$$\lambda_3 = -c,$$

where a, b and c are positive and real. Thus, for a standard linear viscoelastic slightly damped solid, the solution of equation (A1.6) is

$$x(\tau) = A_1 e^{-a\tau} cos(b\tau) + A_2 e^{-c\tau}, \tag{A1.17}$$

where A_1 and A_2 are real constants that depend on the initial conditions, and the angular frequency of vibration is given by

$$\omega_{SLS,Free} = \frac{b\eta_M}{m} = \frac{b\eta}{m} \frac{E_1^2}{(E_1 + E_2)^2}. \tag{A1.18}$$

where the subindex "SLS,Free" stands for free vibration of the standar linear viscoelastic solid.

Note that in this derivation the spring constants E_1 and E_2 could represent any constants of elasticity of a given one-dimensional model, such as the shear elastic moduli named G_{a0} and G_{v0} in Chapter 5. Using the experimental data of the mortar specimen indicated in Chapter 5, and using the best-fit G_{a0} and G_{v0}, let us calculate the angular frequency of vibration given by equation (A1.18), which yields

$$\omega_{SLS,Free} = 10133 \text{ rad/s}.$$

Let us use the $\omega_{SLS,Free}$ value to estimate the storage modulus G'_{est} ("est" for estimated) by using the traditional linear-elastic equation (2.29) or (3.11), which yields

$$G'_{est} = 9.56 \text{ GPa}.$$

But we can calculate the actual G' by introducing the viscoelastic parameters obtained in Chapter 4 into equation (A1.11), which yields

$$G' = 9.53 \text{ GPa}.$$

The estimated storage modulus G'_{est} is only 0.3 % different from the actual storage modulus G'. This finding means that, given a viscoelastic solid, which vibrates freely at frequency $\omega_{SLS,Free}$, then it is possible to estimate the storage

modulus $G'(\Omega = \omega_{SLS,Free})$ by calculating it using the traditional formula of linear-elasticity.

Appendix 2

Code for analytical derivation of β_E and β_G

2.1.   Part 1: β_E

```
clear all; clc; close all;

% En este script aplico la tensión cuasistática y ...
% obtengo el estiramiento
% lateral b en funciónd el estiramiento longitudinal a, ...
% dada la condición
% de borde S22=0.

syms a b h u l m n e11 e12 e13 e21 e22 e23 e31 e32 ...
e33 ei11
% e1, e2, deformaciones de Lagrange en direccion 1 y 2.
% h = lambda, primera constante de Lame.
% u = mu, segunda constante de Lame.
% l, m, n = constantes de 3er orden.

%% Tensores F y C
display('Tensor de estiramientos F:')

assume(a,'real');assumeAlso(a>1);assumeAlso(a<2);
```

```matlab
assume(b,'real');assumeAlso(b>0);assumeAlso(b<1);
assume(h,'real');assumeAlso(h>1e9);
assume(u,'real');assumeAlso(u>1e9);
assume(l,'real');assumeAlso(l<-1e12);
assume(m,'real');assumeAlso(m<-1e12);
assume(n,'real');assumeAlso(n<-1e12);


F = [ a 0  0;...
0  b 0;...
0  0  b]


C = F'*F


%% Tensor de Deformaciones de Lagrange E
display('Tensor de Def. de Lagrange:')
% E = [ e1 0  0;...
%       0  e2 0;...
%       0  0  e2]


E = (1/2)*(C-eye(3))


Egen = [e11 e12 e13;...
e21 e22 e23;...
e31 e32 e33];


%% Invariantes
display('Invariantes:')
I1 = trace(Egen)                       % 1er Invariante
I2 = simplify( (-1/2)* (trace(Egen^2) - ...
(trace(Egen))^2) )  % 2do Invariante
I3 = simplify( det(Egen) )             % 3er Invariante


%% Energía de Deformación
display('Energia de deformacion:')
Waux = (1/2)*(h+2*u)*I1^2  -  2*u*I2  +  ...
(1/3)*(l+2*m)*I1^3  -  2*m*I1*I2  +  n*I3;
```

```matlab
W = simplify(Waux)

%% Tensor de Cosserat S
S11 = simplify(diff(W,e11));
S12 = simplify(diff(W,e12));
S13 = simplify(diff(W,e13));
S21 = simplify(diff(W,e21));
S22 = simplify(diff(W,e22));
S23 = simplify(diff(W,e23));
S31 = simplify(diff(W,e31));
S32 = simplify(diff(W,e32));
S33 = simplify(diff(W,e33));


S11 = subs(S11,[e11 e12 e13 e21 e22 e23 e31 e32 e33],...
[E(1,1) E(1,2) E(1,3) E(2,1) E(2,2) E(2,3) E(3,1) E(3,2) E(3,3)]);
S12 = subs(S12,[e11 e12 e13 e21 e22 e23 e31 e32 e33],...
[E(1,1) E(1,2) E(1,3) E(2,1) E(2,2) E(2,3) E(3,1) E(3,2) E(3,3)]);
S13 = subs(S13,[e11 e12 e13 e21 e22 e23 e31 e32 e33],...
[E(1,1) E(1,2) E(1,3) E(2,1) E(2,2) E(2,3) E(3,1) E(3,2) E(3,3)]);
S21 = subs(S21,[e11 e12 e13 e21 e22 e23 e31 e32 e33],...
[E(1,1) E(1,2) E(1,3) E(2,1) E(2,2) E(2,3) E(3,1) E(3,2) E(3,3)]);
S22 = subs(S22,[e11 e12 e13 e21 e22 e23 e31 e32 e33],...
[E(1,1) E(1,2) E(1,3) E(2,1) E(2,2) E(2,3) E(3,1) E(3,2) E(3,3)]);
S23 = subs(S23,[e11 e12 e13 e21 e22 e23 e31 e32 e33],...
[E(1,1) E(1,2) E(1,3) E(2,1) E(2,2) E(2,3) E(3,1) E(3,2) E(3,3)]);
S31 = subs(S31,[e11 e12 e13 e21 e22 e23 e31 e32 e33],...
[E(1,1) E(1,2) E(1,3) E(2,1) E(2,2) E(2,3) E(3,1) E(3,2) E(3,3)]);
S32 = subs(S32,[e11 e12 e13 e21 e22 e23 e31 e32 e33],...
[E(1,1) E(1,2) E(1,3) E(2,1) E(2,2) E(2,3) E(3,1) E(3,2) E(3,3)]);
S33 = subs(S33,[e11 e12 e13 e21 e22 e23 e31 e32 e33],...
[E(1,1) E(1,2) E(1,3) E(2,1) E(2,2) E(2,3) E(3,1) E(3,2) E(3,3)]);


S = [   S11 S12 S13;...
S21 S22 S33;...
S31 S32 S33];
```

```
%% Condicion de borde para hallar b en funcion de a

b_sol  = solve(S22, b); % Impongo S2=0 y despejo b

% hay dos soluciones, elijo la segunda en este caso que es ...
%la que da menor que 1
b_sol_fin = simplify(b_sol(1),'steps',100)

%% Armo tensor de Cauchy material

J = det(F);
T = F*(J^(-1))*S*(F');
T11 = T(1,1); % expresado en funcion de a, b, 0 y demás parámetros
T11_sol = simplify(subs(T11,b,b_sol_fin)) % expresión de S11

%% Beta E

T11_sol_eps = subs(T11_sol,a,ei11+1); % sustituyo el estiramiento...
%a por la deformación de ingeniería

T11_sol_t = simplify(taylor(T11_sol_eps,ei11,'Order',3)) ...
% aplico taylor de "orden 3" para coeficientes en 1, e y e^2.

% Verifico que el coeficiente en eps es igual al módulo elástico Y.

BetaE = simplify( ( ( T11_sol_t - (ei11*u*(3*h + 2*u))/(h + u) ) /...
   (ei11^2)) /  (u*(3*h + 2*u)/(h + u)) )

BetaE_xE = ( ( T11_sol_t - (ei11*u*(3*h + 2*u))/(h + u) ) / (ei11^2))

return

%% Verificación numérica

Y_num = 42.36e9; % Módulo de Young
v_num = 0.21 ;   % Poisson
```

```
h_num = Y_num*v_num / ((1+v_num)*(1-2*v_num));
u_num = Y_num / (2*(1+v_num));
l_num = -3.01e12;
m_num = -2.28e12;
n_num = -1.81e12;
a_num = 1.001;
%
% double(simplify(subs(b_sol_fin,[h u l m n a],...
[h_num u_num l_num m_num n_num a_num])))

BetaE_num = subs(BetaE,[h u l m n],[h_num u_num l_num m_num n_num])

double(BetaE_num)

BetaE_Matematica = (2*m_num - l_num*(-1+2*v_num )^3 +...
 Y_num *(3/2+2*v_num)+ (v_num^2)*(3*n_num-2*m_num*(3+2*v_num )))/Y_num
```

2.2. Part 2: β_G

```
clc
clear all
close all

% X1: coordenada indeformada 1
% X2: coordenada indeformada 2
% X3: coordenada indeformada 3
% O: barrenado, constante
% a: estiramiento en direccion 1
% b: estiramiento en direccion 2 y 3

syms X1 X2 X3 a b O e11 e12 e13 e21 e22 e23 e31 ...
e32 e33 h u l m n
```

```
assume(a,'real')
assumeAlso(a>1)
assumeAlso(a<1.5)
assume(b,'real')
assumeAlso(b>0)
assumeAlso(b<1)
assume(O,'real')
assumeAlso(O>0)
assumeAlso(O<1)
assume(X1,'real')
assume(X2,'real')
assume(X3,'real')
assume(e11,'real')
assumeAlso(e11<1)
assume(e12,'real')
assumeAlso(e12<1)
assume(e13,'real')
assumeAlso(e13<1)
assume(e22,'real')
assumeAlso(e22<1)
assume(e23,'real')
assumeAlso(e23<1)
assume(e33,'real')
assumeAlso(e33<1)
assume(h,'real')
assumeAlso(h>1e6)
assume(u,'real')
assumeAlso(u>1e6)
assume(l,'real')
assumeAlso(l<-1e9)
assume(m,'real')
assumeAlso(m<-1e9)
assume(n,'real')
assumeAlso(n<-1e9)

%% Tensor de deformación X:
```

```matlab
x1 = a*X1;
x2 = cos(a*O*X1)*b*X2 - sin(a*O*X1)*b*X3;
x3 = cos(a*O*X1)*b*X3 + sin(a*O*X1)*b*X2;


X = [x1,x2,x3]';

%% Tensor F
% F es el gradiente de X

display('Tensor de estiramientos F:')

F = [  diff(x1,X1),diff(x1,X2),diff(x1,X3);...
diff(x2,X1),diff(x2,X2),diff(x2,X3);...
diff(x3,X1),diff(x3,X2),diff(x3,X3)]

%% Tensor C

C = F'*F;

%% Tensor E
display('Tensor de Def. de Lagrange:')

E = (1/2)*(C-eye(3))

% Tensor de Lagrange genérico:
Egen = [e11 e12 e13;...
e21 e22 e23;...
e31 e32 e33];


%% Invariantes
display('Invariantes:')
I1 = trace(Egen)                % 1er Invariante generico
I2 = simplify( (-1/2)* (trace(Egen^2) - ...
(trace(Egen))^2) )  % 2do Invariante genérico
```

```
I3 = simplify( det(Egen) )      % 3er Invariante genérico


%% Energía de Deformación
% display('Energia de deformacion:')
Waux = (1/2)*(h+2*u)*I1^2  -  2*u*I2  +  ...
(1/3)*(l+2*m)*I1^3  -  2*m*I1*I2  +  n*I3;
W = simplify(Waux);


% Comprobación de los invariantes:
% A = n;
% B = m-n/2;
% C = l-m+n/2;
% W2 = h/2*(trace(E))^2 + u*trace(E^2) + ...
C/3*(trace(E))^3 + B*(trace(E))*trace(E^2) + ...
A/3*trace(E^3)
% simplify(W-W2,'Steps',20)
% return


%% Tensor de Cosserat S genérico

Sg11 = simplify(diff(W,e11));
Sg12 = simplify(diff(W,e12));
Sg13 = simplify(diff(W,e13));
Sg21 = simplify(diff(W,e21));
Sg22 = simplify(diff(W,e22));
Sg23 = simplify(diff(W,e23));
Sg31 = simplify(diff(W,e31));
Sg32 = simplify(diff(W,e32));
Sg33 = simplify(diff(W,e33));


Sg = [  Sg11 Sg12 Sg13;...
Sg21 Sg22 Sg23;...
Sg31 Sg32 Sg33]; % tensor de Cosserat genérico

% Constuyo tensor de Cosserat S
% (en donde E(2,3) = 0, VERIFICAR!)
```

```
S11 = subs(Sg11,[e11 e12 e13  e21 e22 e23  e31 e32 e33],...
[E(1,1) E(1,2) E(1,3)  E(2,1) E(2,2) E(2,3)  E(3,1) E(3,2) E(3,3)]);
S12 = subs(Sg12,[e11 e12 e13 e21 e22 e23  e31 e32 e33],...
[E(1,1) E(1,2) E(1,3) E(2,1) E(2,2) E(2,3) E(3,1) E(3,2) E(3,3)]);
S13 = subs(Sg13,[e11 e12 e13 e21 e22 e23  e31 e32 e33],...
[E(1,1) E(1,2) E(1,3) E(2,1) E(2,2) E(2,3) E(3,1) E(3,2) E(3,3)]);
S21 = subs(Sg21,[e11 e12 e13 e21 e22 e23  e31 e32 e33],...
[E(1,1) E(1,2) E(1,3) E(2,1) E(2,2) E(2,3) E(3,1) E(3,2) E(3,3)]);
S22 = subs(Sg22,[e11 e12 e13 e21 e22 e23  e31 e32 e33],...
[E(1,1) E(1,2) E(1,3) E(2,1) E(2,2) E(2,3) E(3,1) E(3,2) E(3,3)]);
S23 = subs(Sg23,[e11 e12 e13 e21 e22 e23  e31 e32 e33],...
[E(1,1) E(1,2) E(1,3) E(2,1) E(2,2) E(2,3) E(3,1) E(3,2) E(3,3)]);
S31 = subs(Sg31,[e11 e12 e13 e21 e22 e23  e31 e32 e33],...
[E(1,1) E(1,2) E(1,3) E(2,1) E(2,2) E(2,3) E(3,1) E(3,2) E(3,3)]);
S32 = subs(Sg32,[e11 e12 e13 e21 e22 e23  e31 e32 e33],...
[E(1,1) E(1,2) E(1,3) E(2,1) E(2,2) E(2,3) E(3,1) E(3,2) E(3,3)]);
S33 = subs(Sg33,[e11 e12 e13 e21 e22 e23  e31 e32 e33],...
[E(1,1) E(1,2) E(1,3) E(2,1) E(2,2) E(2,3) E(3,1) E(3,2) E(3,3)]);


S = [S11 S12 S13;
S12 S22 S23
S13 S23 S33]



%%
% Tensor de tensiones material
J = det(F);
T = F*(J^(-1))*S*(F');
T12 = T(1,2); % expresado en funcion de a, b, O y demás parámetros
%%
% sustituyo el valor de b hayado anteriormente

% solución 1 de b:
b_sol = (4*h - 12*l - 2*m - n + 4*u + 4*a^2*l - 2*a^2*m + a^2*n - ...
(4*a^4*m^2 - 4*a^4*m*n - 24*l*a^4*m + a^4*n^2 + 8*l*a^4*n - ...
```

```
32*a^2*h*m + 8*a^2*h*n - 8*a^2*m^2 + 8*a^2*m*n - 16*a^2*m*u + ...
48*l*a^2*m - 2*a^2*n^2 + 8*a^2*n*u - 16*l*a^2*n + 32*l*a^2*u + ...
16*h^2 + 32*h*m - 8*h*n + 32*h*u + 4*m^2 - 4*m*n + 16*m*u - ...
24*l*m + n^2 - 8*n*u + 8*l*n + 16*u^2 - 32*l*u)^(1/2))^(1/2)/...
(2*(- 2*l - m)^(1/2));


% solución 2 de b:
% b_sol =(3*(l/3 + (2*m)/3)*(4*h + 4*m - n + 4*u - 4*a^2*m + ...
%a^2*n + (4*a^4*m^2 - 4*a^4*m*n - 24*l*a^4*m + a^4*n^2 + ...
%8*l*a^4*n - ...
%32*a^2*h*m + 8*a^2*h*n - 8*a^2*m^2 + 8*a^2*m*n - 16*a^2*m*u + ...
%48*l*a^2*m - 2*a^2*n^2 + 8*a^2*n*u - 16*l*a^2*n + 32*l*a^2*u + ...
%16*h^2 + 32*h*m - 8*h*n + 32*h*u + 4*m^2 - 4*m*n + 16*m*u - ...
%24*l*m + n^2 - 8*n*u + 8*l*n + 16*u^2 - 32*l*u)^(1/2))^2)/...
%(16*(2*l + m)^2) - 2*m*((4*h - 4*l + 2*m - n + 4*u + 4*a^2*l -...
%2*a^2*m + a^2*n + (4*a^4*m^2 - 4*a^4*m*n - 24*l*a^4*m + ...
%a^4*n^2 + 8*l*a^4*n - 32*a^2*h*m + 8*a^2*h*n - 8*a^2*m^2 + ...
%8*a^2*m*n - 16*a^2*m*u + 48*l*a^2*m - 2*a^2*n^2 + 8*a^2*n*u - ...
%16*l*a^2*n + 32*l*a^2*u + 16*h^2 + 32*h*m - 8*h*n + 32*h*u +...
%4*m^2 - 4*m*n + 16*m*u - 24*l*m + n^2 - 8*n*u + 8*l*n + ...
%16*u^2 - 32*l*u)^(1/2))^2/(64*(2*l + m)^2) - (2*(a^2/2 - ...
%1/2)*(4*h - 4*l + 2*m - n + 4*u + 4*a^2*l - 2*a^2*m + ...
%a^2*n + (4*a^4*m^2 - 4*a^4*m*n - 24*l*a^4*m + a^4*n^2 + ...
%8*l*a^4*n - 32*a^2*h*m + 8*a^2*h*n - 8*a^2*m^2 + 8*a^2*m*n -...
%16*a^2*m*u + 48*l*a^2*m - 2*a^2*n^2 + 8*a^2*n*u -...
%16*l*a^2*n + 32*l*a^2*u + 16*h^2 + 32*h*m - 8*h*n + 32*h*u +...
%4*m^2 - 4*m*n + 16*m*u - 24*l*m + n^2 - 8*n*u + 8*l*n + 16*u^2 -...
%32*l*u)^(1/2)))/(16*l + 8*m)) - ((h/2 + u)*(4*h + 4*m -...
% n + 4*u -...
%4*a^2*m + a^2*n + (4*a^4*m^2 - 4*a^4*m*n - 24*l*a^4*m + a^4*n^2 + ...
%8*l*a^4*n - 32*a^2*h*m + 8*a^2*h*n - 8*a^2*m^2 + 8*a^2*m*n - ...
    %16*a^2*m*u + 48*l*a^2*m - 2*a^2*n^2 + 8*a^2*n*u - 16*l*a^2*n +...
%32*l*a^2*u + 16*h^2 + 32*h*m - 8*h*n + 32*h*u + 4*m^2 - 4*m*n +...
%16*m*u - 24*l*m + n^2 - 8*n*u + 8*l*n + 16*u^2 - 32*l*u)^(1/2)))/...
%(4*l + 2*m) + (n*(4*h - 4*l + 2*m - n + 4*u + 4*a^2*l - 2*a^2*m +...
%a^2*n + (4*a^4*m^2 - 4*a^4*m*n - 24*l*a^4*m + a^4*n^2 +...
```

```
% 8*l*a^4*n - ...
%32*a^2*h*m + 8*a^2*h*n - 8*a^2*m^2 + 8*a^2*m*n - 16*a^2*m*u +...
% 48*l*a^2*m - ...
%2*a^2*n^2 + 8*a^2*n*u - 16*l*a^2*n + 32*l*a^2*u + 16*h^2 + 32*h*m - ...
%8*h*n + 32*h*u + 4*m^2 - 4*m*n + 16*m*u - 24*l*m + n^2 -...
% 8*n*u + 8*l*n + ...
%16*u^2 - 32*l*u)^(1/2))^2)/(64*(2*l + m)^2) + (2*u*(4*h - 4*l + 2*m -...
%n + 4*u + 4*a^2*l - 2*a^2*m + a^2*n + (4*a^4*m^2 - 4*a^4*m*n - ...
%24*l*a^4*m + a^4*n^2 + 8*l*a^4*n - 32*a^2*h*m + 8*a^2*h*n -...
% 8*a^2*m^2 +...
%8*a^2*m*n - 16*a^2*m*u + 48*l*a^2*m - 2*a^2*n^2 + ...
%8*a^2*n*u - 16*l*a^2*n +...
%32*l*a^2*u + 16*h^2 + 32*h*m - 8*h*n + 32*h*u + 4*m^2 -...
%4*m*n + 16*m*u -...
%24*l*m + n^2 - 8*n*u + 8*l*n + 16*u^2 - 32*l*u)^(1/2)))/...
%(8*l + 4*m) -...
%(m*(4*h + 4*m - n + 4*u - 4*a^2*m + a^2*n + (4*a^4*m^2 -...
%4*a^4*m*n -...
%24*l*a^4*m + a^4*n^2 + 8*l*a^4*n - 32*a^2*h*m + 8*a^2*h*n -...
%8*a^2*m^2 + ...
%8*a^2*m*n - 16*a^2*m*u + 48*l*a^2*m - 2*a^2*n^2 + 8*a^2*n*u -...
%16*l*a^2*n +...
%32*l*a^2*u + 16*h^2 + 32*h*m - 8*h*n + 32*h*u + 4*m^2 - ...
%4*m*n + 16*m*u - ...
%24*l*m + n^2 - 8*n*u + 8*l*n + 16*u^2 - 32*l*u)^(1/2))*(4*h -...
%4*l + 2*m -...
%n + 4*u + 4*a^2*l - 2*a^2*m + a^2*n + (4*a^4*m^2 - 4*a^4*m*n -...
%24*l*a^4*m + ...
%a^4*n^2 + 8*l*a^4*n - 32*a^2*h*m + 8*a^2*h*n - 8*a^2*m^2 +...
%8*a^2*m*n - ...
%16*a^2*m*u + 48*l*a^2*m - 2*a^2*n^2 + 8*a^2*n*u - 16*l*a^2*n +...
%32*l*a^2*u +...
%16*h^2 + 32*h*m - 8*h*n + 32*h*u + 4*m^2 - 4*m*n + 16*m*u - ...
%24*l*m + n^2 - ...
%8*n*u + 8*l*n + 16*u^2 - 32*l*u)^(1/2)))/(8*(2*l + m)^2)
```

```matlab
T12_s = subs(T12,b,b_sol) % sustityo b

T12_s = simplify(T12_s,'Steps',100) % LLEVA TIEMPO
%
% T11 = T(1,1);
% T11_s = subs(T11,b,b_sol) % sustityo b
% % % T11_s = simplify(T11_s,'Steps',100)
% %
% T33 = T(3,3);
% T33_s = subs(T33,b,b_sol) % sustityo b
%
% T22 = T(2,2);
% T22_s = subs(T22,b,b_sol) % sustityo b

%% verificaciones

Y_num = 42.36e9; % Módulo de Young
v_num = 0.21 ;   % Poisson
h_num = Y_num*v_num / ((1+v_num)*(1-2*v_num));
u_num = Y_num / (2*(1+v_num));
l_num = -3.01e12;
m_num = -2.28e12;
n_num = -1.81e12;
a_num = 1.001;
O_num = 0.0001;
X1_num = 0.3;
X2_num = 0.15;
X3_num = 0.15;
b_num = -0.000178951+1;

% subs(W,[h u l m n a b O X1 X2 X3],[h_num u_num l_num m_num...
%n_num a_num b_num O_num X1_num X2_num X3_num])
% double(ans)

% subs(T11_s,[h u l m n a O X1 X2 X3],[h_num u_num l_num m_num...
%n_num a_num O_num X1_num X2_num X3_num]);
```

170

```matlab
% double(ans)
% %
% subs(T33_s,[h u l m n a O X1 X2 X3],[h_num u_num l_num...
%m_num n_num a_num O_num X1_num X2_num X3_num]);
% double(ans)
%
% subs(T22_s,[h u l m n a O X1 X2 X3],[h_num u_num l_num m_num...
%n_num a_num O_num X1_num X2_num X3_num]);
% double(ans)

% subs(T,[h u l m n a O b X1 X2 X3],[h_num u_num l_num m_num...
%n_num a_num O_num  b_num X1_num 0.15/sqrt(2) 0.15/sqrt(2)])



%%

T12_s_t = taylor(T12_s,O,0,'Order',2)  % taylor para linealizar en O (tita)

G_eps = T12_s_t / (O*(-X3)) % calculo G_epsilon

syms ei11 % defino epsilon de ingenieria ei11
assume(ei11<1);assumeAlso(ei11>-1);
G_eps_s = subs(G_eps,a,ei11+1)

G_eps_s_t = taylor(G_eps_s,ei11,'Order',2)

G_eps_s_t = simplify(G_eps_s_t)

% pretty(simplify(subs(G_eps_s_t,ei11,0)))

%%
BetaG = simplify((G_eps_s_t-u)/(u*ei11))

pretty(BetaG)

double(subs(BetaG,[h u l m n],[h_num u_num l_num m_num n_num]))
```

```
BetaG_Matematica = (u_num*(3+v_num)+...
((m_num*(2-4*v_num )+n_num*v_num))/2)/u_num
```

Appendix 3

Analysis of the torsional vibration of a shaft with torsional springs at each end

Let us consider an elongated solid of of length L with uniform section along its axis, density ρ, and polar moment of inertia I_p. Consider a differential volume of length dx and its angle of twist given by $\theta(x,t)$, where x is the coordinate parallel to the axial direction, and t is time. A pair of torsional moments appear at each end of the volume, as shown in Figure A3.1. These moments are M_θ and $(M_\theta + \frac{\partial M_\theta}{\partial x}dx)$.
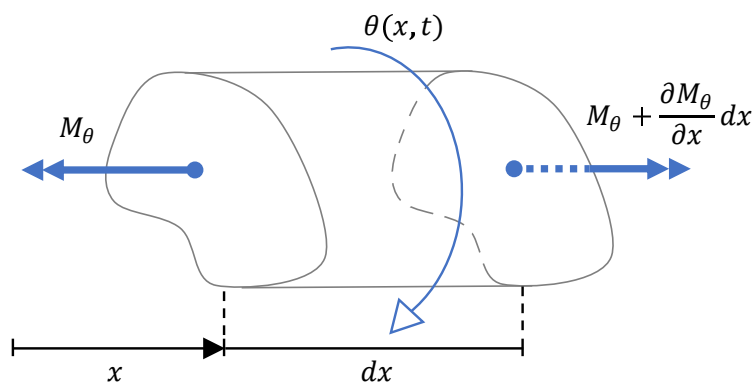

Figure A3.1: Differential volume with torsional moments at each end.

By applying the 2nd Newton's Law to the differential volume we get

$$-M_\theta + (M_\theta + \frac{\partial M_\theta}{\partial x}dx) = \rho dx I_p \frac{\partial^2 \theta}{\partial t^2} \Rightarrow$$

173

$$\frac{\partial M_\theta}{\partial x}(x,t) = \rho I_p \frac{\partial^2 \theta}{\partial t^2}(x,t). \tag{A3.1}$$

From the strength of materials, considering the Saint-Venant torsion theory (small deformations and linear-elastic material) we have that

$$M_\theta(x) = GJ \frac{\partial \theta}{\partial x}(x), \tag{A3.2}$$

where G is the material's shear modulus of elasticity, and J is the section's torsional constant. By combining equations (A3.1) and (A3.2) we obtain the equation of motion

$$\frac{\partial^2 \theta}{\partial x^2}(x,t) = \frac{\rho I_p}{GJ} \frac{\partial^2 \theta}{\partial t^2}(x,t). \tag{A3.3}$$

To solve equation (A3.3) let us separate variables and thus consider solutions of the form

$$\theta(x,t) = \phi_x(x) Y_t(t). \tag{A3.4}$$

Thus, by introducing equation (A3.4) into the equation of motion (A3.3) we obtain

$$\frac{\phi_x''(x)}{\phi_x(x)} = \frac{1}{c_s^2} \frac{\ddot{Y}_t(t)}{Y_t(t)} = -\gamma^2, \tag{A3.5}$$

where, the quotation marks indicate derivation over position x, the dots imply derivation over time t, γ is a constant to be calculated, and $c_s^2 = GJ/(\rho I_p)$. Let us observe that each equation in (A3.5) can be analyzed separately and both are second order ordinary differential equations with constant coefficients. Thus we can seek solutions of the form

$$\phi_x(x) = A_1 \sin(\gamma x) + A_2 \cos(\gamma x) \tag{A3.6}$$

$$Y_t(t) = B_1 \sin(\omega t) + B_2 \cos(\omega t), \tag{A3.7}$$

with $\omega^2 = c_s^2 \gamma^2$. Their first derivatives are

$$\phi'_x(x) = \gamma A_1 \cos(\gamma x) - \gamma A_2 \sin(\gamma x) \qquad \text{(A3.8)}$$

$$\dot{Y}_t(t) = \omega B_1 \cos(\omega t) - \omega B_2 \sin(\omega t). \qquad \text{(A3.9)}$$

To find the modes of vibration we need to consider the boundary conditions. We are analyzing the case with a torsional spring (of constant k_1) at the first end of the bar (at $x = 0$), and another torsional spring (of constant k_2) at the second end (at $x = L$). Consider a certain rotation where the first end has a twist angle $\theta_{x=0}$ and the second end has a twist angle $\theta_{x=L}$. Then, the springs will impose corresponding torsional moments given by

$$M_{\theta,k1} = k_1 \theta_{x=0}$$

and

$$M_{\theta,k2} = k_2 \theta_{x=L},$$
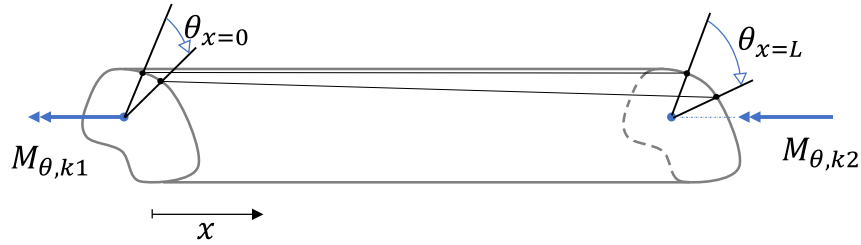
with directions indicated in Figure A3.2.

Figure A3.2: Elongated solid with torsional moments at each end produced by torsional springs.

Thus, the boundary conditions at each end are

$$M_\theta(x = 0, t) = M_{\theta,k1} = k_1 \theta(x = 0, t) \qquad \text{(A3.10)}$$

$$M_\theta(x = L, t) = -M_{\theta,k2} = -k_2 \theta(x = L, t), \qquad \text{(A3.11)}$$

By introducing equation (A3.2) into the first boundary condition given by equation (A3.10) we get

$$M_\theta(0, t) = k_1 \theta(0, t) = GJ \frac{\partial \theta}{\partial x}(0, t) \Rightarrow$$

$$k_1\phi(0) = GJ\phi'(0). \tag{A3.12}$$

Using the proposed solutions of ϕ and ϕ' given in equations (A3.6) and (A3.8), at $x = 0$, and introducing them into equation (A3.12), we get

$$k_1 A_2 = GJ(\gamma A_1) \Rightarrow A_1 = \frac{A_2 k_1}{\gamma GJ}. \tag{A3.13}$$

In an analogous manner, by introducing equation (A3.2) into the second boundary condition given by equation (A3.11) we get

$$M_\theta(L, t) = -k_2\theta(L, t) = GJ\frac{\partial\theta}{\partial x}(L, t) \Rightarrow$$

$$- k_2\phi(L) = GJ\phi'(L). \tag{A3.14}$$

Using the proposed solutions of ϕ and ϕ' given in equations (A3.6) and (A3.8), at $x = L$, and introducing them into equation (A3.14), we get

$$GJ\left[\gamma A_1 \cos(\gamma L) - \gamma A_2 \sin(\gamma L)\right] = -k_2\left[A_1 \sin(\gamma L) + A_2 \cos(\gamma L)\right]. \tag{A3.15}$$

By introducing equation (A3.13) into equation (A3.15) we get

$$GJ\left[\frac{\gamma k_1}{\gamma GJ}A_2 \cos(\gamma L) - \gamma A_2 \sin(\gamma L)\right] = -k_2\left[\frac{k_1}{\gamma GJ}A_2 \sin(\gamma L) + A_2 \cos(\gamma L)\right], \tag{A3.16}$$

which simplifies into

$$(k_1 + k_2)\cos(\gamma L) = \left(GJ\gamma - \frac{k_1 k_2}{\gamma GJ}\right)\sin(\gamma L). \tag{A3.17}$$

Equation (A3.17) can be solved for γ to provide the mode shapes, and the associated frequencies of vibration ω by considering $\omega = c_s\gamma$. To find the γ solutions of equation (A3.17), let us first consider the possible solutions in which $\cos(\gamma L) \neq 0$. In this case, we can pass the cosine term in the left dividing the right term, and thus we get

$$\frac{(k_1 + k_2)}{GJ\gamma - \frac{k_1 k_2}{GJ\gamma}} = \tan(\gamma L). \tag{A3.18}$$

By considering that $k_1 = k_2 = k$, and introducing L in the numerator and denominator of the left term we obtain

$$\frac{(2kL)}{GJ\gamma L - \frac{k^2 L^2}{GJ\gamma L}} = \tan(\gamma L). \tag{A3.19}$$

Equation (A3.19) can be solved numerically. It can also be graphically inspected by observing that the solutions of γ are those that make the left-side function intersect the right-side function, as done in Chapter 3 of this thesis (there expressed as a function of ω instead of γ).

Going back to equation (A3.17), we still still need to analyze possible solutions in which $\cos(\gamma L) = 0$, which implies that $\gamma L = \pi/2 + n\pi$, with $n \in \{0, 1, 2, ...\}$. If the left term is null, the right term must be null; but in this case, $\sin(\gamma L) \neq 0$, so, these γ are solutions only if

$$\left(GJ\gamma - \frac{k_1 k_2}{\gamma GJ}\right) = 0 \Rightarrow$$

$$GJ\gamma = \frac{k_1 k_2}{\gamma GJ} \Rightarrow$$

$$(GJ)^2 \gamma^2 = k^2 \Rightarrow$$

$$\gamma = \frac{k}{GJ}. \tag{A3.20}$$

where it was considered that $k_1 = k_2 = k$. Thus, we have that the mentioned γ are solutions only if

$$\frac{k}{GJ\mathrm{L}} = \gamma L = \pi/2 + n\pi, \tag{A3.21}$$

which is highly unlikely since there must be a perfect coincidence between the different elastic constants and geometric parameters. Nevertheless, let us inspect equation (A3.21) by assigning typical values of the involved magnitudes. The experiments in this thesis involved concrete specimens of size $0.15 \times 0.15 \times 0.6 \ \mathrm{m}^3$, with $J \cong 6.77 \times 10^{-3} \ \mathrm{m}^4$, $L = 0.60 \ \mathrm{m}$, $G \sim 17 \ \mathrm{GPa}$, and $k \sim 100 \ \mathrm{kN.m/rad}$. Thus, by introducing those values into equation (A3.21) and considering the smallest value in the right term ($n = 0$), we get that

$$\frac{k}{GJ\mathrm{L}} \sim 0.05 < 1.57 \cong \pi/2. \tag{A3.22}$$

177

Therefore, possible solutions to equation (A3.17) for γ, are only those given by equation (A3.18)—and by equation (A3.19).